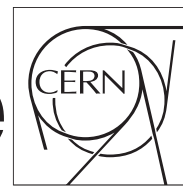


The Compact Muon Solenoid Experiment

# CMS Draft Note

Mailing address: CMS CERN, CH-1211 GENEVA 23, Switzerland



2016/08/02

Head Id: 360214

Archive Id: 362299

Archive Date: 2016/07/27

Archive Tag: trunk

## Investigating the top-Yukawa coupling with the production of a Higgs boson in association with a single top quark in the $H \rightarrow b\bar{b}$ decay channel

T. Chwalek<sup>1</sup>, N. Faltermann<sup>1</sup>, S. Fink<sup>1</sup>, K. Flöh<sup>1</sup>, B. Maier<sup>2</sup>, D. Müller<sup>1</sup>, Th. Müller<sup>1</sup>, F. Roscher<sup>1</sup>,  
and M. Schnepf<sup>1</sup>

<sup>1</sup> Karlsruhe Institute of Technology, Karlsruhe, Germany

<sup>2</sup> Massachusetts Institute of Technology, Cambridge, USA

### Abstract

A direct search for the production of a Higgs boson in association with a single top quark is performed. The analysis considers single top quark production either via the  $t$  channel or via the associated production with a W boson and uses Higgs-boson decays to a bottom quark-antiquark pair and semileptonic top-quark decays. Data recorded by the CMS detector in 2015 in pp collisions at a center-of-mass energy of 13 TeV, amounting to an integrated luminosity of about  $2.3 \text{ fb}^{-1}$ , are analyzed. Upper limits in the two-dimensional plane spanned by the scaling factors for the coupling strength of the Higgs boson to top quarks and to weak gauge bosons,  $\kappa_t$  and  $\kappa_V$ , are determined. The observed (expected) limit on the cross section for the production of a Higgs boson in association with a single top quark in the scenario with a negative Yukawa coupling of the top quark ( $\kappa_t = -1$  and  $\kappa_V = +1$ ) is 6.0 (6.4) times the predicted value.

This box is only visible in draft mode. Please make sure the values below make sense.

PDFAuthor:	B. Maier
PDFTitle:	Investigating the top-Yukawa coupling with the production of a Higgs boson in association with single top in the $h \rightarrow b\bar{b}$ decay channel
PDFSubject:	CMS
PDFKeywords:	CMS, physics, software, computing

Please also verify that the abstract does not use any user defined symbols



## 1 Contents

1	1	Introduction . . . . .	1
2	2	Experimental data and simulation datasets . . . . .	5
3	2.1	Monte–Carlo simulation . . . . .	5
4	2.2	Data samples . . . . .	9
5	3	Objects definition . . . . .	9
6	4	Monte Carlo Corrections . . . . .	12
7	4.1	Pileup Reweighting . . . . .	12
8	4.2	Lepton Efficiency Scale Factors . . . . .	12
9	4.3	CSV Shape Reweighting . . . . .	12
10	4.4	Jet Pseudorapidity in the Forward Region . . . . .	13
11	5	Selection of events . . . . .	14
12	6	Event interpretation . . . . .	19
13	6.1	Jet assignment under the tHq hypothesis . . . . .	19
14	6.2	Jet assignment under the t̄t hypothesis . . . . .	24
15	7	Event classification . . . . .	28
16	8	Uncertainty treatment . . . . .	40
17	9	Limit Extraction . . . . .	42
18	10	Summary . . . . .	46
19	A	Appendix A: Signal cross sections . . . . .	47
20	B	Appendix B: Distributions of variables used in the reconstruction . . . . .	49
21	C	Appendix C: Changes from 8 to 13 TeV . . . . .	53
22	D	Appendix D: Limit Values . . . . .	54
23	E	Appendix E: BDT output distributions . . . . .	55

## 1 Introduction

We present an analysis searching for a single top quark produced in association with a Higgs boson decaying to  $b\bar{b}$ . This channel is important to study the Yukawa couplings of the Higgs boson, Htt and HW, as well as their relative phase in the standard model.

As for the more common case without the Higgs boson, single top production can be separated at leading order (LO) into three production modes:  $t$ -channel,  $tW$  associated production, and  $s$ -channel. While the latter production mode has a negligible cross section, the other two modes are considered in this search; notably the  $tHW$  production mode is considered for the first time in this channel.

The Yukawa couplings to the Higgs defined in the standard model depend on the mass of the particle coupled to. The ratio of the actual couplings to the standard model ones for fermions such as the top quark are defined to be  $\kappa_t$ . Similarly,  $\kappa_V$  is the ratio for the vector bosons. The sign of  $\kappa_t$  gives information about the relative phase between the fermion and boson couplings. Only the  $H \rightarrow \gamma\gamma$  analysis is sensitive to the sign of  $\kappa_t$  because the decay to photons proceeds through interfering diagrams containing both fermion (top quark) and boson (W boson) loops. For beyond the standard model (BSM) theories, each fermion and boson could have a different coupling to the Higgs, or there could be new particles entering the loops, which could potentially change the relative phases.

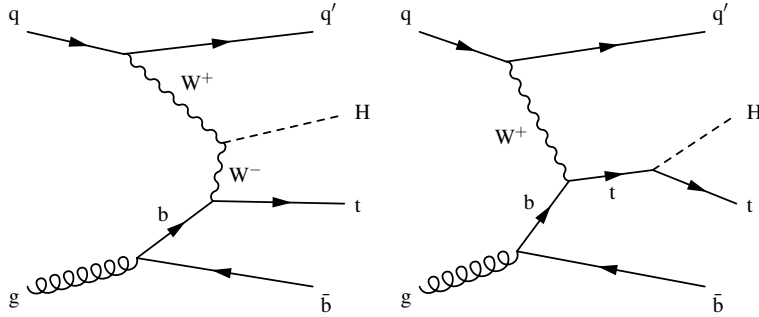


Figure 1: Representative Feynman diagrams for the associated production of single top quarks and Higgs bosons in the  $t$ -channel.

For the  $t$ -channel single top quark production in association with a Higgs boson, there are two dominant diagrams as shown in Figure 1 (see Figure 2 for the corresponding  $tW$  production diagrams). The Mandelstam variables characterizing the  $Wb \rightarrow tH$  scattering are given by:

$$\begin{aligned} s &= (p_W + p_b)^2, \\ t &= (p_W - p_H)^2, \\ u &= (p_W - p_t)^2. \end{aligned}$$

This breakdown to the core scattering process, ignoring the upper vertices in the Feynman diagrams, is a valid approach at high energies, where in the effective  $W$  approximation [1] one treats  $W$  bosons that appear in intermediate states of a scattering process as partons in the proton. According to [2], the amplitude in the hard-scattering regime with  $s, -t, -u \gg m_t^2, m_W^2, m_H^2$  is then given by

$$\mathcal{A} = \frac{g}{\sqrt{2}} \left[ (\kappa_f - \kappa_V) \frac{m_t \sqrt{s}}{m_W v} A \left( \frac{t}{s}, \varphi; \xi_t, \xi_b \right) + \right. \quad (1)$$

$$\left. \left( \kappa_V \frac{2m_W s}{v} \frac{t}{t} + (2\kappa_f - \kappa_V) \frac{m_t^2}{m_W v} \right) B \left( \frac{t}{s}, \varphi; \xi_t, \xi_b \right) \right], \quad (2)$$

where  $v$  is the vacuum expectation value of the Higgs field. The exact expressions for  $A$  and  $B$ , which are dependent on the spinors  $\xi_{t,b}$  of the top and bottom quark and the angle  $\varphi$  (the azimuthal angle of the Higgs boson in the reference frame centered at the partonic collision point, where the  $z$  axis points along the beam direction), can be found in [2]. It is easy to see in the above equation that there is an almost total destructive interference between the two leading order Feynman diagrams. In the standard model, with  $\kappa_t = +1$ , the expected cross section at 13 TeV is 71 fb for  $tHq$  and 16 fb for  $tHW$ , respectively. With BSM theories, there can be a negative Yukawa coupling of the top quark to the Higgs boson of  $\kappa_t = -1$  (see for example [3]); this results in a constructive interference between the two diagrams and expected cross sections of 793 fb ( $tHq$ ) and 147 fb ( $tHW$ ). Fig. 4 shows the  $tHq$  and  $tHW$  cross section in the  $\kappa_t - \kappa_V$  plane. Several papers have discussed using this channel of Higgs boson production in association with a single top quark to measure the coupling to fermions as well as the relative phase of the  $Htt$  and  $HWW$  couplings [2, 4–6].

Accordingly, for this analysis note, the scope of the 8 TeV analysis [7] is extended in the sense that multiple points in the two-dimensional plane are being looked for and a direct search is performed for each of them, using the full 2015 dataset at  $\sqrt{s} = 13$  TeV.

Semileptonic top decays are used. In addition to looking for two b-jets from the Higgs boson decay and one b-jet from the top quark decay, there will also be a charged lepton (either an

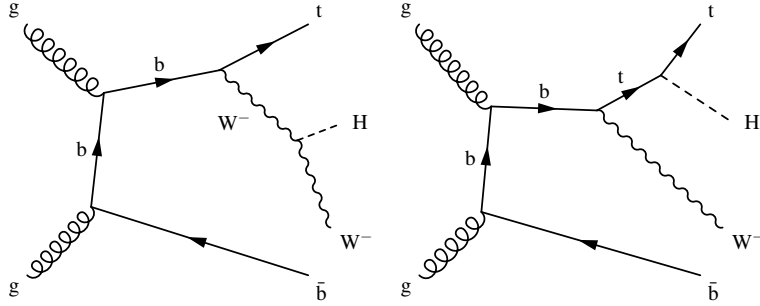


Figure 2: Representative Feynman diagrams for the associated production of single top quarks and Higgs bosons in the tW-channel.

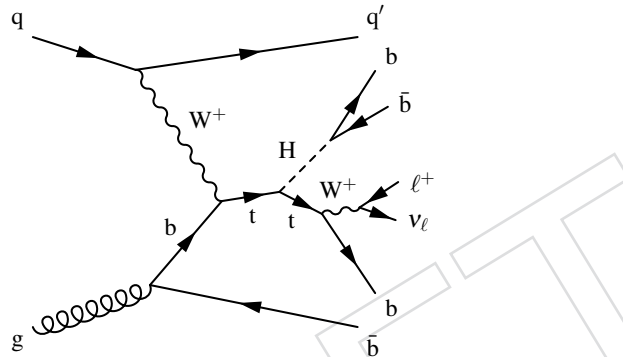


Figure 3: Feynman diagram for the full decay channel with five jets, a lepton, and  $\cancel{E}_T$ . The b jet arising from the hadronization of the spectator b quark at the bottom of the diagram is very forward and therefore often outside of the detector (or at least tracker) acceptance.

61 electron or a muon) and missing transverse energy ( $\cancel{E}_T$ ) from the decay of the W from the top  
 62 quark. This gives four jets, three of which are b-jets. The light jet should be in the forward  
 63 direction as it is from the recoiling quark. There is also the possibility that the b-jet produced in  
 64 the initial-state gluon splitting is measurable in the detector, which then results in a total of five  
 65 jets with four of them being b-jets. The full decay chain for this case is illustrated in Figure 3.

66 Single-muon and -electron triggers are used and an initial object selection requires events with  
 67 at least four or at least five jets, three or four b-tags from the combined secondary vertex tagger  
 68 (CSV), a tight electron or muon, and  $\cancel{E}_T$ . All backgrounds, including the main background  $t\bar{t}$  +  
 69 jets, are simulated with the Monte-Carlo method; the simulations are normalized to the most  
 70 recent and accurate available theory cross sections, and the shapes of the modeled distributions  
 71 are validated in a dedicated control region. The residual amount of QCD multi-jet events is  
 72 rejected by imposing the aforementioned cut on  $\cancel{E}_T$ . Multivariate techniques are used to assign  
 73 jets to both a tH and  $t\bar{t}$  hypothesis and separate the signal from the background. Limits are then  
 74 found and results are presented.

75 Appendix C details the changes of the presented analysis w.r.t. the 8 TeV analysis.

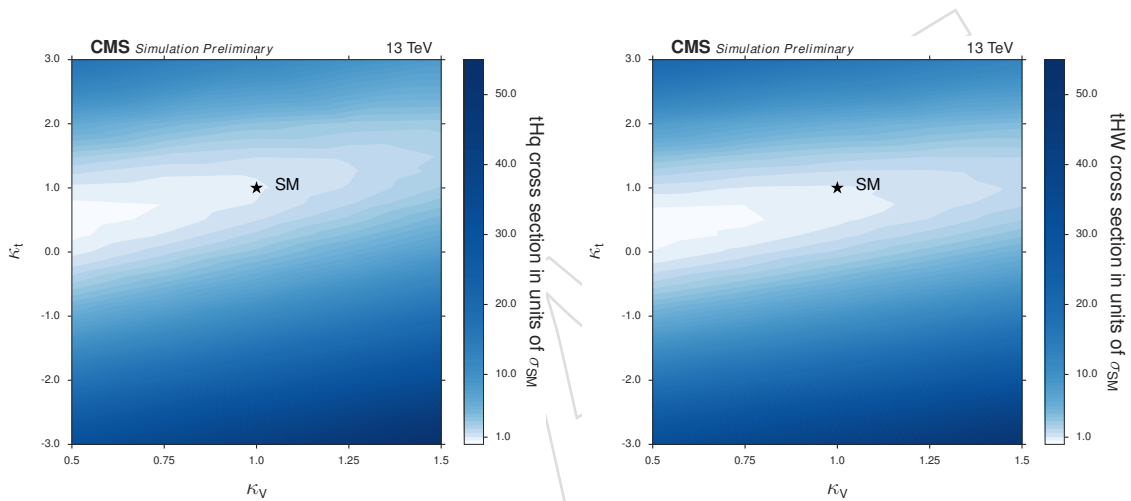


Figure 4: Cross sections in the  $\kappa_t - \kappa_V$  plane at 13 TeV for  $t\bar{H}q$  (left) and  $t\bar{H}W$  (right) production. Right figure adapted from [8].

## 76 2 Experimental data and simulation datasets

### 77 2.1 Monte–Carlo simulation

78 Due to recent developments in the field of MC simulation and new phenomenological studies  
 79 on tHq production, the way of modeling the signal process has been revised for the first Run-  
 80 II analysis. It has been adapted to the latest phenomenological studies on tHq performed in  
 81 [9]. While the accuracy of the matrix element calculation is LO in QCD as for Run-I, the main  
 82 changes in the signal modeling are the use of the new NNPDF3.0 set [10] that incorporates  
 83 recent LHC data, as well as switching to a dedicated dynamical scale  $\mu = (m_T(t) + m_t(H) +$   
 84  $m_T(b))/6$  to better account for the event kinematics at large transferred momenta. Moreover,  
 85 Pythia8 with the CUETP8M1 underlying event tune has replaced the Run-I default Pythia6  
 86 TuneZ2\*. The settings and additional information on the modeling are given in Table 1.

87 For the first time, the tHW process is also considered and will contribute to the signal yields.  
 88 Due to its small cross section, the analysis chain however will be optimized (and BDTs trained)  
 89 for the tHq process only. Fig. 5 contrasts the two signal processes in terms of the kinematics of  
 90 the Higgs boson and the top quark. In general, the tHW process has harder  $p_T$  spectra and the  
 91 objects are more central, which applies to both the Higgs boson and the top quark, and propa-  
 92 gates to their decay products. The topology of the process resembles the one of top quark pair  
 93 production (in association with a Higgs boson). Events originating from tHW production are  
 94 therefore expected to yield scores in the final BDT output which range somewhere in between  
 95 the tHq signal and the bulk of  $t\bar{t}$  plus  $t\bar{t}H$  events.

96 Both signal samples are generated for the point  $(\kappa_t|\kappa_V) = (-1|+1)$ , i.e. this point gets unit  
 97 weights. The tHq process is generated within the four-flavor-scheme (4F) and with dynamical  
 98 factorization and renormalization scales while for the generation of tHW events fixed scales  
 99 (40 GeV) and the five-flavor-scheme (5F) are used. The choice of the 5F-scheme for the tHW  
 100 process is motivated by the need to avoid interference with  $t\bar{t}H$  process.

101 The considered background processes are the same as for the 8 TeV analysis and are listed in  
 102 Table 2. The  $t\bar{t}$  background is split into five processes based on the flavor of additional jets at  
 103 generator level which do not arise from the top quark decays in the event:  $t\bar{t} + b\bar{b}$ ,  $t\bar{t} + b$ ,  $t\bar{t} + 2b$ ,  
 104  $t\bar{t} + c\bar{c}$  and  $t\bar{t} + \text{light}$  [11]. Events that belong to  $t\bar{t} + b\bar{b}$  have 2 or more extra b-quark jets which

Table 1: Simulation settings for the signal processes at 8 and 13 TeV. The tHW process has not been considered in the 8 TeV analysis. ME: matrix element; PS: parton shower; UE: underlying event. The cross sections have been obtained at NLO QCD.

$\sqrt{s}$ Process	8 TeV tHq	13 TeV	
ME generator ME precision	MadGraph 5 LO	MG5_aMC@NLO LO	
PS UE tune	Pythia6 TuneZ2*	Pythia8 CUETP8M1	
QCD description	4F	4F	5F
$\mu_{R,F}$ PDF	fixed, 100 GeV cteq6l1	dynamical, $\Sigma_{H,t,q} m_T / 6$ NNPDF30_lo_as_0130_nf_4	fixed, 40 GeV NNPDF30_lo_as_0130
Normalized to $\sigma_{\kappa_t=-1}$ [fb]	5F NLO 233.8	4F NLO 792.7	5F NLO 147.2

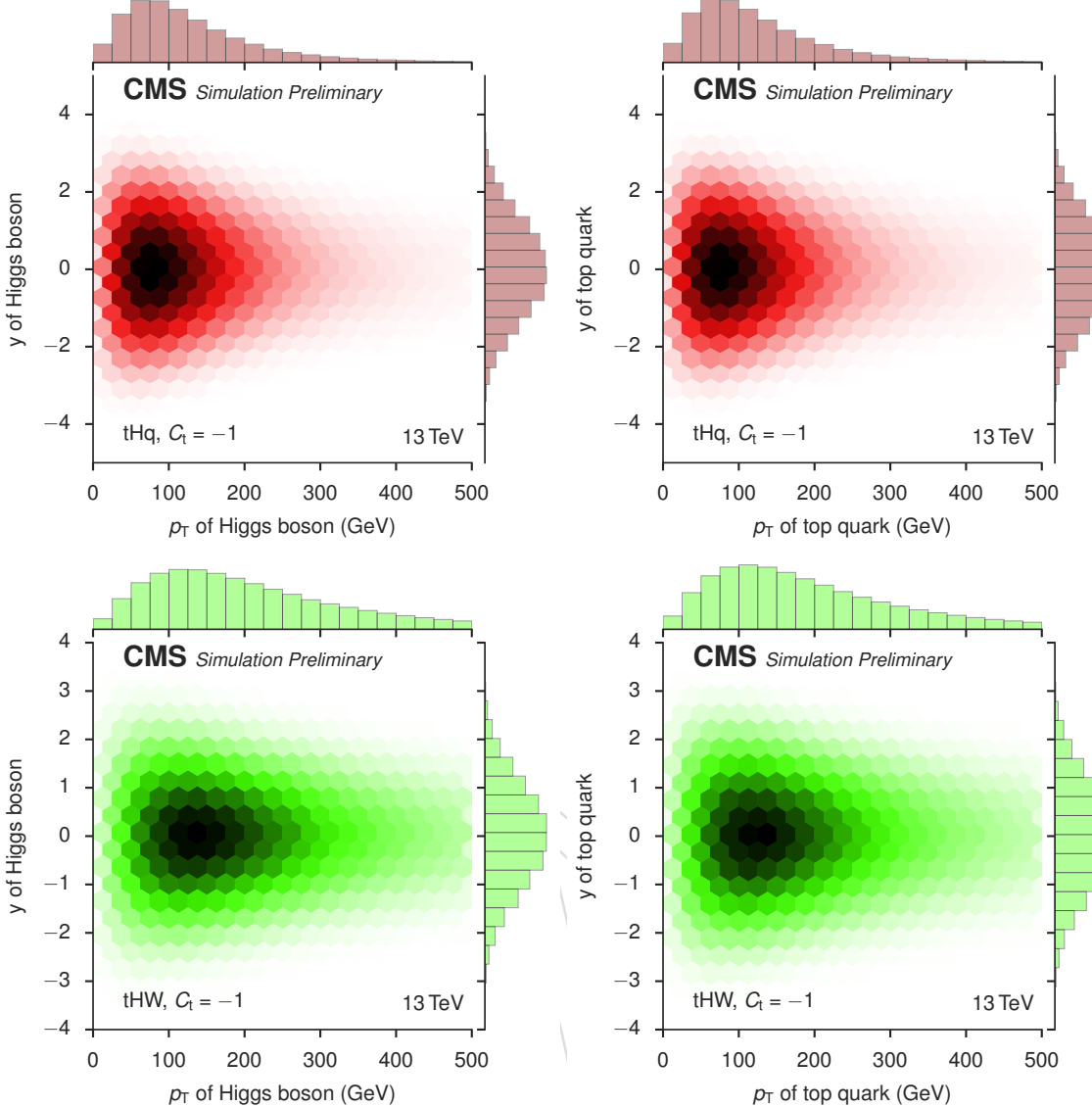


Figure 5: Kinematics ( $p_T$  vs. the rapidity  $y$ ) of the Higgs boson and the top quark at LO for tHq and tHW at  $\sqrt{s} = 13$  TeV and for  $\kappa_t = -1$ .

105 originate from one or more overlapping B hadrons.  $t\bar{t} + b$  corresponds to events with only one  
 106 additional b-quark jet originating from a single B hadron while  $t\bar{t} + 2b$  events have only one  
 107 additional b-quark jet which originates from two or more overlapping B hadrons. Events in  $t\bar{t}$   
 108 +  $c\bar{c}$  have at least one c-quark jet and events in  $t\bar{t} + \text{light}$  do not correspond to any of the other  
 109 processes mentioned.

110 The additional category  $t\bar{t} + 2b$  which was part of the  $t\bar{t} + b\bar{b}$  category before is now utilized.  
 111 This distinction is motivated by the differences in the modeling of a collinear gluon splitting  
 112 as opposed to two clearly separated b quarks. The matrix element generator POWHEG is used  
 113 for  $t\bar{t}$ , modeling the two top quarks at NLO and an additional emission at LO accuracy. The  
 114 simulation of further radiation is left to the parton shower (Pythia8). This will lead to relatively  
 115 large uncertainties on predictions for  $t\bar{t}$  in the phase space determined by the event selection,  
 116 both for shapes and the overall normalization. An alternative approach for simulating this  
 117 major background employs the FxFx merging and models more jets already on matrix element  
 118 level at NLO QCD. On the one side, this should help in reducing the scale uncertainties, but

<sup>119</sup> since this approach creates a large fraction of negative event weights, distributions are afflicted  
<sup>120</sup> with large statistical uncertainties. Consequently, such an MC sample is not utilized in the  
<sup>121</sup> analysis to prohibit overtraining due to statistical fluctuations and make the limit calculation  
<sup>122</sup> more robust, until sufficient statistical power is available.

DRAFT

## 2 Experimental data and simulation datasets

Table 2: Nominal simulation datasets with prompt leptons. The fragment “RunIIIFall15MiniAODv2–PU25nsData2015v1\_76X\_mcRun2–asymptotic<sub>IC</sub>\_v12” and the postfix “\_MINIAODSIM” are omitted everywhere. When only specific decays of top quarks are considered in a dataset, the inclusive cross section is scaled using the dileptonic  $t\bar{t}$  branching ratio 0.10608 and the semileptonic  $t\bar{t}$  branching ratio 0.43923 respectively.

Dataset name	Num. of events	Cross section (pb)
/THQ_Hincl_13TeV-madgraph-pythia8.TuneCUETP8M1/...-v1 /THW_Hincl_13TeV-madgraph-pythia8.TuneCUETP8M1/...-v1	3 495 199 1 496 000	see Table 13 see Table 14
/DYJetsToLL_M-10to50_TuneCUETP8M1_13TeV-amcatnloFXFX-pythia8/...-ext3-v1 /DYJetsToLL_M-50_TuneCUETP8M1_13TeV-amcatnloFXFX-pythia8/...-ext3-v1	76 558 711 121 212 419	22635.09 (NNLO[12]) 6025.2 (NNLO[13])
/ST_t-channel_antitop_4f_inclusiveDecays_13TeV-powhegV2-madspin-pythia8.TuneCUETP8M1/...-v1 /ST_t-channel_antitop_4f_inclusiveDecays_13TeV-powhegV2-madspin-pythia8.TuneCUETP8M1/...-v1	38 932 192 64 957 724	80.95 (NLO[14]) 136.02 (NLO[14])
/ST_tW_top_5f_inclusiveDecays_13TeV-powheg-pythia8.TuneCUETP8M1/...-v1 /ST_tW_top_5f_inclusiveDecays_13TeV-powheg-pythia8.TuneCUETP8M1/...-v1	999 400 1 000 000	35.9 (NNLO[14]) 35.9 (NNLO[14])
/TTWJetsToLNu_TuneCUETP8M1_13TeV-amcatnloFXFX-madspin-pythia8/...-v1 /TTWJetsToQQ_TuneCUETP8M1_13TeV-amcatnloFXFX-madspin-pythia8/...-v1	250 307 831 847	0.21 (NLO[15]) 0.435 (NLO[15])
/TTTo2L2Nu_13TeV-powheg/...-v1 /TTTo2L2Nu_13TeV-powheg/...-ext1-v1	4 995 600 108 233 158	831.76 (NNLO[16]) 831.76 (NNLO[16])
/TTToSemiLeptonic_13TeV-powheg/...-ext1-v1	353 216 236	831.76 (NNLO[16])
/TTZToLLNuNu_M-10_TuneCUETP8M1_13TeV-amcatnlo-pythia8/...-v1 /TTZToQQ_TuneCUETP8M1_13TeV-amcatnlo-pythia8/...-v1	349 200 747 000	0.2529 (NLO[15]) 0.611 (NLO[15])
/WJetsToLNu_TuneCUETP8M1_13TeV-madgraphMLM-pythia8/...-v1 /ttHToobb_M125_13TeV_powheg-pythia8/...-v1	24 156 124 3 772 012	61526.7 (NNLO[13]) 0.2934 (NLO[17])

123 **2.2 Data samples**

124 The results presented here are based on  $2.3 \text{ fb}^{-1}$  of the 2015 CMS data, corresponding to the  
 125 Run2015D data-taking era. Table 3 lists the datasets used for this analysis, based on the trig-  
 126 gers employed to collect the data. Only luminosity sections certified as good according to the  
 127 Cert\_13TeV\_16Dec2015ReReco\_Collisions15\_25ns\_JSON\_v2.json file are considered.  
 128 Luminosities are quoted from the pixel cluster counting method and have an uncertainty of  
 129 2.7% [18].

Table 3: The CMS datasets analyzed for this analysis.

Dataset	Run Range	Integrated Luminosity
/SingleMuon/Run2015D-16Dec2015-v1/MINIAOD	256630–260627	$2.3 \text{ fb}^{-1}$
/SingleElectron/Run2015D-16Dec2015-v1/MINIAOD	256630–260627	$2.3 \text{ fb}^{-1}$

130 **3 Objects definition**

131 **Primary vertices**

132 Primary vertices are reconstructed with the help of the standard deterministic-annealing clus-  
 133 tering algorithm [19]. The first vertex in the collection (the one with greatest sum of  $p_T^2$  for the  
 134 associated tracks) is required to be within a cylinder of radius 2 cm around the nominal beam  
 135 axis and its  $z$ -coordinate must satisfy  $|z| < 24$  cm, where  $z = 0$  cm corresponds to the geomet-  
 136 ric center of the detector. In addition, the reconstruction algorithm must not mark the vertex  
 137 as “fake” and must assign it at least 4 degrees of freedom, which roughly corresponds to the  
 138 requirement of at least four tracks associated with the vertex.

139 The vertices that satisfy the above requirements are exploited to mitigate an impact from addi-  
 140 tional pp interactions within the same bunch crossing (the “pileup”) according to the so-called  
 141 charged-hadron subtraction (CHS) scheme. If a PF candidate is identified as a charged hadron  
 142 and is associated to any but the first of these vertices, the candidate is removed from an event.

143 **Muons**

144 Muons considered in the analysis are defined according to the tight muon ID [20]. A PF candi-  
 145 date is required to be reconstructed as a global muon. The goodness-of-fit for its track must sat-  
 146 isfy  $\chi^2/\text{n.d.f.} < 10$ . The global-track fit must include at least one hit in a muon chamber. Muon  
 147 segments in at least two muon stations must be associated to the candidate. The track’s trans-  
 148 verse impact parameter with respect to the first primary vertex must satisfy  $|d_{xy}| < 2$  mm, and  
 149 the  $z$ -position of the muon’s vertex must lie within 5 mm around the  $z$ -position of the primary  
 150 vertex. At least one hit in the pixel system and at least six tracker layers with measurements  
 151 are required.

152 In addition to the above identification criteria, the muon must have  $p_T > 25 \text{ GeV}/c$  and  $|\eta| < 2.4$   
 153 and must be isolated satisfying  $I_{\Delta\beta} < 0.15$ , where the relative  $\Delta\beta$ -corrected isolation is defined  
 154 as

$$I_{\Delta\beta} = \frac{1}{p_T} \left( \text{chargedHadronIso} + \max(\text{neutralHadronIso} + \text{photonIso} - 0.5 \cdot \text{puChargedHadronIso}, 0) \right). \quad (3)$$

155 Here, values in the numerator are sums of the transverse momenta of charged-hadron, neutral-  
 156 hadron, and photon PF candidates as well as charged-hadron pileup PF candidates inside a

157 cone of size  $\Delta R = \sqrt{\Delta\eta^2 + \Delta\phi^2} = 0.4$  around the muon, and  $p_T$  is the muon's transverse  
 158 momentum.

159 A muon satisfying the above requirements is referred to as a "tight" muon. For the purpose of  
 160 an event selection we also define "loose" muons. They are required to be global muons and to  
 161 satisfy  $p_T > 15 \text{ GeV}/c$  and  $I_{\Delta\beta} < 0.2$ .

## 162 Electrons

163 Similar to the case of muons, "tight" and "loose" electrons are defined. A "tight" electron  
 164 must not be identified as originating from a photon conversion. It must have a triggering  
 165 MVA ID [21] response larger than 0.8 and pass the associated trigger-emulating preselection.  
 166 The electron must have  $p_T > 30 \text{ GeV}/c$  and  $|\eta| < 2.1$ , excluding the transition region between  
 167 the barrel and the endcap of the electromagnetic calorimeter,  $1.4442 < |\eta_{sc}| < 1.5660$ , where  $\eta_{sc}$   
 168 is the pseudorapidity of the associated supercluster.

169 In addition, the relative  $\rho$ -corrected isolation  $I_\rho$  with a cone of size  $\Delta R = 0.3$  must be smaller  
 170 than 0.15. The isolation is calculated as

$$I_\rho = \frac{1}{p_T} \left( \text{chargedHadronIso} + \max(\text{neutralHadronIso} + \text{photonIso} - \rho A_{\text{eff}}, 0) \right). \quad (4)$$

171 Here, the charged-hadron, neutral-hadron, and photon components of the isolation are defined  
 172 in the same way as in Eq. (3) but using a smaller cone, and  $\rho$  is the average angular  $p_T$  density in  
 173 an event. The effective area  $A_{\text{eff}}$  is defined such that it compensates for the neutral component  
 174 of pileup in the isolation.

175 "Loose" electrons are only required to have  $p_T > 15 \text{ GeV}/c$ ,  $|\eta| < 2.5$ , and  $I_\rho < 0.15$ .

## 176 Jets

177 Jets are clustered using the anti- $k_T$  algorithm [22] with a cone size of 0.4. Jets that fall within  
 178 a cone of size 0.4 of a loose electron or muon are removed from the collection. Produced jets  
 179 must meet the cuts for the loose working point of the jet identification algorithm [23]. Here,  
 180 the jet must contain more than one constituent, and it must have a neutral-electromagnetic  
 181 energy fraction and a neutral-hadron energy fractions smaller than 0.99, each. If the jet is central  
 182 ( $|\eta| < 2.4$ ) it is required, in addition, to have a non-zero charged-hadron energy fraction  
 183 and a non-zero charged multiplicity. The charged-electromagnetic energy fraction has to be  
 184 smaller than 0.99. For jets with  $|\eta| > 3.0$  only these requirements are applied: the neutral  
 185 electromagnetic fraction has to be smaller than 0.90 and the number of neutral particles has to  
 186 be larger than 10.

187 In order to account for the non-linear calorimeter response and the detector mismodeling,  
 188 the measured jet energy is corrected [24]. The so-called L2Relative and L3Absolute cor-  
 189 rections from payload Fall115\_25nsV2 are applied to both real data and simulation, and  
 190 L2L3Residual corrections are applied to the real data only, while a jet energy of MC sam-  
 191 ples is smeared to match the  $p_T$  differences observed between reconstructed and associated  
 192 generated jet in data to those in the simulation [25]. In addition, an attempt to subtract the  
 193 pileup energy is performed by employing L1FastJet corrections.

194 All central ( $|\eta| < 2.4$ ) jets with  $p_T > 20 \text{ GeV}/c$  and all forward jets ( $2.4 < |\eta| < 4.7$ ) with  
 195  $p_T > 40 \text{ GeV}/c$  are considered in the analysis. The higher threshold in the forward region  
 196 is motivated by a mismodeling observed there. In addition, pseudorapidities of forward jets  
 197 are modified in order to mask the mismodeling. The problem will be discussed in detail in  
 198 Section 4.4.

199 As the signal signature involves b quarks, the b-tagging capability of the detector is exploited in  
 200 the analysis. Jets produced by b quarks are identified with the help of the combined secondary  
 201 vertex (CSVv2) algorithm [26]. The medium working point is utilized, which corresponds to  
 202 the b-tagging discriminator value larger than 0.800.

### 203 Missing transverse energy

204 The missing transverse energy  $\vec{E}_T$  is reconstructed as  $\vec{E}_T = -\sum_i \vec{p}_{Ti}$ , where the sum is cal-  
 205 culated over all PF candidates. The `slimmedMET` collection in simulation is recorrected for  
 206 possible effects caused by applied jet corrections. The four-vectors of the initial, uncorrected  
 207 jets are added to the four-vectors of the missing transverse energy, thereby undoing the  $\vec{E}_T$  cal-  
 208 culation. From the resulting four-vector the corrected jets are subtracted ensuring a coherent  
 209 recalculation of the missing transverse energy.

### 210 W boson reconstruction

211 All decay products are reconstructed in the detector, except for the neutrino from the W boson  
 212 decay which escapes unobserved. While the transverse momentum of the neutrino can be  
 213 inferred from the missing energy, the longitudinal momentum can be determined from an extra  
 214 assumption [27]. Due to the  $\vec{E}_T$  resolution, the resolution on the reconstructed transverse mass  
 215 of the W,  $m_{\ell\nu}$ , is much greater than the intrinsic W-boson width.

216 To reconstruct the W boson 4-momentum, we assume that the  $x$  and  $y$  components of the miss-  
 217 ing energy are entirely due to the escaping neutrino, and apply the W-mass constraint in order  
 218 to extract the  $z$  component ( $p_{z,\nu}$ ):

$$m_W^2 = (E_\ell + \sqrt{\vec{E}_T^2 + p_{z,\nu}^2})^2 - (\vec{p}_{T,\ell} + \vec{E}_T)^2 - (p_{z,\ell} + p_{z,\nu})^2. \quad (5)$$

219 This equation in general has two solutions:

$$p_{z,\nu} = \frac{\Lambda \cdot p_{z,\ell}}{p_{T,\ell}^2} \pm \sqrt{\frac{\Lambda^2 \cdot p_{z,\ell}^2}{p_{T,\ell}^4} - \frac{E_\ell^2 \cdot \vec{E}_T^2 - \Lambda^2}{p_{T,\ell}^2}}, \quad (6)$$

220 with

$$\Lambda = \frac{m_W^2}{2} + \vec{p}_{T,\ell} \cdot \vec{E}_T. \quad (7)$$

221 If the discriminant in Eq. (6) becomes negative, or equivalently  $m_T$  is larger than  $m_W$ , the solu-  
 222 tions have an imaginary component. This happens mostly because of the finite  $\vec{E}_T$  resolution,  
 223 while lepton momentum resolution and the finite W intrinsic width give negligible contribu-  
 224 tions.

225 In this analysis the imaginary component is eliminated by modifying the neutrino transverse  
 226 momentum components while keeping the measured  $\vec{E}_T$  vector fixed, while still respecting the  
 227  $m_W$  constraint from Eq. (5). This is obtained by imposing that the discriminator, and thus the  
 228 square-root term in Eq. (6), are null. This condition gives a quadratic relation between  $p_{x,\nu}$  and  
 229  $p_{y,\nu}$ , with two possible solutions, among which the one with minimal distance between  $p_{T,\nu}$   
 230 and  $\vec{E}_T$  is chosen.

231 In the case of two real solutions for  $p_{z,\nu}$ , the solution with the smallest absolute value is chosen.

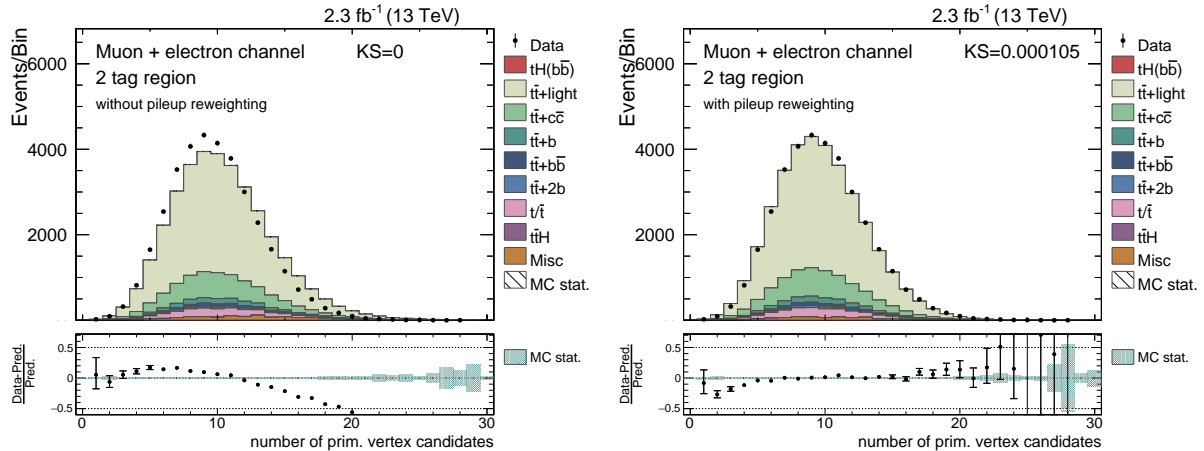


Figure 6: Distribution of the number of primary vertices per event before (left) and after (right) application of the pileup reweighting. The simulation models slightly more primary vertices than are observed in data. For both distributions the simulation is scaled to match the observed event numbers in data. After the reweighting a good agreement of simulation and recorded events is observed.

## 4 Monte Carlo Corrections

### 4.1 Pileup Reweighting

The pileup profile observed in data, derived from the (effective) total cross section of inelastic pp scattering and from a measurement of the instantaneous luminosity, does not agree exactly with the profile imposed in the MC production. To correct the difference, MC events are reweighted based on the true number of pileup interactions, as directed by the standard prescription [28], assuming a minimum-bias cross section of 69 mb for the pileup reweighting. The effect of the reweighting can be seen in Figure 6.

### 4.2 Lepton Efficiency Scale Factors

The correction of the muon efficiencies encompasses separate scale factors for the muon trigger, identification and isolation efficiencies. The correction factors are provided by the Muon POG [29] and are derived with tag-and-probe methods [30] at the  $J/\Psi$  or Z boson resonances.

Simulated electron efficiencies for the reconstruction as well as for the triggering MVA-ID are corrected [31]. The efficiencies are provided by the EGamma POG and have been determined on large  $Z \rightarrow e^+e^-$  samples with the tag-and-probe procedure [32]. The correction of the electron isolation and trigger efficiency are also applied; since the EGamma POG does not provide these efficiencies, the private produced correction scale factors are used.

The efficiency scale factors cause a slight change in shape for some distributions and a reduction of the overall yield of  $\sim 4\%$ .

### 4.3 CSV Shape Reweighting

For the output of the CSVv2 b-tagging algorithm a reweighting procedure is applied [33]. Every event is assigned a weight such that the complete measured CSV distribution in data is reproduced by the simulation. Weights are calculated separately for heavy and light flavored jets. The applied scale factors are functions of the jet CSV output value, the  $p_T$  and the  $\eta$  of the jet. The scale factors for the heavy flavored jets are derived via the tag-and-probe method in a control region enriched with fully leptonically decaying top quark pairs, whereas scale factors

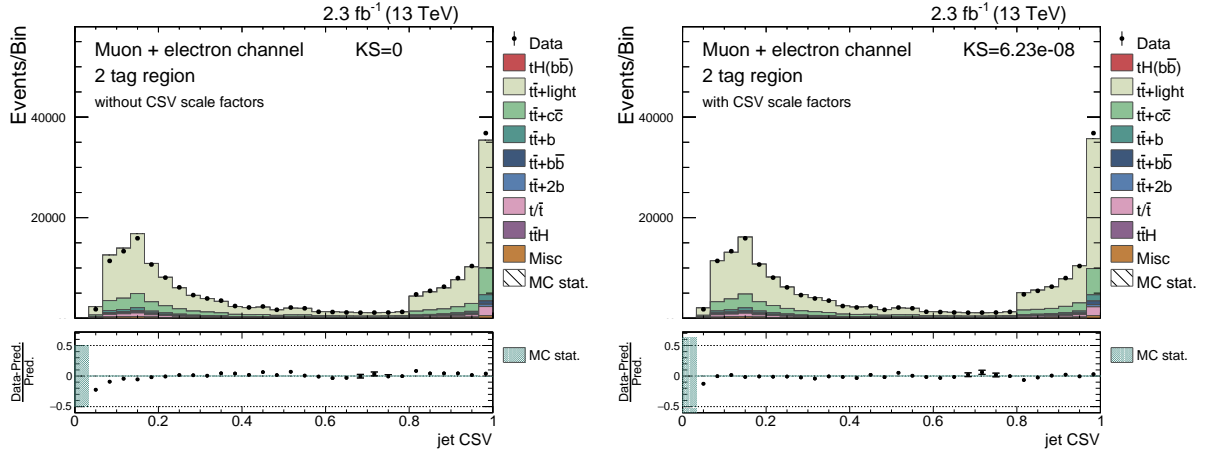


Figure 7: Distribution of the CSV output for all jets per event before (left) and after (right) application of the CSV reweighting. For both distributions the simulation is scaled to match the observed event yields in data. After the reweighting an improved agreement of simulation and recorded events is observed.

for light flavored jets are obtained in a  $Z \rightarrow \ell\ell$  control region. The scale factors to account for light flavor contamination are calculated as

$$SF_{HF}(CSV, p_T, \eta) = \frac{\text{Data} - MC_{LF}}{MC_{HF}}, \quad (8)$$

where for events in data the presence of one b-tagged jet is required and  $MC_{LF}$  and  $MC_{HF}$  are the simulated yields of light flavored jets and heavy flavored jets, respectively. For the calculation of the scale factors for light flavored jets, the yields in data are estimated by requiring one jet to be untagged and exchanging the positions of  $MC_{HF}$  in Equation 8. The effect of the reweighting can be seen in Figure 7.

This procedure allows for the exploitation of the full information of the CSV output distribution, thus making it possible to employ complete CSV distributions of specific jets as input variables in the reconstruction and classification. More information on the scale factor estimation can be found in Reference [34].

#### 4.4 Jet Pseudorapidity in the Forward Region

One of the main discriminant features of the  $tHq$  signal process is the light forward jet. Unfortunately, a severe mismodeling of the jet pseudorapidity in the forward region is evident. The mismodeling is clearly visible in ratio distributions when comparing the yields found in data and simulation, as can be seen in Figure 8.

The main features are an overestimated number of jets in simulation in the region with  $2.5 \leq |\eta| \leq 3.2$ . In the region around  $|\eta| \sim 3.2$  the agreement of simulation with the amount of measured jets in data is improved. In the most forward region of the detector with  $|\eta| > 3.5$  the predicted number of jets in simulation again exceeds the measured number. The disagreement increases for increasing absolute values of the pseudorapidity. The effect is most apparent for low- $p_T$  jets, but still visible at the higher end of the  $p_T$  spectrum.

To be insensitive to this discrepancy of the pseudorapidity for the further analysis, the actual  $\eta$  values of the jets in the forward region are modified:

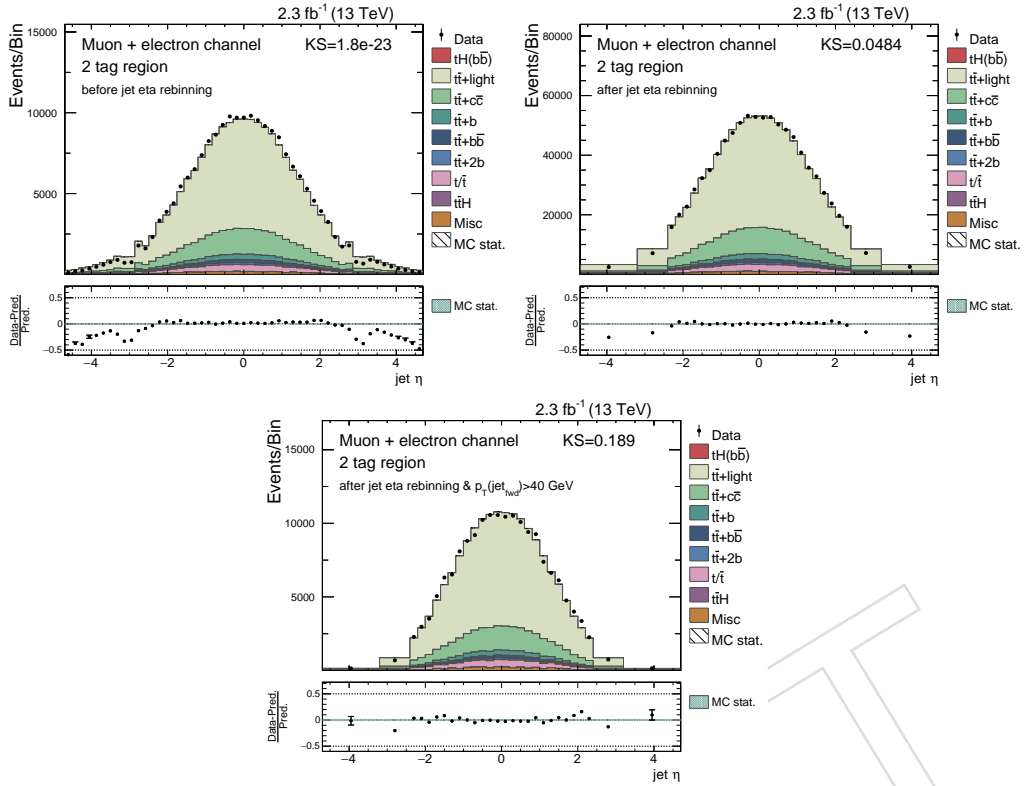


Figure 8: The situation before the jet eta rebinning is shown (top left), after the rebinning (top right) and after a stricter cut of  $p_T > 40 \text{ GeV}$  for jets in the forward region.

$$\eta \rightarrow \eta' = \begin{cases} \eta & \text{if } |\eta| < 2.4, \\ 2.8 \cdot \text{sign}(\eta) & \text{if } 2.4 \leq |\eta| < 3.2, \\ 3.5 \cdot \text{sign}(\eta) & \text{if } 3.2 \leq |\eta|. \end{cases}$$

- 275 This treatment was already successfully employed in the analysis at 8 TeV. The bin boundaries  
 276 are chosen in accordance with the derivation of the L2L3Residual corrections in these two  
 277 bins due to a low number of jets in the forward region. The transformation is applied to sim-  
 278 ulation as well as to data, making the redefined pseudorapidity an effective observable. The  
 279 analysis only relies on a good agreement of the simulation with the recorded data in the trans-  
 280 formed variables. It is therefore blind to the mismodeling in the forward region.  
 281 After the correction is applied a slightly different normalization in the forward region in sim-  
 282 ulation is still observed, but this can be improved by requiring  $p_T > 40 \text{ GeV}$  for jets with  
 283  $|\eta| > 2.4$ .

## 284 5 Selection of events

- 285 In order to distinguish signal events from the overwhelming background, the analysis focuses  
 286 on the semileptonic decays of the top quark exclusively. At the same time no attempts are made  
 287 to reconstruct  $\tau$ -leptons, and the corresponding decays are included only indirectly, through  
 288 decays of the  $\tau$ -leptons to muons or electrons.  
 289 The analysis is performed with data collected with the following triggers: HLT\_IsoTkMu20\_vX  
 290 or HLT\_IsoMu20\_vX for the muon channel and HLT\_Ele27\_eta2p1\_WP\_Loose\_Gsf\_vX for the

Table 4: Overview of the selection criteria applied to define the two signal regions, the three-tag region and the four-tag region.

	<b>3 tag</b>	<b>4 tag</b>
# reconstructable jets	$\geq 4$	$\geq 5$
# reconstructable jets with CSV > 0.80	3	4
# tight leptons	1	1
# additional loose leptons	0	0
$\cancel{E}_T$	$> 35/45 \text{ GeV}(\mu/\text{e})$	$> 35/45 \text{ GeV}(\mu/\text{e})$

291 electron channel.

292 An event in the muon (electron) channel is required to contain exactly one “tight” muon (elec-  
293 tron), as defined in Section 3. In order to suppress the contribution from Drell–Yan and other  
294 processes in which multiple prompt leptons are produced, an event is rejected if an additional  
295 “loose” muon or electron is found, regardless of the channel.

296 The final state of a signal event (see Fig. 3) contains five quarks, all but one being of b flavor. The  
297 b quark produced in the strong vertex is often forward and might miss the detector acceptance.  
298 This suggests an event selection of either at least four jets with exactly three of them b-tagged  
299 (3 tag) or at least five jets with exactly four of them b-tagged (4 tag)).

300 One major change compared to the analysis at 8 TeV is the migration from the tight b-tagging  
301 working point to the medium working point. A jet is b-tagged if the output of the CSVv2 algo-  
302 rithm exceeds a value of 0.8. The tagging efficiencies for the medium working point improved  
303 with regard to Run-I, therefore the expected significance of the analysis is going to be increased  
304 significantly. Additionally, the migration to the medium working point delivers higher event  
305 counts in the MC signal samples. A high number of signal events ensures a coherent behavior  
306 of the tHq reconstruction and of the classification, as both have to be trained with a significant  
307 amount of signal events that afterwards are discarded from the analysis. Another measure to  
308 ensure a reasonably high event count is the combination of the muon and electron channel into  
309 a common lepton channel. Another small change in comparison to the 8 TeV analysis is that  
310 jets that are considered to be b-tagged need to satisfy  $p_T > 30 \text{ GeV}/c$ .

311 The jets of the central region are part of the jet collection if their transverse momentum is larger  
312 than  $20 \text{ GeV}/c$ . Reconstructable jets are defined as satisfying  $p_T > 30 \text{ GeV}/c$ , if they are recon-  
313 structed in the central region of the detector, and satisfying  $p_T > 40 \text{ GeV}/c$ , they are recon-  
314 structed in the forward region with  $|\eta| > 2.4$ . Each event is required to contain at least four  
315 reconstructable jets in the 3 tag region and at least five reconstructable jets in the 4 tag region.  
316 This requirement significantly reduces the amount of W+jets and QCD events with only a mod-  
317 erate impact on the signal. Although these backgrounds have a small impact compared to  $t\bar{t}$ ,  
318 their modeling is known to be difficult in the considered phase space. To further reject QCD  
319 multi-jet events a missing transverse energy selection is applied, with thresholds optimized per  
320 channel:  $\cancel{E}_T > 35 \text{ GeV}$  in the muon channel,  $\cancel{E}_T > 45 \text{ GeV}$  in the electron channel.

321 Table 4 summarizes the event selection for the 3 tag and 4 tag regions.

322 The expected event yields after event selection are given in Table 5. The different signal-to-  
323 background ratio regions with three and four b-tagged jets are considered independently. The  
324 errors include both systematic and statistical uncertainties.

325 Figures 9 and 10 show some basic variables like lepton  $p_T$ , jet  $p_T$  and  $\cancel{E}_T$  in a  $t\bar{t}$  enriched control  
326 region (2 tag), that requires two medium b-tagged jets but is otherwise identical to the 3 tag

Table 5: Event yields for tHq and tHW signal (for the SM and ITC scenarios) as well as the various background processes in the two signal regions. The uncertainties include both systematic and statistical uncertainties. Additionally, the numbers of observed events in data are shown.

	3 tag	4 tag
t <bar>t&gt;+LF</bar>	$2119 \pm 651$	$21.3 \pm 21.6$
t <bar>t&gt;+c<bar>c</bar></bar>	$852 \pm 624$	$39 \pm 46$
t <bar>t&gt;+b</bar>	$324 \pm 203$	$18.7 \pm 15.3$
t <bar>t&gt;+b<bar>b</bar></bar>	$333 \pm 298$	$71 \pm 67$
t <bar>t&gt;+2b</bar>	$177 \pm 102$	$13.0 \pm 9.6$
Single top	$156 \pm 44$	$6.0 \pm 2.4$
t <bar>t&gt;H</bar>	$20.3 \pm 9.7$	$5.3 \pm 2.9$
t <bar>t&gt;Z</bar>	$9.4 \pm 2.3$	$1.8 \pm 1.7$
t <bar>t&gt;W</bar>	$8.0 \pm 2.5$	$0.4 \pm 0.4$
W+jets	$42 \pm 35$	$0.0 \pm 0.0$
Z+jets	$10.2 \pm 5.0$	$0.0 \pm 0.0$
Sum of Backgrounds	$4051 \pm 978$	$177 \pm 86$
tHq (SM)	$0.77 \pm 0.21$	$0.12 \pm 0.04$
tHW (SM)	$0.61 \pm 0.09$	$0.09 \pm 0.02$
tHq (ITC)	$11.2 \pm 3.1$	$1.7 \pm 0.6$
tHW (ITC)	$6.7 \pm 1.0$	$1.1 \pm 0.3$
Observed	<b>3603</b>	<b>171</b>

327 region. The overall good agreement of the simulation with the data gives trust in applying  
 328 the selection criteria of Table 4 and reconstructing more complex objects out of these basic  
 329 quantities.

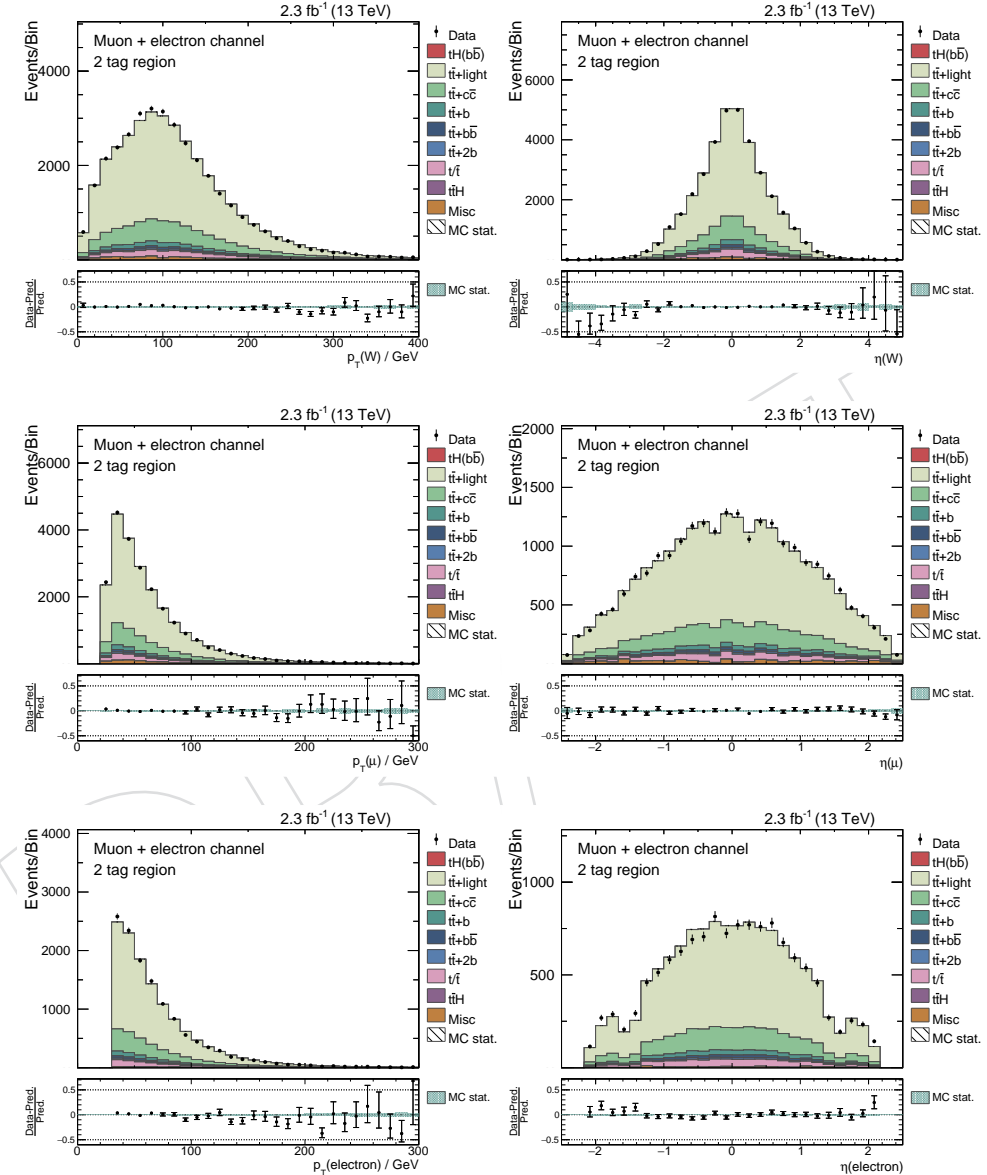


Figure 9: The transverse momentum and  $\eta$  of the reconstructed W boson, lepton  $p_T$  and  $\eta$  in the  $t\bar{t}$  control region. All corrections have been applied; MC is normalized to data.

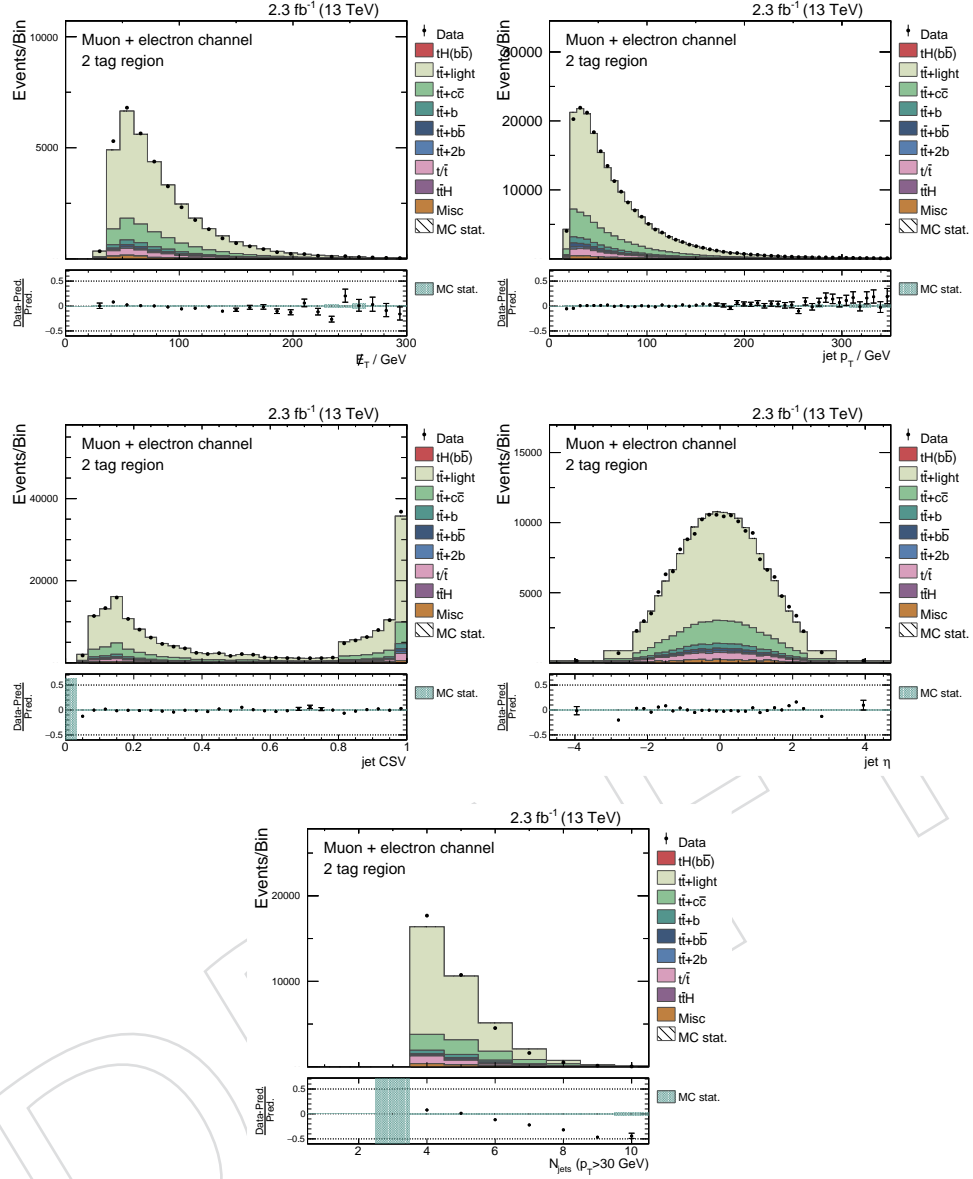


Figure 10:  $\cancel{E}_T$ , the jet  $p_T$ -, CSV- and  $\eta$ -spectrum, and the number of jets for  $p_T > 30 \text{ GeV}/c$  in the  $t\bar{t}$  control region. All corrections have been applied; MC is normalized to data.

## 330 6 Event interpretation

### 331 6.1 Jet assignment under the tHq hypothesis

332 The goal of the procedure described here is to find reconstructed jets that correspond to each of  
 333 the four quarks in the final state  $tHq \rightarrow 3bql\nu$ . There are two possible approaches: either each  
 334 object (the top quark, the Higgs boson, and the recoil jet) can be reconstructed independently or  
 335 the whole event can be reconstructed in one step. For each quark there is a non-zero probability  
 336 that it does not give birth to a reconstructed jet. The jet might fail quality selection or detector  
 337 acceptance cuts, it might merge with other jets, or it can split into two jets. The approach of  
 338 independent reconstructions can be considered to be more robust a priori, albeit more difficult  
 339 to implement. For example, one could reconstruct the Higgs boson even when the jet from the  
 340 decay of the top quark is missing. In contrast, the global reconstruction method assumes that  
 341 no jet is missing, and its behavior is undefined otherwise.

342 Both approaches have been implemented and compared. They have been found to give equal  
 343 discrimination power to the classification BDT, and for this reason the simpler global recon-  
 344 struction is kept. The method is described in detail below.

345 In a simulated signal event, the procedure considers all possible ways to choose four recon-  
 346 structed jets and assign them to the four quarks in the final state. One particular way represents  
 347 a possible interpretation of the event. If all jets in an interpretation are matched to appropriate  
 348 quarks within a cone of size  $\Delta R = \sqrt{\Delta\eta^2 + \Delta\phi^2} = 0.3$ , the interpretation is considered correct.  
 349 Otherwise, if the angular distance  $\Delta R$  from at least one quark to the jet assigned to it is larger  
 350 than the threshold 0.3, the interpretation is considered to be wrong. By construction, one re-  
 351 constructed jet can be assigned to one quark at maximum. Due to radiation, jets outside of the  
 352 detector acceptance, and other reasons, not every event has a correct interpretation.

353 To simplify the jet combinatorics, a few simple constraints are imposed during the construction  
 354 of potential event interpretations. The b-quark jets from decays of the top quark and the Higgs  
 355 boson are required to be central ( $|\eta| < 2.4$ ). In addition, only jets that are not b-tagged can be  
 356 assigned to the recoil quark. These requirements are met by  $\sim 99\%$  of correct interpretations,  
 357 while they limit the number of wrong interpretations.

358 The jet assignment is performed with the help of dedicated BDTs, which are trained to dis-  
 359tinguish correct and wrong interpretations. The training is done separately for all analyzed  
 360 points in the  $\kappa_t - \kappa_V$  plane. These BDTs are applied to the selected events and for each event  
 361 and each  $\kappa_t - \kappa_V$  scenario the event interpretation with the highest output value of the BDT  
 362 discriminant is then chosen. The parameter settings of the used BDTs are listed in Table 6. Each  
 363 tHq event used for training gives one entry to the signal category (the correct interpretation)  
 364 and one entry to the background category (one randomly chosen wrong interpretation). If an  
 365 event does not have a correct interpretation, it is not used for training. Each interpretation is  
 366 described through a set of observables provided in Table 7, which were chosen as variables  
 367 that have a decent separation power and are not expected to be too correlated. Distributions of  
 368 correct and wrong interpretations over these variables are shown in Fig. 12. Distributions over  
 369 the BDT response is provided in Fig. 13. A summary of the reconstruction efficiency in the 3  
 370 tag and 4 tag region is given by Fig. 11, showing the improved efficiency when using the BDT  
 371 approach. The efficiency is calculated with respect to the number of events for which a correct  
 372 assignment (as defined above) exists. It is noticeable that the  $\chi^2$  reconstruction, which performs  
 373 clearly worse in the assignment for all central partons, can outperform the BDT reconstruction  
 374 in the assignment of the light forward jet. The  $\chi^2$  reconstruction simply chooses the jet with the  
 375 highest absolute pseudorapidity as light jet. This way the correct light jet can be selected more

Table 6: Parameter settings used for the training of the employed BDTs for the two reconstructions in the TMVA software package. The lower number of trees is used for points that have otherwise shown signs of overtraining. These points include the following  $(\kappa_t|\kappa_V)$ -value pairs: (1|1), (1.25|1), (1.5|1), (1.5|1.5), (2|1.5) and (0.5|0.5). After this reduction no sign of overtraining is found.

Parameter	Value
NTrees	400/150
MinNodeSize	1
MaxDepth	3
BooseteType	AdaBoost
nCuts	20
AdaBoostBeta	0.3
SeparationType	GiniIndex

376 often, but all correlations of the light quark to the other partons are ignored. By applying this  
 377 procedure to background events the separation between signal events and background events  
 378 actually becomes worse, as jets in the forward region, that would have otherwise been ignored  
 379 by the BDT reconstruction, are selected as light jet. The separation quality cannot be evaluated  
 380 by a simple visual comparison, both variables, reconstructed light jet and most forward jet,  
 381 have been used separately in the final classification, where the highest absolute pseudorapi-  
 382 dity of an event showed a slightly worse behavior. As figure of merit the AUC was used and a  
 383 small but noticeable reduction can be observed. Additionally, when both variables are used in  
 384 the classification simultaneously, the BDT reconstructed pseudorapidity is chosen as the more  
 385 important variable.

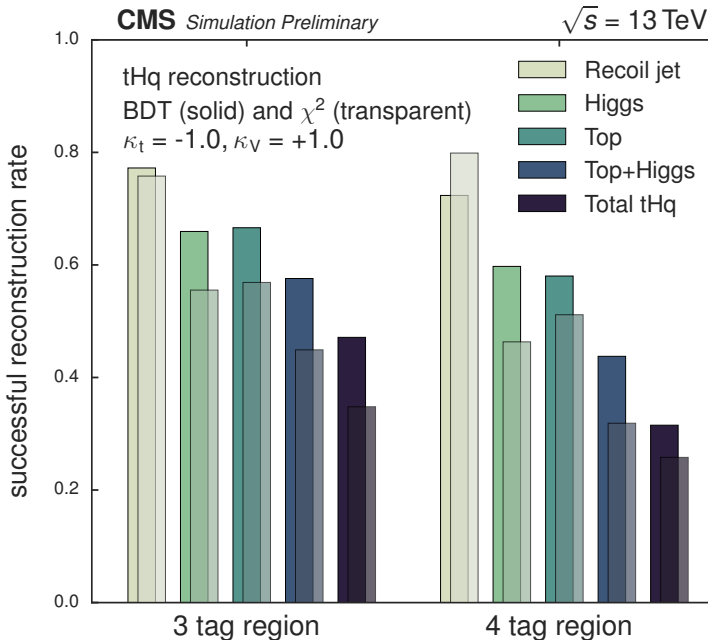


Figure 11: Reconstruction efficiency under the tHq hypothesis in the two signal regions.

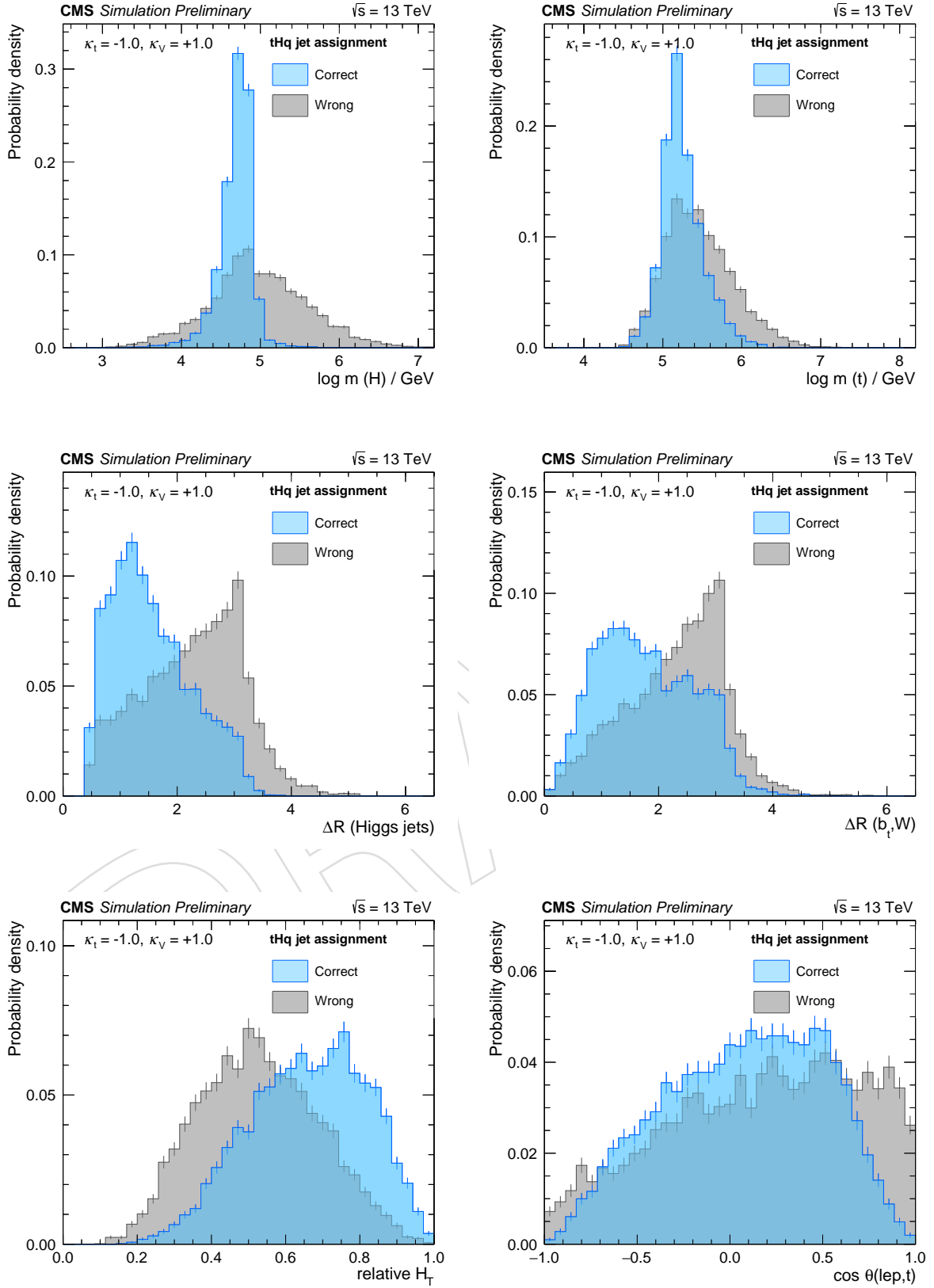


Figure 12: The six most discriminating variables between correct and wrong jet assignments in the tHq reconstruction at  $\sqrt{s} = 13 \text{ TeV}$  are shown sorted by their importance in the training. All distributions are normalized to unit area. The corresponding variable descriptions can be found in Table 7. The remaining variables can be found in Appendix 31 and 32.

Table 7: Input variables for the jet-assignment BDT under the tHq hypothesis sorted by their importance in the training. Instead of the invariant masses and transverse momenta their logarithms are used, as narrow distributions are better suited for the usage in BDT techniques than distributions with long tails. The two jets which are assigned to the Higgs boson are  $p_T$ -ordered.

Variable	Points	Description
<b>log m(H)</b>	14.27	invariant mass of the reconstructed Higgs boson
<b>log m(t)</b>	12.84	invariant mass of the reconstructed top quark
<b><math>\Delta R</math> (Higgs jets)</b>	12.35	$\Delta R$ between the two jets from the Higgs boson decay
<b><math>\Delta R(b_t, W)</math></b>	11.05	$\Delta R$ between jets assigned to the b quark from the top decay and the W boson
<b>relative <math>H_T</math></b>	9.56	percentage of the total transverse momenta (jets, lepton, $E_T$ ) that falls to b jet of the top quark, Higgs jets and light forward jet
<b><math>\cos \theta(t, \ell)</math></b>	8.74	Cosine of the angle from the top quark vector to the sum of top quark and charged lepton in their common restframe
<b>CSV(Higgs jet 2)</b>	7.15	output of the CSVv2 b-tagging algorithm for the second jet assigned to the Higgs boson
<b>CSV(<math>b_t</math>)</b>	7.05	output of the CSVv2 b-tagging algorithm for the jet assigned to the b quark from the top quark decay
<b><math> \eta(\text{light jet}) - \eta(b_t) </math></b>	5.23	absolute difference of pseudorapidities of light forward jet and b of the top quark decay
<b>CSV(Higgs jet 1)</b>	3.96	output of the CSVv2 b-tagging algorithm for the first jet assigned to the Higgs boson
<b><math> \eta(b_t) </math></b>	3.70	pseudorapidity of the jet assigned to the b quark of the top decay
<b><math> \eta(t) - \eta(H) </math></b>	3.27	absolute difference of pseudorapidities of reconstructed top quark and the reconstructed Higgs boson
<b><math>\log \min(p_T(\text{H jets}))</math></b>	3.05	lower transverse momentum of the two jets assigned to the Higgs boson decay products
<b><math> \eta(\text{light jet}) </math></b>	2.47	absolute pseudorapidity of light forward jet
<b><math>\Delta E(\text{light jet}, b_t)</math></b>	2.29	jet energy difference of the light jet and the jet assigned to the b quark from the top quark decay

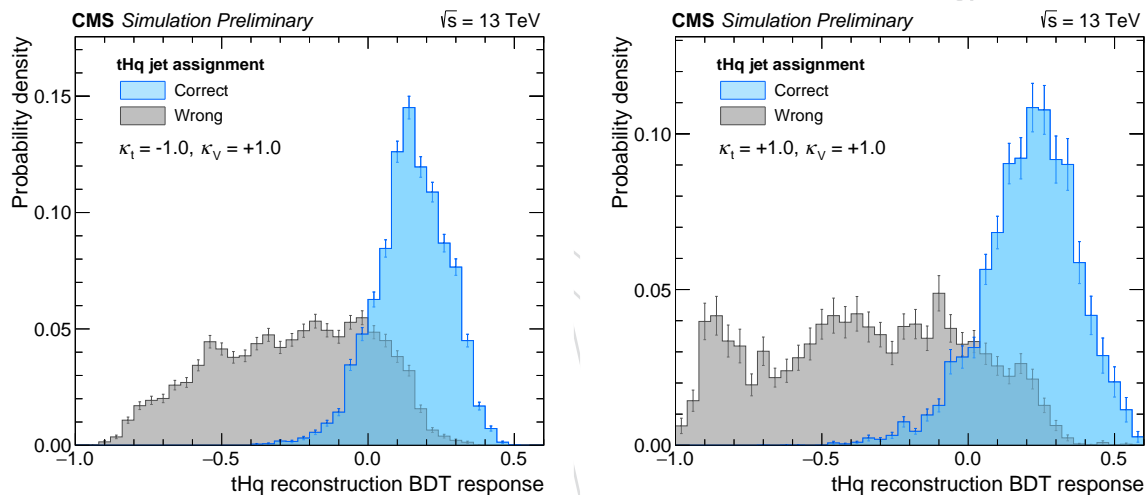


Figure 13: Output values of the tHq reconstruction BDTs for good and bad jet assignments for the coupling case of  $\kappa_t = -1$  and  $\kappa_V = +1$  (left) and of the SM prediction (right).

## 386 6.2 Jet assignment under the $t\bar{t}$ hypothesis

387 Semileptonic  $t\bar{t}$  decays are by far the dominant background in the analysis. In order to provide  
 388 an additional handle to suppress them, a dedicated jet assignment is developed. This allows  
 389 one to define in a natural way observables that are intrinsic for semileptonic  $t\bar{t}$  such as the mass  
 390 of the hadronically decaying top quark.

391 The jet assignment is performed following the same scheme as for the signal process: a BDT is  
 392 trained to discriminate correct and wrong interpretations, and in a new event the interpretation  
 393 with the largest BDT response is chosen. The jet combinatorics challenge is mitigated by a  
 394 requirement that only central b-tagged jets can be assigned to the b-quarks from decays of  
 395 the top quarks. Selected input variables are listed in Table 8, and distributions of correct and  
 396 wrong interpretations are shown in Fig. 16. Distributions over the BDT response is provided  
 397 in Fig. 17. A summary of the reconstruction efficiency in the 3 tag and 4 tag region is given by  
 398 Fig. 15, showing the improved efficiency when using the BDT approach.

399 A validation in the  $t\bar{t}$  control region is performed by comparing the distributions of data and  
 400 MC over the BDT response for the best event interpretation, which is shown in Fig. 14.

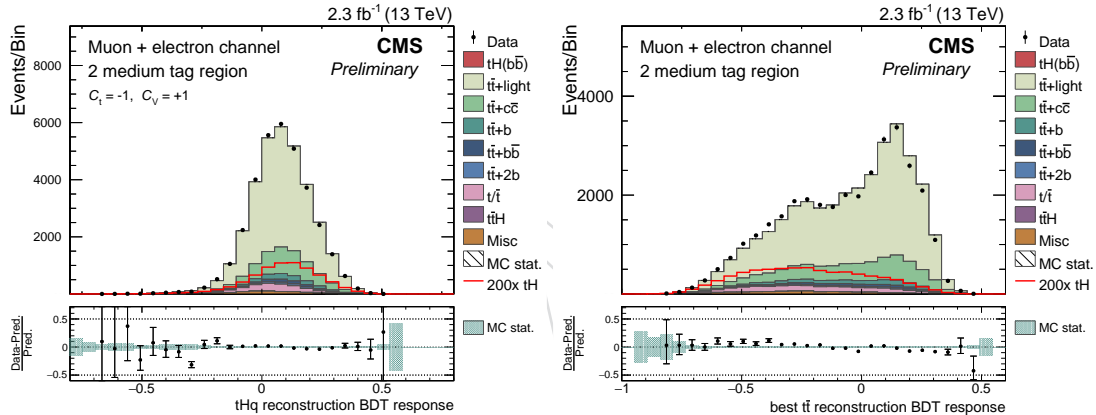


Figure 14: This shows the output of the best reconstruction BDT under the signal and  $t\bar{t}$  hypotheses in the 2 tag region. MC is normalized to data.

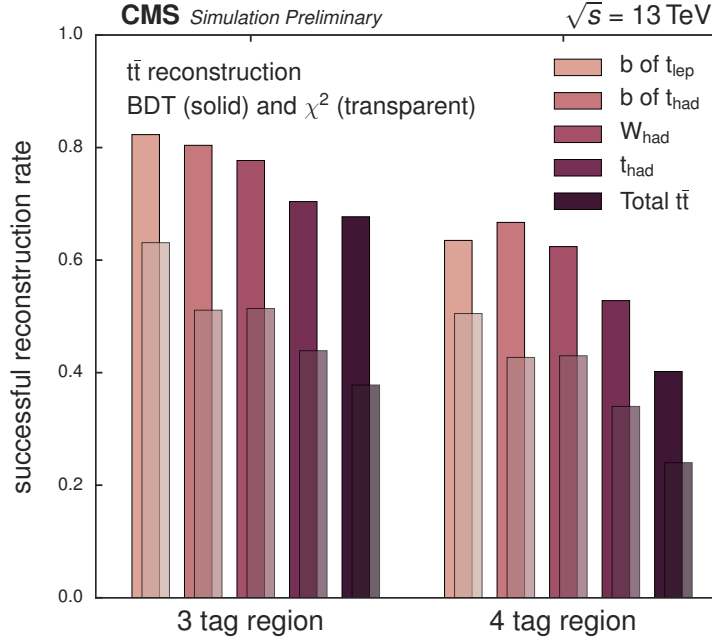


Figure 15: Reconstruction efficiency under the  $t\bar{t}$  hypothesis in the two signal regions.

Table 8: Input variables for the jet-assignment BDT under the  $t\bar{t}$  hypothesis sorted by their importance in the training. Instead of the transverse momenta variables the logarithm of these variables is used, as narrow distributions are better suited for the usage in BDT techniques than distributions with long tails. The two jets which are assigned to the  $W$  boson of  $t_{\text{had}}$  are  $p_T$ -ordered.

Variable	Description
$\log m(W_{\text{had}})$	invariant mass of the two jets assigned to the $W$ boson of $t_{\text{had}}$
$\log (m(t_{\text{had}}) - m(W_{\text{had}}))$	difference between the invariant masses of reconstructed $t_{\text{had}}$ and $W_{\text{had}}$
$\log m(t_{\text{lep}})$	invariant mass of the reconstructed $t_{\text{lep}}$
CSV( $W_{\text{had}}$ jet 1)	CSV output of the first jet assigned to $W_{\text{had}}$
$\Delta R(b_{t_{\text{lep}}}, W_{\text{lep}})$	$\Delta R$ between the $b$ quark of the reconstructed $t_{\text{lep}}$ and $W_{\text{lep}}$
CSV( $W_{\text{had}}$ jet 2)	CSV output of the second jet assigned to $W_{\text{had}}$
$\Delta R(b_{t_{\text{had}}}, W_{\text{had}})$	$\Delta R$ between the $b$ quark of the reconstructed $t_{\text{had}}$ and $W_{\text{had}}$
relative $H_T$	percentage of the total transverse momentum (jets, lepton, $E_T$ ) that falls to the reconstructed $t_{\text{had}}$ and $t_{\text{lep}}$
$\Delta R(W_{\text{had}})$	$\Delta R$ between the two jets assigned to the $W$ boson of $t_{\text{had}}$
$\log p_T(t_{\text{had}})$	transverse momentum of the reconstructed $t_{\text{had}}$
$\log p_T(t_{\text{lep}})$	transverse momentum of the reconstructed $t_{\text{lep}}$

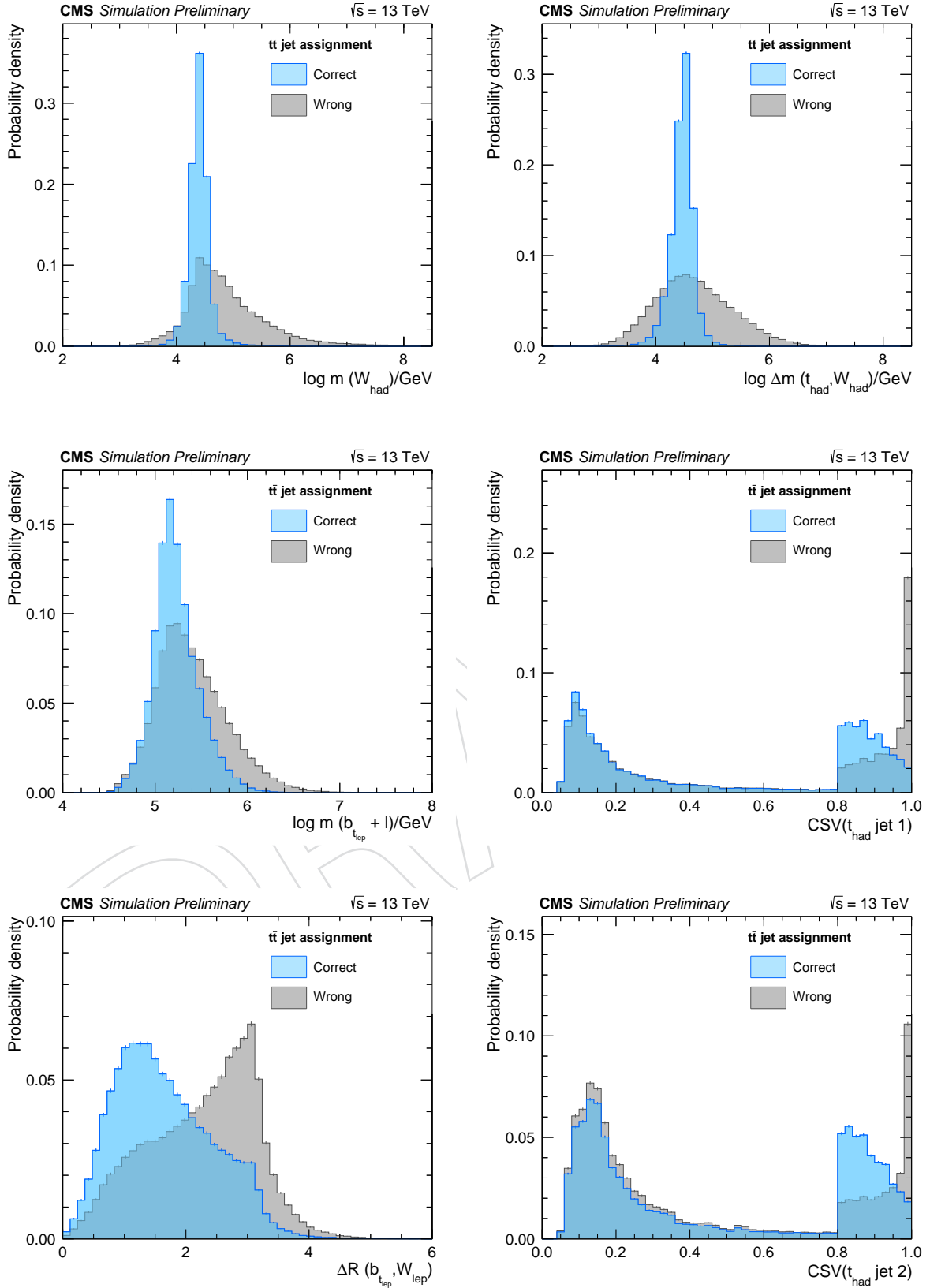


Figure 16: The six most discriminating variables between correct and wrong jet assignments in the  $t\bar{t}$  reconstruction at  $\sqrt{s} = 13 \text{ TeV}$  are shown sorted by their importance in the training. All distributions are normalized to unit area. The corresponding variable descriptions can be found in Table 8. The remaining variables can be found in Fig. 33 in Appendix B.

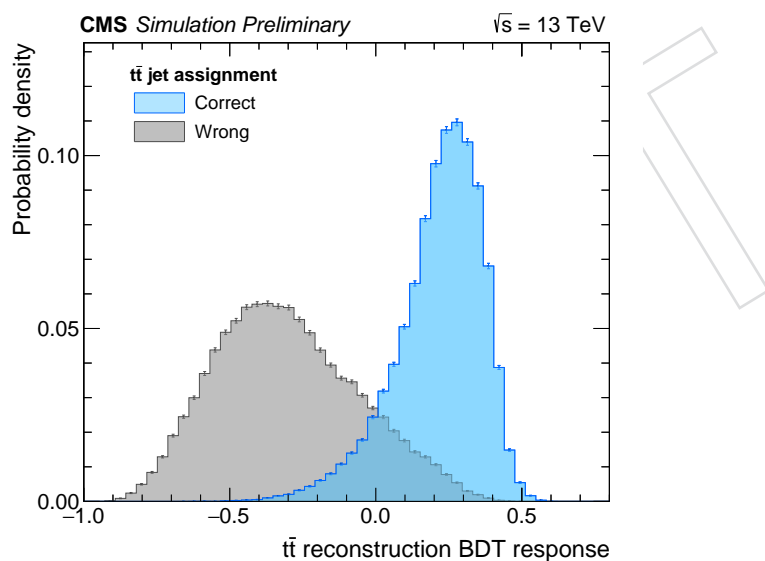


Figure 17: Output values of the  $t\bar{t}$  reconstruction BDTs for good and bad jet assignments. Only  $t\bar{t}$  events are used.

## 401 7 Event classification

402 After the two types of reconstructions every event is supplied with 51 jet assignments under the  
 403 tHq hypothesis and one under the  $t\bar{t}$  hypothesis. These reconstructed objects build the basis for  
 404 most of the variables, which are used in a multivariate classifier to separate signal events from  
 405 background events. The classification has to be performed separately for each coupling point  
 406 of the  $\kappa_t - \kappa_V$  plane, where for each point the identical variable set is used, but the observables  
 407 based on reconstructed objects of the tHq process will differ for every studied coupling point.

408 The training parameters of the classification BDTs can be found in table 9 – they are basically  
 409 the same as in the reconstruction BDTs, a setting which proved to be a good compromise be-  
 410 tween performance and robustness against overtraining. The only difference is in the number  
 411 of trees that are used in scenarios that would have shown signs of overtraining if using more  
 412 trees. Similar to what was observed in the tHq reconstruction, coupling pairs that correspond  
 413 to the lowest cross sections and thus have fewer effective events in the training are prone to  
 414 overtraining. Hence, these points are trained with a lower number of trees (see Table 6) to  
 415 mitigate the overtraining effect.

416 The training is performed in the 3 tag region, where only the tHq process is used as signal input.  
 417 The BDT is trained with background events from a mixture of semileptonic  $t\bar{t}$ , fullleptonic  $t\bar{t}$ ,  
 418 and  $t\bar{t}H$ . The background events are scaled to their predicted cross sections and the signal is  
 419 scaled such that the integral coincides with the integral of the background events.

420 A total of 15 different variables is used; a description of the variables and their averaged im-  
 421 portance over all 51 trainings can be found in Table 10. The employed variables are shown in  
 422 Figures 21 and 22 for signal and background events. A good modeling of the employed vari-  
 423 ables by the simulation is validated by comparing the distributions from simulation and data  
 424 samples. The resulting distributions can be found in Figures 21 and 22, 23 and 24, and 25 and  
 425 26 for the 2 tag region, 3 tag, and 4 tag region, respectively.

426 Each of the 51 trainings is evaluated and checked for possible signs of overtraining. If overtrain-  
 427 ing occurred, the number of trees in the training is reduced until no overtraining is observed  
 428 anymore. The response of the training sample and of a disjoint testing sample for the nomi-  
 429 nal coupling point of  $\kappa_t = -1$  and  $\kappa_V = +1$  and for the couplings predicted by the standard  
 430 model can be found in Figure 18. The BDT responses show a clear separation between sig-  
 431 nals events and background events and the testing sample reproduces the shape of the output,  
 432 hence giving confidence in the training of the classifier.

433 Subsequently, the classifier is applied to simulation samples and data samples alike. As the  
 434 input variables already are well modeled in the simulation a good agreement between data  
 435 and simulation in the classifier output is expected. The distributions in Figure 27, which show  
 436 the classifier output for the  $\kappa_t = -1$  and  $\kappa_V = +1$  and the standard model scenario in the  $t\bar{t}$   
 437 control region, confirm this expectation, as both classification outputs agree well for data and  
 438 simulation. The different shape of the BDT output for the two depicted coupling points is a  
 439 direct consequence of the reduced number of trees in the classification training for the point  
 440 predicted by the standard model.

Table 9: Parameter settings used for the BDTs employed in the classification. The lower number of trees is used for points in the  $\kappa_t - \kappa_V$  plane that have otherwise shown signs of overtraining. For  $\kappa_V = 1.5$  this includes all points with  $\kappa_t \geq 0.5$ , for  $\kappa_V = 1$  all points satisfying  $\kappa_t \geq 0.75$  and for points with  $\kappa_V = 0.5$  the tree number is reduced if  $0.25 \leq \kappa_t \leq 2.0$ . These points correspond to the points with the lowest cross sections and due to the reweighting lead to a lower number of effective signal events in the training of the classification. After this reduction no sign of overtraining is found.

Parameter	Value
NTrees	400/100
MinNodeSize	1
MaxDepth	3
BoostType	AdaBoost
nCuts	20
AdaBoostBeta	0.3
SeparationType	GiniIndex

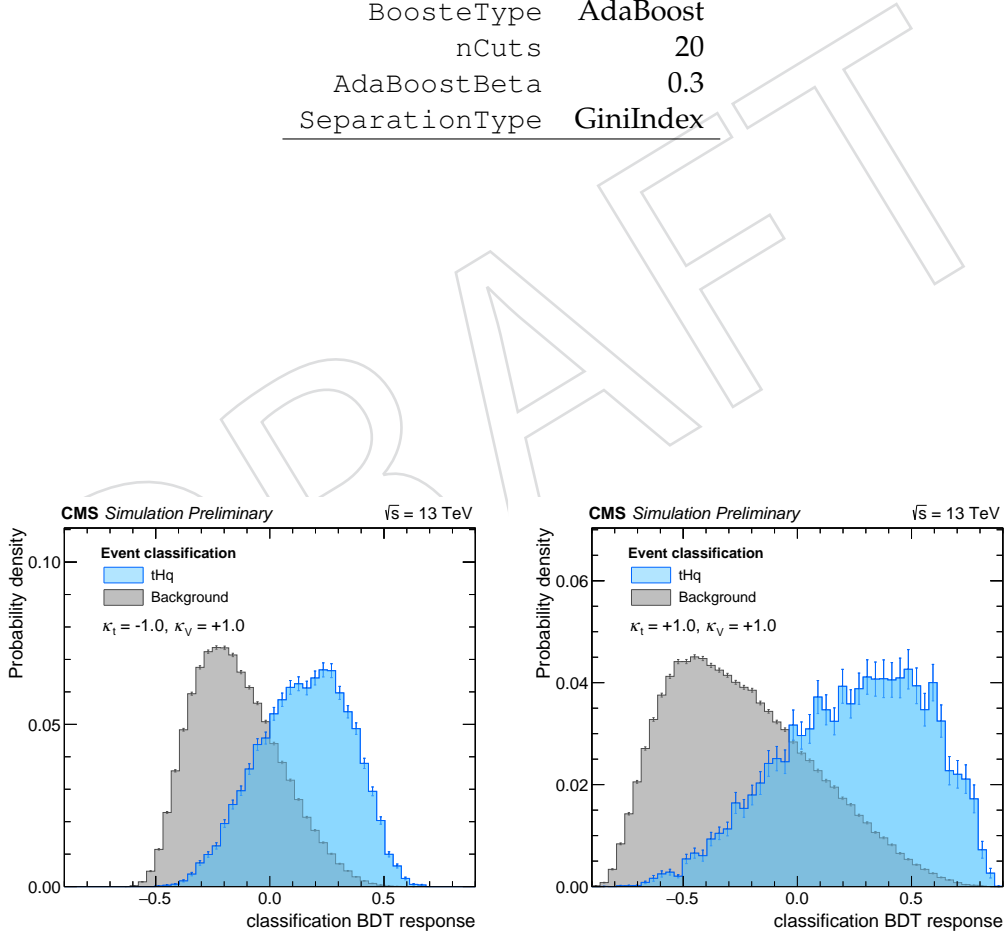


Figure 18: Response values of the classification BDTs for the coupling case of  $\kappa_t = -1$  and  $\kappa_V = +1$  (left) and of the SM prediction (right). The background consists of  $t\bar{t}$  and  $t\bar{t}H$  events.

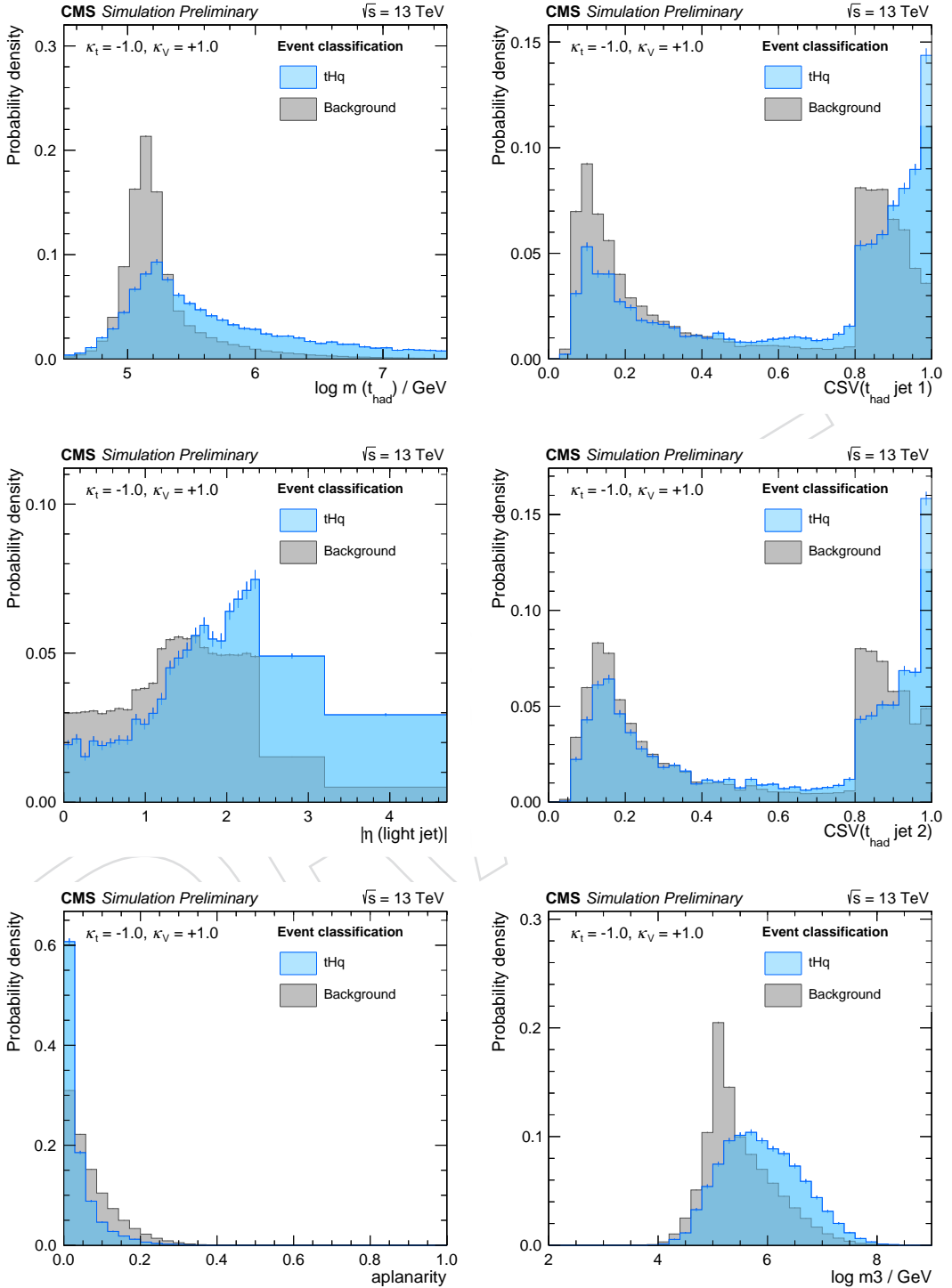


Figure 19: Normalized distributions of the input variables for the classification BDT in the muon + electron channel in the 3 tag region.

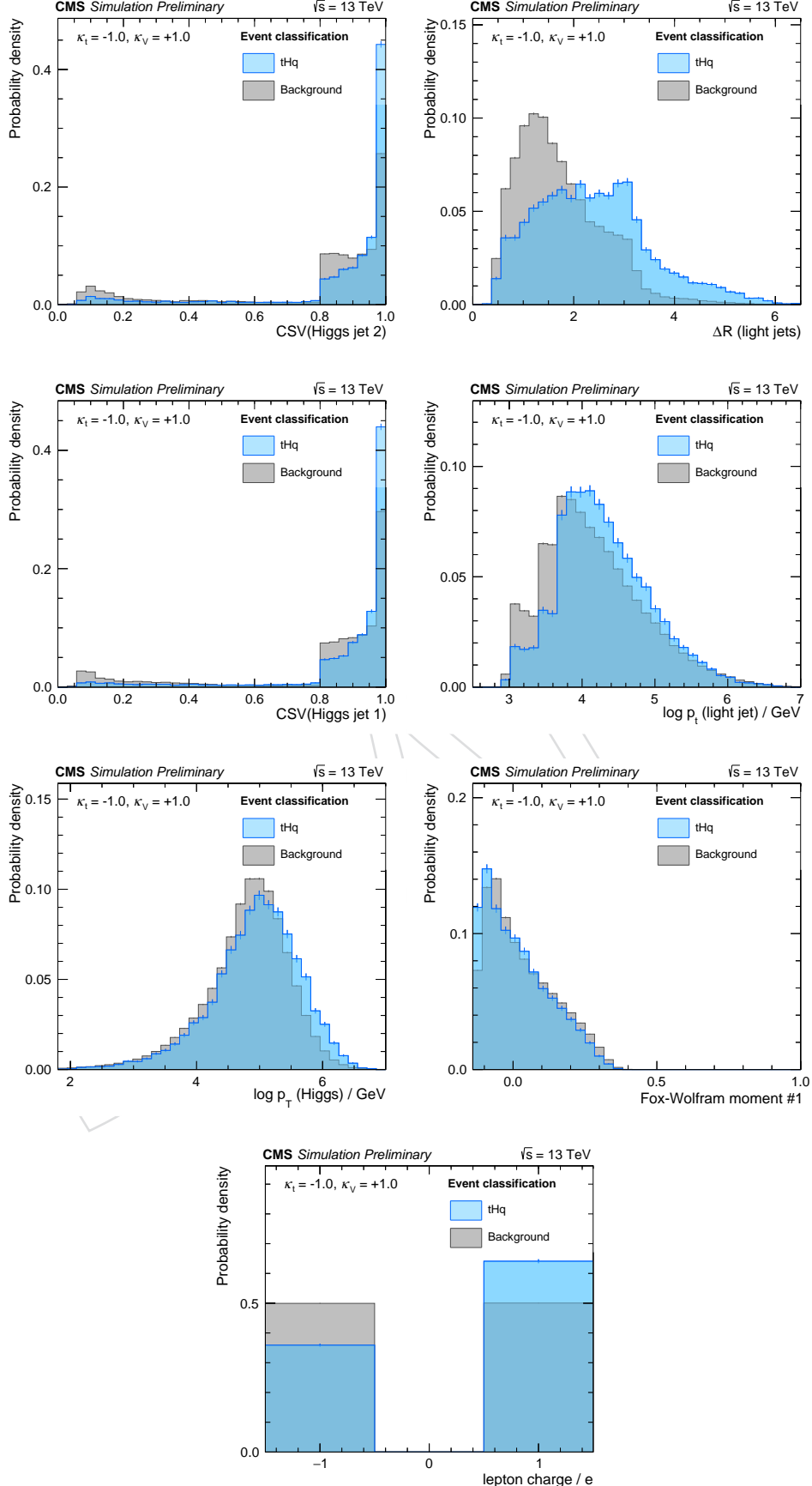


Figure 20: Normalized distributions of the input variables for the classification BDT in the muon + electron channel in the 3 tag region.

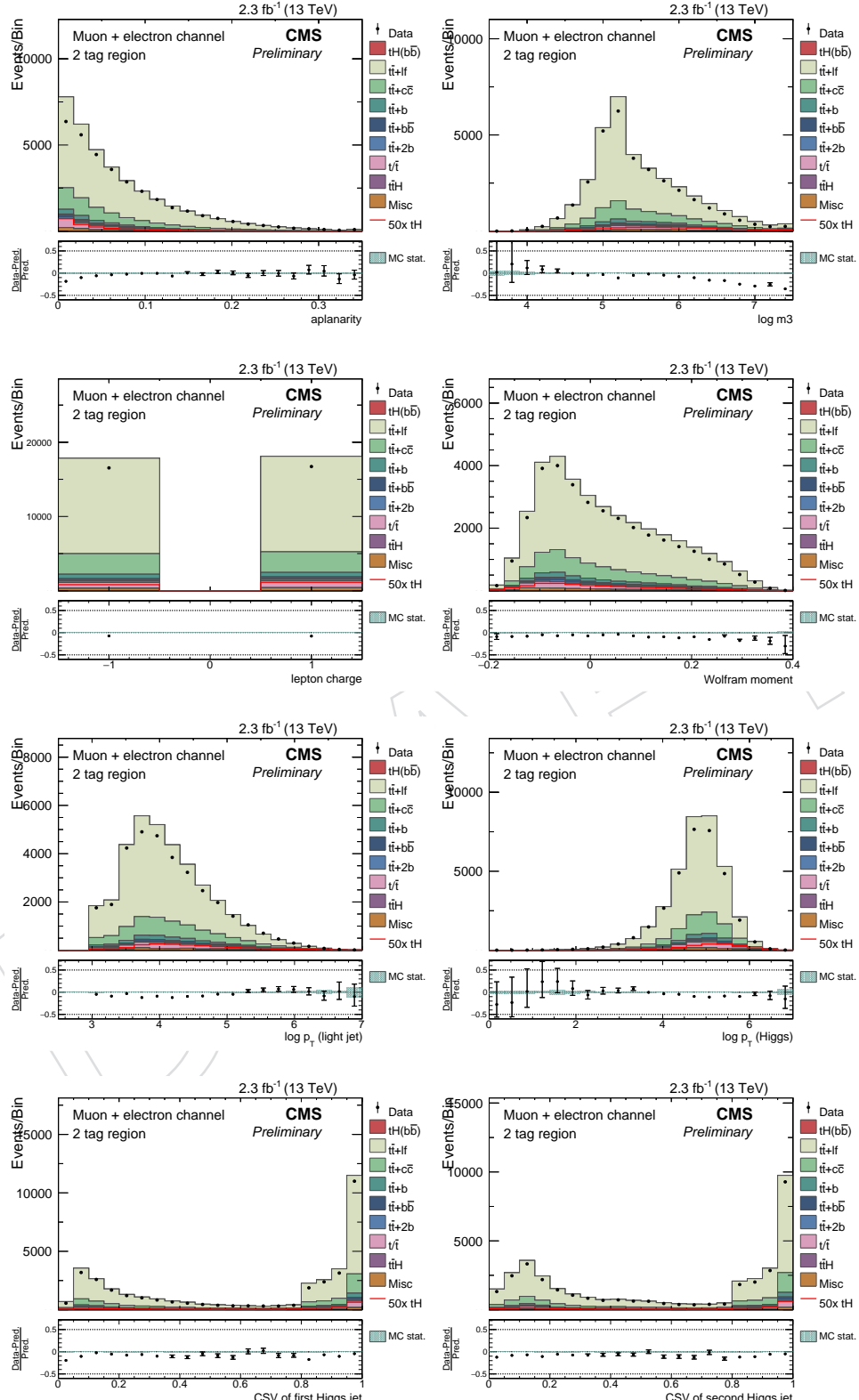


Figure 21: Distributions of the input variables for the classification BDT for the combined muon + electron channel. MC is normalized to prediction. All MC weights are applied.

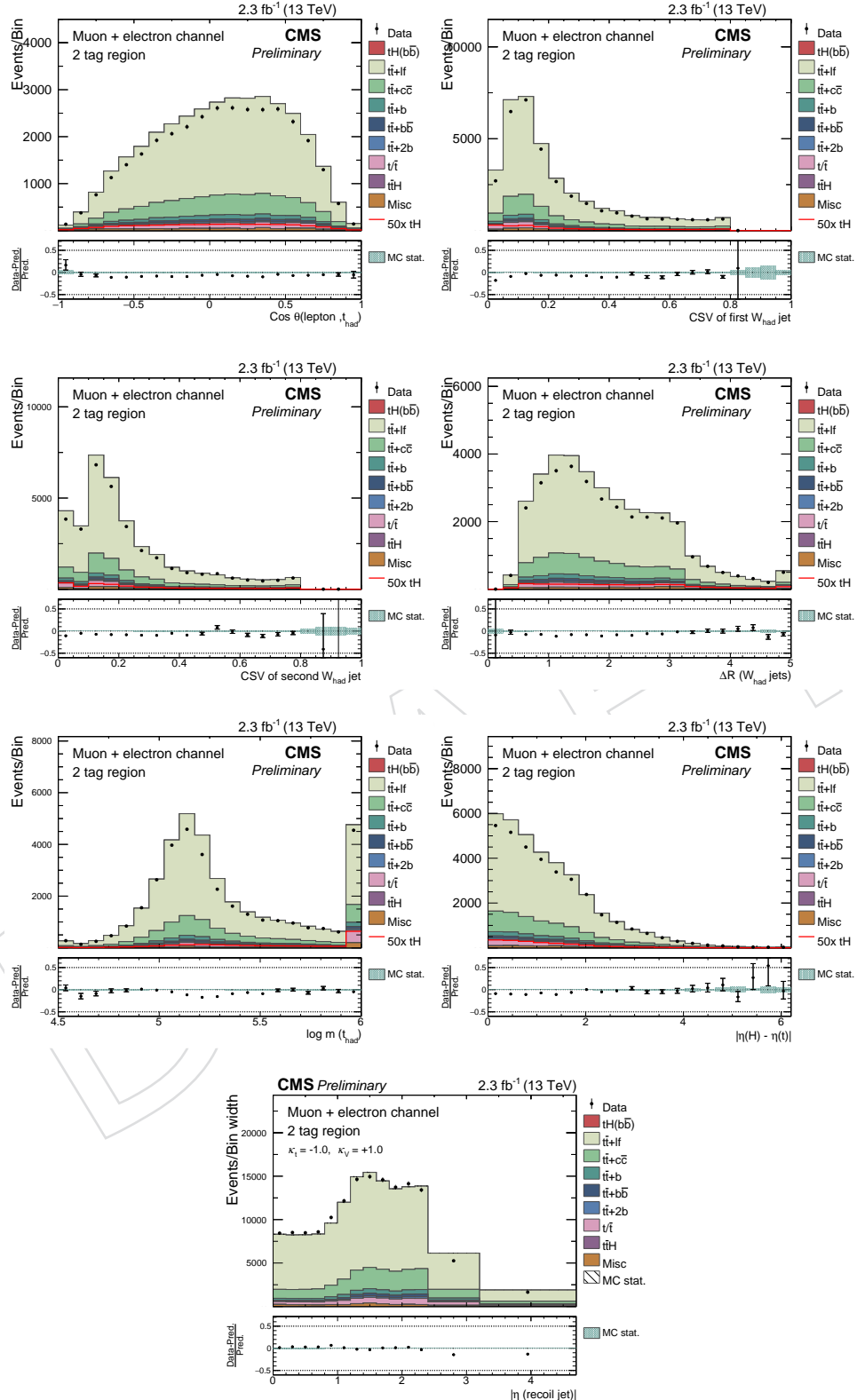


Figure 22: Distributions of the input variables for the classification BDT for the combined muon + electron channel, continued. MC is normalized to prediction. All MC weights are applied.

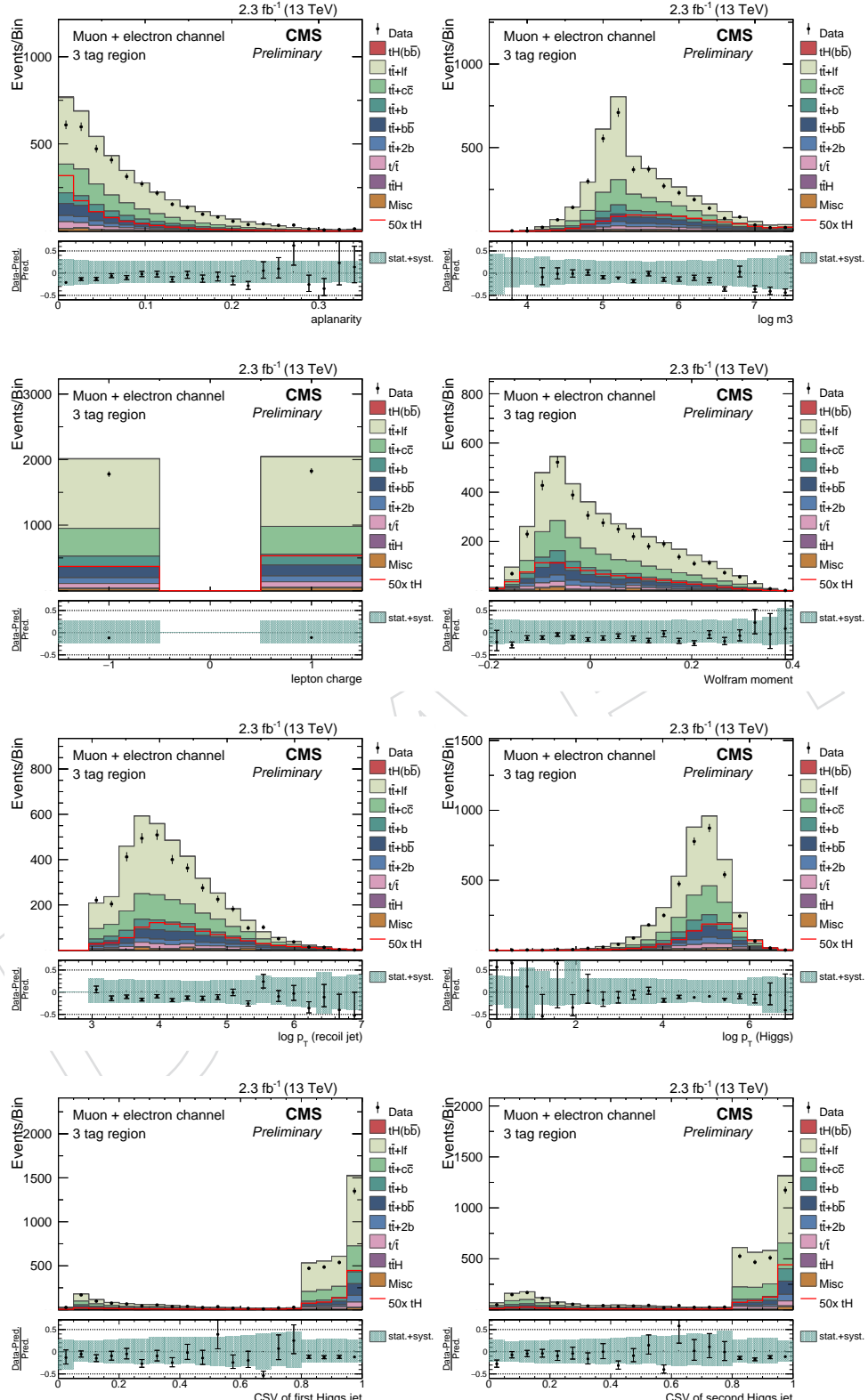


Figure 23: Distributions of the input variables for the classification BDT for the combined muon + electron channel. MC is normalized to prediction. All MC weights are applied.

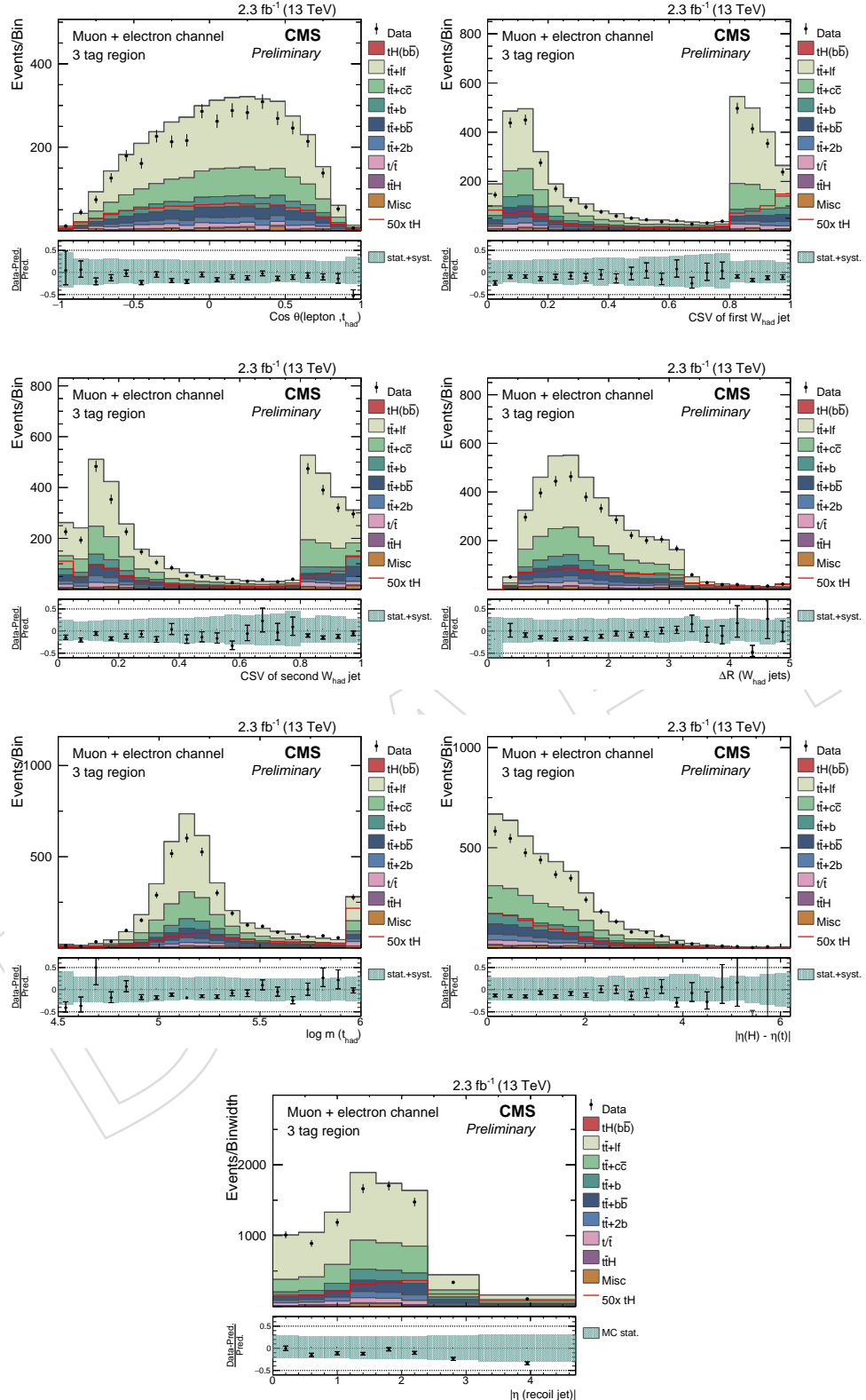


Figure 24: Distributions of the input variables for the classification BDT for the combined muon + electron channel, continued. MC is normalized to prediction. All MC weights are applied.

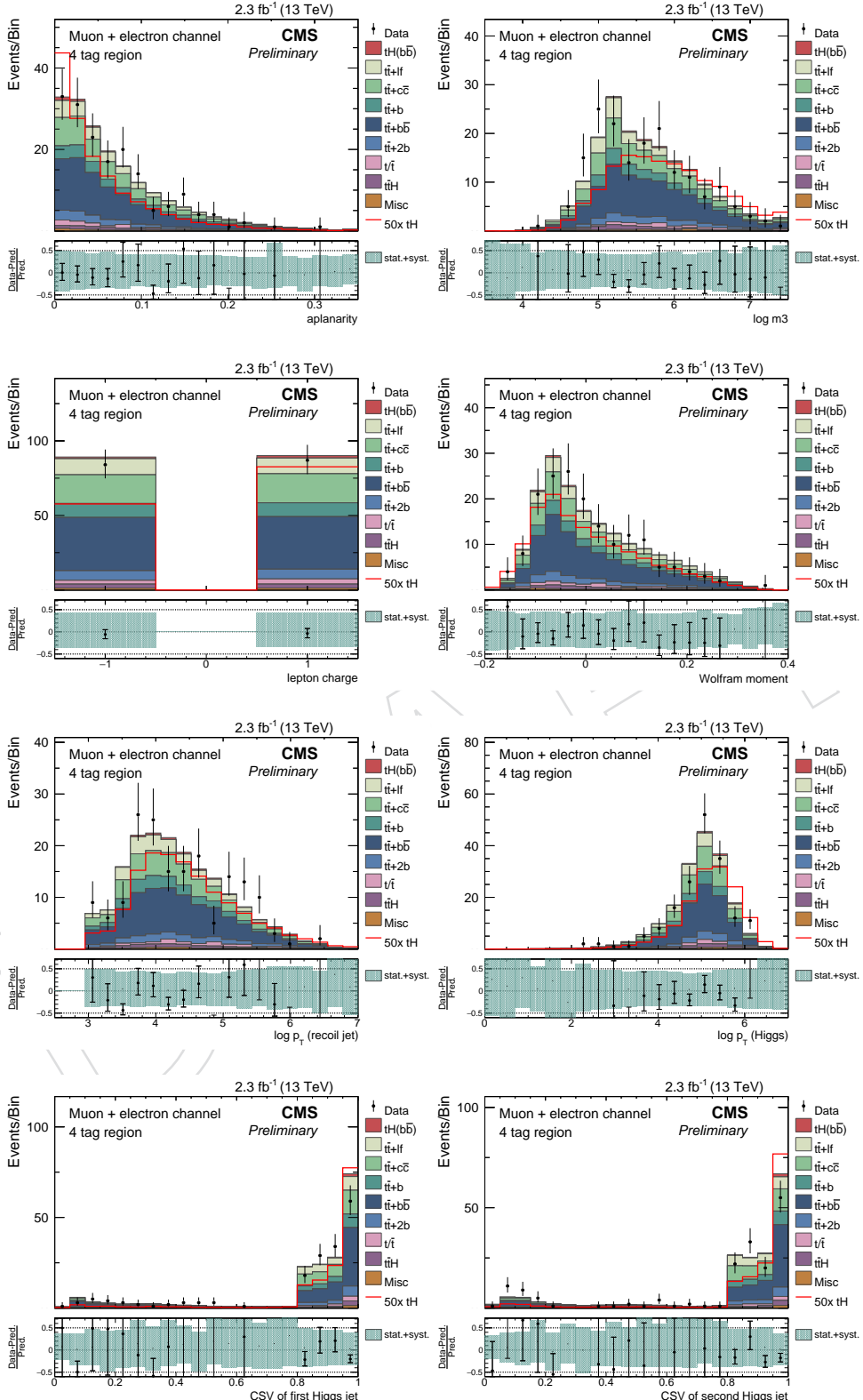


Figure 25: Distributions of the input variables for the classification BDT for the combined muon + electron channel. MC is normalized to prediction. All MC weights are applied.

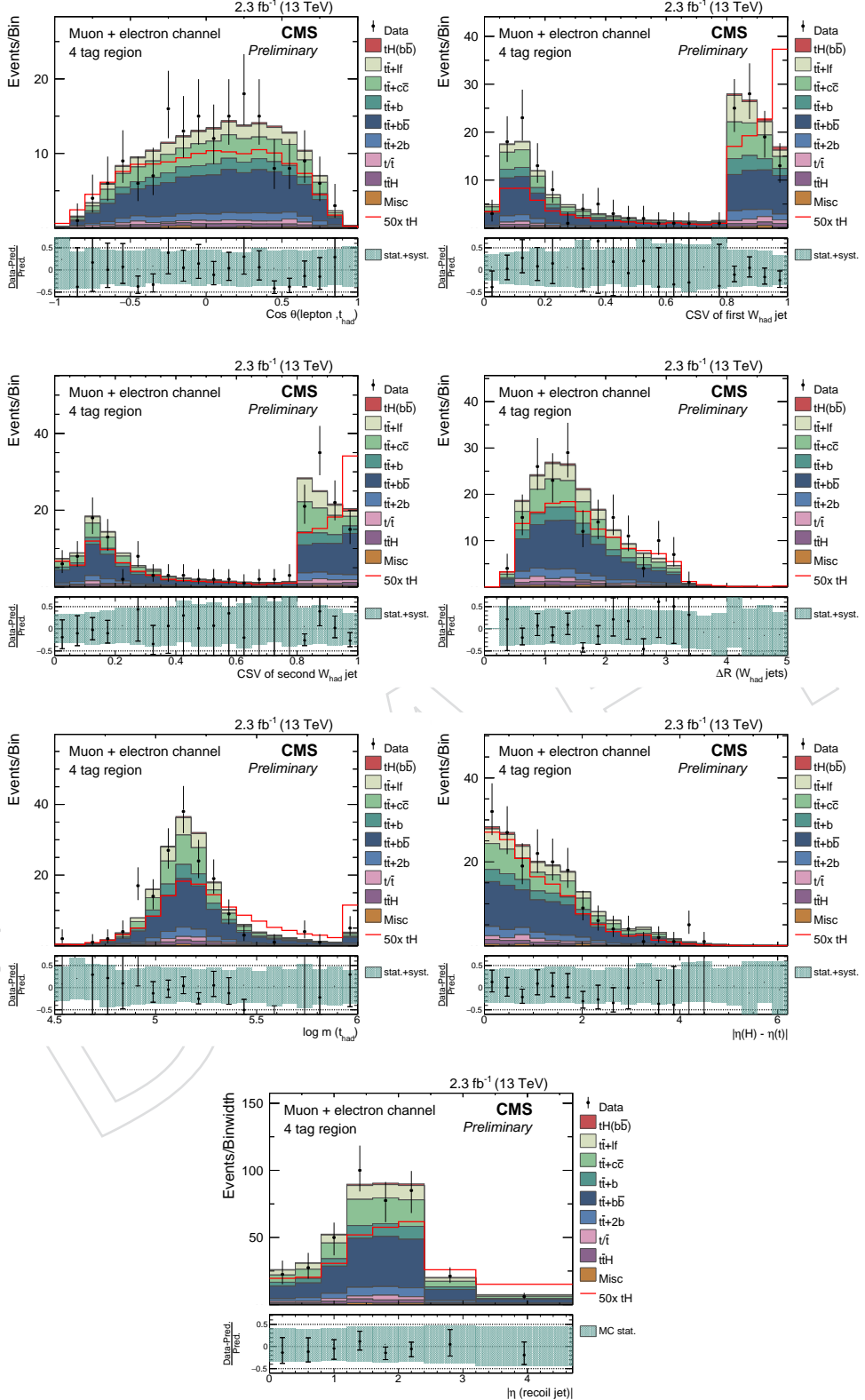


Figure 26: Distributions of the input variables for the classification BDT for the combined muon + electron channel, continued. MC is normalized to prediction. All MC weights are applied.

Table 10: Description of variables used in the classification and their importance ranking in the training. There are three types of variables: variables independent of any reconstruction, variables based on objects reconstructed under the  $t\bar{t}$  hypothesis, and variables based on objects reconstructed under the  $tHq$  hypothesis. The logarithm transformation is used to smoothen and constrain broad distributions to a more narrow range.

Variable	Points	Description
aplanarity	10.58	aplanarity of the event
$\log m_3$	9.31	invariant mass of three hardest jets in the event
Fox-Wolfram #1	3.01	first Fox-Wolfram moment of the event
$q(\ell)$	2.00	electric charge of the lepton
$\log m(t_{had})$	13.27	invariant mass of $t_{had}$
CSV ( $W_{had}$ jet 1)	11.74	CSV output of the first jet assigned to $W_{had}$
$\Delta R$ ( $W_{had}$ jets)	8.68	$\Delta R$ between the two light jets from the decay of $W_{had}$
CSV ( $W_{had}$ jet 2)	8.23	CSV output of the second jet assigned to $W_{had}$
$ \eta(\text{light jet}) $	12.11	pseudorapidity of light forward jet
CSV (Higgs jet 2)	8.68	CSV output of the second jet assigned to the Higgs boson
CSV (Higgs jet 1)	8.45	CSV output of the first jet assigned to the Higgs boson
$\log p_T$ (light jet)	4.23	transverse momentum of the recoil jet
$\log p_T$ (Higgs)	3.86	transverse momentum of the Higgs boson
$ \eta(t) - \eta(H) $	2.49	absolute pseudorapidity difference of reconstructed Higgs boson and reconstructed top quark
$\cos \theta(t, \ell)$	0.11	Cosine of the angle from the top quark vector to the sum of top quark and charged lepton in their common restframe

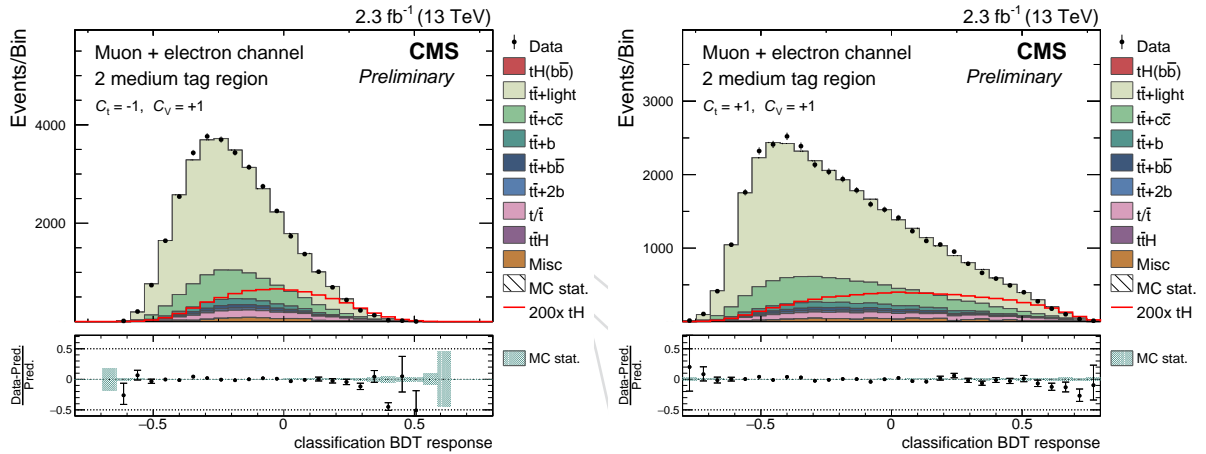


Figure 27: Simulation to data comparisons for the output of the classification in the  $t\bar{t}$  control region at 13 TeV. The training output is shown for the  $\kappa_t = -1$  and  $\kappa_V = +1$  coupling point (left) and the coupling point predicted by the SM (right). In both distributions a good agreement between simulation and data is observed. The simulation is scaled to match the event yields observed in data and all MC weights are applied.

## 441 8 Uncertainty treatment

### 442 Experimental uncertainties

443 **Luminosity (rate)** An overall uncertainty on the luminosity measurement at  $\sqrt{s} = 13 \text{ TeV}$  of  
 444 2.7% [18] is applied to all processes in both signal regions.

445 **Lepton Efficiencies (rate)** To account for uncertainties in the estimation of the corrected lepton  
 446 efficiencies a conservative overall uncertainty of 2% is applied to all processes.

447 **Pileup (shape and rate)** The uncertainty in the distribution of the number of pileup interactions  
 448 is applied by varying the cross section used to predict the number of pileup interactions  
 449 in MC by  $\pm 5\%$  from its nominal value of 69 mb [35].

450 **Jet Energy Resolution (shape and rate)** The uncertainty covering the jet energy resolution is  
 451 evaluated by increasing and decreasing the difference between reconstructed jet energy  
 452 and true jet energy on particle level. The scale factors and their uncertainties used in  
 453 the smearing are provided in reference [25]. The complete analysis chain is repeated for  
 454 samples with systematically changed jet energy resolution.

455 **Jet Energy Scale (shape and rate)** The applied jet energy corrections are varied within their  
 456 provided uncertainties [24] and the complete analysis is repeated for the systematically  
 457 shifted samples.

458 **CSV Reweighting (shape and rate)** The CSV reweighting procedure described in Section 4.3  
 459 considers different uncertainty sources, which are all treated as uncorrelated uncertainties.  
 460 When changing the jet energy scale according to its uncertainties the change of the  
 461 b-tagging scale factors is re-evaluated and taken as 100% correlated to the shift of the  
 462 energy scale. Another uncertainty source is the impurity of the sample from which the  
 463 scale factors were derived. The third source, the impact of statistical uncertainties during  
 464 the scale factor determination, is propagated to an alternative set of scale factors. The  
 465 statistical impact is described by two different nuisance parameters, which both have  
 466 control over distortions in the CSV distribution. All of the uncertainties described above  
 467 are taken into account separately for heavy flavor and light flavor jets and are taken to be  
 468 fully uncorrelated. Additionally, two sets of weights are applied that change the contam-  
 469 ination of charm jets in the samples used for the scale factor determination. More infor-  
 470 mation on the uncertainties considered in the scale factor determination can be found in  
 471 Reference [34].

### 472 Theoretical uncertainties

473  **$t\bar{t} + \text{Heavy Flavor Rates (rate)}$**  A 50% rate uncertainty is assigned to the  $t\bar{t} + b$ ,  $t\bar{t} + 2b$ ,  $t\bar{t} + b\bar{b}$   
 474 and  $t\bar{t} + c\bar{c}$  samples.

475  **$Q^2$  scale (shape and rate)** By utilizing the LHE reweighting procedure, events in a simulation  
 476 sample can be reweighted in such a way that they emulate a sample produced with a  
 477 varied  $Q^2$  scale at matrix element level. These weights are available for all simulation  
 478 samples but the single top and diboson samples, and for each process an uncorrelated  $Q^2$   
 479 scale uncertainty is introduced by reweighting the events in the final classification output.  
 480 The reweighted samples correspond to a  $Q$  scale of double and half of the initial value.  
 481 The implementation of this uncertainty has a large effect on the shape of the classification  
 482 output as well as on the normalization of the individual processes. For  $t\bar{t}$  the  $Q^2$  scale  
 483 uncertainty is evaluated using dedicated samples that have been produced with different

Table 11: Cross section uncertainties based on the choice of PDF set and  $Q^2$  scale applied for the different processes. The uncertainty values are obtained from References [14–16, 36, 37].

Process	PDF [%]			$Q^2$ scale [%]
	gg	q $\bar{q}$	qg	
tHq				3.7
tHW				4.0
t $\bar{t}$ H	3.6			
t $\bar{t}$	3.0			
t $\bar{t}$ W		2.0		
Single top			4.0	4.0
W + jets		4.0		
Diboson	2.0			2.5

values of the  $Q^2$  scale in the parton shower (again double and half the initial  $Q$  value), thus varying simultaneously both, the  $Q^2$  scale at matrix element and parton shower level.

**PDFs/ $Q^2$  Scale (rate)** Uncertainties applied to different simulation samples affecting the normalization of the different processes based on the choice of PDF set and the  $Q^2$  scale can be found in Table 11. Uncertainties for processes with a common production mechanism are treated as fully correlated.

As noted above the LHE weights needed for the  $Q^2$  uncertainty are not available for the single top and diboson simulation samples. Therefore, in analogy to the PDF rate uncertainties, the single top process is assigned a 4.0% rate uncertainty and the diboson process is assigned a 2.5% uncertainty to cover the effect of the variation of the  $Q^2$  scale.

## Statistical uncertainties

**Bin-by-bin uncertainties (shape)** Due to the finite size of the used simulated samples an additional uncertainty has to be considered. This uncertainty is evaluated applying the “Barlow-Beeston lite” method [38, 39], which introduces a nuisance parameter in the fit for each bin in each sample and each region. For every introduced nuisance parameter one bin is varied within its uncertainties while the other bins are scaled such that the normalization of the complete distribution remains constant. This procedure introduces hundreds of additional nuisance parameters, resulting in a significant increase of the needed computing power. In order to keep the calculation complexity within reasonable bounds only bins with a relative uncertainty above 5% are considered for the evaluation of this uncertainty.

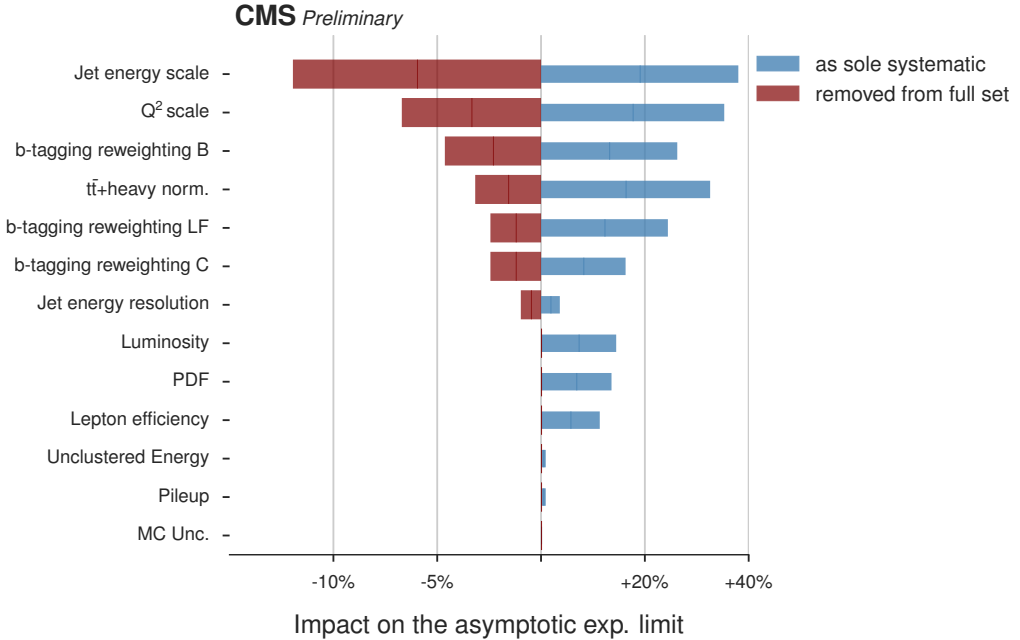


Figure 28: Impact of groups of systematic uncertainties on the expected asymptotic limit. The groups of systematic uncertainties are either removed from the fit by fixing them to their postfit value, or used as single systematic uncertainty by fixing all other uncertainties to their postfit values. The changes displayed in this diagram are calculated relative to the limit with all systematic uncertainties included (red bars) and to the limit where all uncertainties are fixed to their best fit value (blue bars).

## 506 9 Limit Extraction

507 The final limit for all 51 considered coupling hypotheses is extracted with a simultaneous Maximum  
 508 Likelihood Estimate fit of the classification BDT output in the 3 tag and 4 tag regions for  
 509 each coupling point. The prefit distributions for the coupling case of  $\kappa_t = -1$  and  $\kappa_V = +1$  and  
 510 for the SM prediction of  $\kappa_t = +1$  and  $\kappa_V = +1$  can be found in Figure 29. In order to account for  
 511 the observed normalization offset, expected limits are derived from a postfit asimov dataset,  
 512 although the analysis is still blinded.

513 The underlying model of the analysis is tested by comparing nuisance parameters of a prefit  
 514 asimov dataset with a postfit asimov dataset. The comparison can be found in Figure 78 and  
 515 Figure 79. The comparison shows a stringent constraint of an uncertainty associated with the c  
 516 quark purity during the estimation of the CSV reweighting parameters. This uncertainty seems  
 517 to be overestimated, as the same behavior already is apparent in other analyses [11].

518 Furthermore, the impact of uncertainty groups is studied by freezing specific groups to their  
 519 postfit values and thus effectively removing them from the limit calculation. The impact is de-  
 520 termined in two ways: On the one hand the impact of an uncertainty group as only uncertainty  
 521 source is derived by freezing all other uncertainty groups to their postfit values. The effect  
 522 is quantified by taking the relative limit increase on a limit where all uncertainties are frozen.  
 523 On the other hand, the impact from a removal of an uncertainty group is determined by tak-  
 524 ing the relative decrease of a limit with a certain frozen uncertainty group to the limit with all  
 525 uncertainties included. The outcome of this study can be seen in Figure 28. The study shows  
 526 that the analysis would benefit the most from a reduction of the  $Q^2$  scale uncertainty or of the  
 527 uncertainties related to the CSV reweighting.

528 Asymptotic CLs limits at 95% C.L. are calculated for each of the 51 points; they can be found in  
 529 Figure 30. A cubic spline fit has been used to interpolate between the calculated values in order  
 530 to smoothen the shape of the limit curves. The values for the case of  $\kappa_t = -1$  and  $\kappa_V = +1$  and  
 531 the SM prediction for tH production can be found in Table 12. The expected limit values for all  
 532 studied points can be found in the Appendix in Table 15.

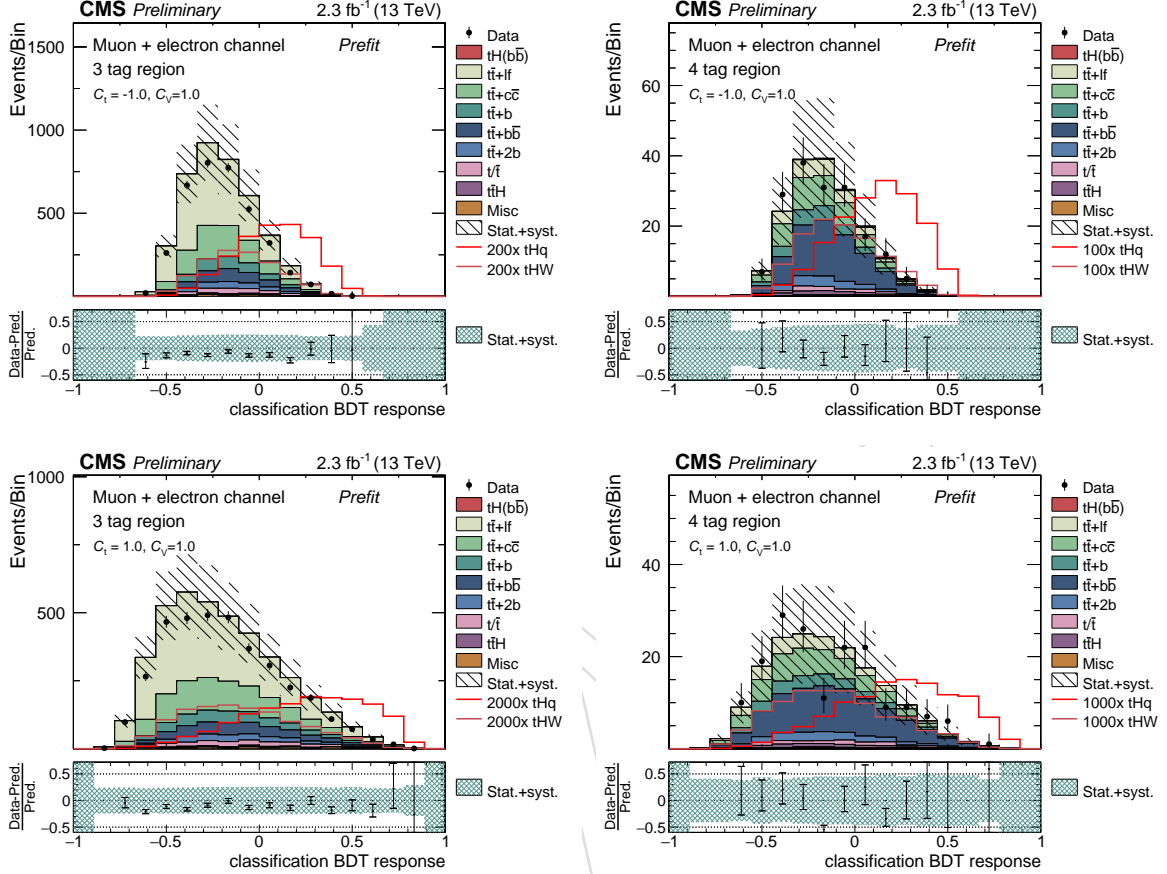


Figure 29: Prefit distributions of the classifier output in the 3 tag and 4 tag regions for the coupling pair of  $\kappa_t = -1$  and  $\kappa_V = +1$  and for the SM prediction. Neglecting the normalization offset, the shapes of data and simulation agree well. The uncertainty bands contain both systematic and statistical contributions. All MC corrections are applied.

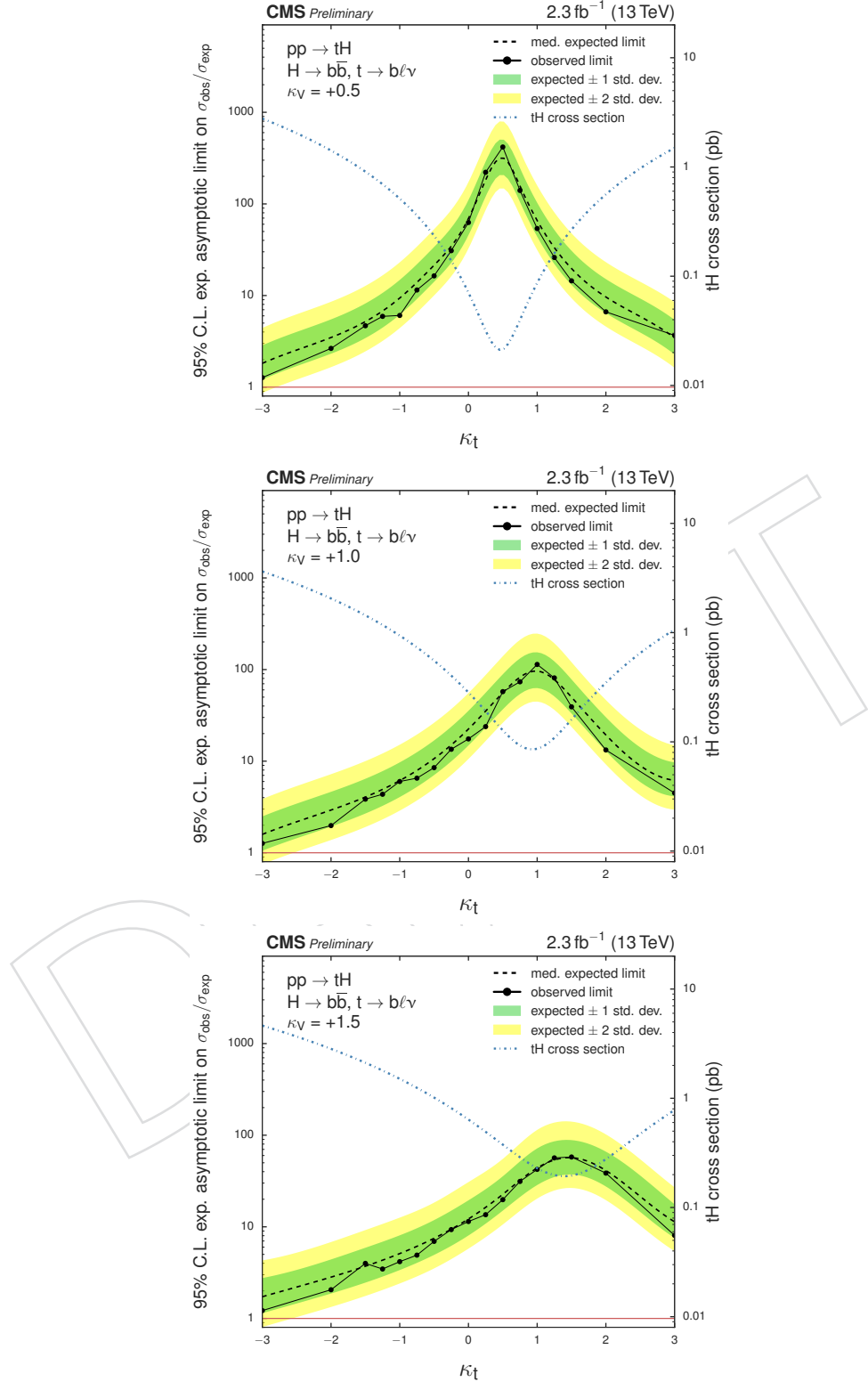


Figure 30: Upper limits on  $t\bar{t}H$  scenarios with different  $\kappa_t$ - $\kappa_V$  configurations, for  $\kappa_V = 0.5$  (top),  $\kappa_V = 1$  (middle), and  $\kappa_V = 1.5$  (bottom). Neither an excess nor a strong downward fluctuation is observed.

Table 12: Expected and observed asymptotic  $CL_s$  limits at 95% C.L. in the 3-tag and 4-tag region and their combination for the SM and ITC coupling scenarios. Also the 68% and 95% uncertainty band values are shown.

	Region	Observed Limit	Expected Limit		
			Median	$\pm 1\sigma$	$\pm 2\sigma$
$\kappa_t = 1$ (SM)	3 tag	124.0	114.3	[73.6, 184.4]	[52.0, 295.2]
	4 tag	195.8	174.6	[112.9, 287.4]	[78.8, 464.4]
	<b>Combination</b>	<b>113.7</b>	<b>98.6</b>	<b>[64.0, 159.2]</b>	<b>[45.3, 254.8]</b>
$\kappa_t = -1$ (ITC)	3 tag	7.4	7.4	[4.9, 11.6]	[3.5, 17.8]
	4 tag	9.2	10.0	[6.5, 16.3]	[4.5, 26.3]
	<b>Combination</b>	<b>6.0</b>	<b>6.4</b>	<b>[4.2, 10.1]</b>	<b>[3.0, 15.7]</b>

## 533 10 Summary

534 We have conducted a search for  $t$ - and  $tW$ -channel single top production in association with the  
535 125 GeV Higgs boson using the full CMS dataset at a center of mass energy of 13 TeV, updating  
536 a previous analysis performed at 8 TeV. Due to the low cross section of this process in the  
537 standard model, the focus of the analysis is on possible variations in the coupling between the  
538 Higgs boson and the top quark or the W boson; such variations could arise as part of physics  
539 beyond the standard model. Limits are calculated as a function of the coupling strength factors  
540  $\kappa_t$  and  $\kappa_V$ .

541 Two different signal regions are selected: one region with at least 4 jets, among them exactly  
542 3 tagged jets; the other region with at least 5 jets, exactly 4 of which must be tagged. The  
543 assignment of the jets to a potential  $tHq$  signal or  $t\bar{t}$  background reconstruction hypothesis  
544 is performed using two separate boosted decision trees. A third boosted decision tree uses  
545 these assignments to enhance the signal-to-background ratio and discriminate against main  
546 backgrounds, including the predominant  $t\bar{t}$  production. Limits are then calculated using the  
547 shape of the BDT distribution.

548 The observed 95% confidence-level upper limit for the scenario with  $\kappa_V = +1$  and  $\kappa_t = -1$  is  
549 6.0 times the predicted cross section, with an expected upper limit of 6.4.

DRAFT

<sup>550</sup> **A Appendix A: Signal cross sections**

Table 13: Production cross sections for  $tHq$ , depending on  $\kappa_f$  and  $\kappa_V$ . Obtained with MADGRAPH5\_AMC@NLO at NLO in the 4F. The quoted uncertainties on the cross section correspond to scale variations in %. Additional information can be found in Ref. [40].

$\kappa_t$	$\kappa_V$	$\sigma [\text{pb}]$	$\kappa_t$	$\kappa_V$	$\sigma [\text{pb}]$	$\kappa_t$	$\kappa_V$	$\sigma [\text{pb}]$
-3.0	0.5	$2.260^{+1.9}_{-2.7}$	-3.0	1.0	$2.991^{+2.1}_{-3.1}$	-3.0	1.5	$3.845^{+2.6}_{-3.2}$
-2.0	0.5	$1.160^{+2.0}_{-2.9}$	-2.0	1.0	$1.706^{+2.6}_{-3.2}$	-2.0	1.5	$2.371^{+2.5}_{-3.6}$
-1.5	0.5	$0.748^{+2.1}_{-3.1}$	-1.5	1.0	$1.205^{+2.5}_{-3.6}$	-1.5	1.5	$1.784^{+2.7}_{-3.9}$
-1.25	0.5	$0.573^{+2.1}_{-3.0}$	-1.25	1.0	$0.987^{+2.6}_{-3.4}$	-1.25	1.5	$1.518^{+2.8}_{-3.9}$
-1.0	0.5	$0.472^{+2.3}_{-3.3}$	-1.0	1.0	$0.793^{+2.7}_{-3.9}$	-1.0	1.5	$1.287^{+3.0}_{-4.3}$
-0.75	0.5	$0.300^{+2.5}_{-3.5}$	-0.75	1.0	$0.621^{+2.9}_{-4.1}$	-0.75	1.5	$1.067^{+3.1}_{-4.4}$
-0.5	0.5	$0.198^{+2.8}_{-3.9}$	-0.5	1.0	$0.472^{+3.2}_{-4.4}$	-0.5	1.5	$0.874^{+3.4}_{-4.7}$
-0.25	0.5	$0.119^{+3.1}_{-4.6}$	-0.25	1.0	$0.351^{+3.5}_{-5.0}$	-0.25	1.5	$0.703^{+3.6}_{-5.0}$
0.0	0.5	$0.062^{+3.8}_{-5.6}$	0.0	1.0	$0.248^{+3.9}_{-5.5}$	0.0	1.5	$0.558^{+3.8}_{-5.4}$
0.25	0.5	$0.028^{+5.0}_{-7.1}$	0.25	1.0	$0.169^{+4.4}_{-6.2}$	0.25	1.5	$0.437^{+4.2}_{-6.1}$
0.5	0.5	$0.018^{+4.2}_{-6.7}$	0.5	1.0	$0.113^{+5.0}_{-7.1}$	0.5	1.5	$0.334^{+4.6}_{-6.5}$
0.75	0.5	$0.030^{+1.4}_{-2.9}$	0.75	1.0	$0.081^{+5.7}_{-7.6}$	0.75	1.5	$0.256^{+5.2}_{-7.2}$
1.0	0.5	$0.066^{+1.0}_{-3.6}$	1.0	1.0	$0.071^{+4.1}_{-6.7}$	1.0	1.5	$0.200^{+5.7}_{-7.6}$
1.25	0.5	$0.124^{+0.9}_{-3.7}$	1.25	1.0	$0.084^{+2.3}_{-4.6}$	1.25	1.5	$0.167^{+5.5}_{-7.5}$
1.5	0.5	$0.205^{+0.8}_{-3.7}$	1.5	1.0	$0.120^{+1.2}_{-2.9}$	1.5	1.5	$0.159^{+4.1}_{-6.7}$
2.0	0.5	$0.436^{+1.0}_{-3.6}$	2.0	1.0	$0.260^{+1.0}_{-3.6}$	2.0	1.5	$0.211^{+2.0}_{-3.9}$
3.0	0.5	$1.177^{+1.2}_{-3.2}$	3.0	1.0	$0.821^{+0.8}_{-3.7}$	3.0	1.5	$0.589^{+0.9}_{-3.7}$

Table 14: Production cross sections for tHW, depending on  $\kappa_f$  and  $\kappa_V$ . Obtained with MADGRAPH5\_AMC@NLO at NLO in the 5F. The quoted uncertainties on the cross section correspond to scale variations in %. Additional information can be found in Ref. [40].

$\kappa_t$	$\kappa_V$	$\sigma [\text{pb}]$	$\kappa_t$	$\kappa_V$	$\sigma [\text{pb}]$	$\kappa_t$	$\kappa_V$	$\sigma [\text{pb}]$
-3.0	0.5	$0.514^{+2.3}_{-3.0}$	-3.0	1.0	$0.641^{+2.3}_{-2.7}$	-3.0	1.5	$0.783^{+2.1}_{-2.1}$
-2.0	0.5	$0.255^{+2.3}_{-2.8}$	-2.0	1.0	$0.346^{+2.2}_{-2.5}$	-2.0	1.5	$0.457^{+2.1}_{-2.1}$
-1.5	0.5	$0.159^{+2.3}_{-2.8}$	-1.5	1.0	$0.253^{+2.1}_{-2.2}$	-1.5	1.5	$0.329^{+1.9}_{-1.8}$
-1.25	0.5	$0.120^{+2.2}_{-2.5}$	-1.25	1.0	$0.188^{+2.0}_{-2.0}$	-1.25	1.5	$0.275^{+1.9}_{-1.6}$
-1.0	0.5	$0.087^{+2.1}_{-2.3}$	-1.0	1.0	$0.147^{+2.0}_{-1.8}$	-1.0	1.5	$0.224^{+1.9}_{-1.5}$
-0.75	0.5	$0.059^{+2.0}_{-2.1}$	-0.75	1.0	$0.110^{+2.0}_{-1.7}$	-0.75	1.5	$0.180^{+1.8}_{-1.3}$
-0.5	0.5	$0.037^{+1.9}_{-1.8}$	-0.5	1.0	$0.080^{+1.7}_{-1.4}$	-0.5	1.5	$0.141^{+1.6}_{-1.2}$
-0.25	0.5	$0.020^{+1.8}_{-1.3}$	-0.25	1.0	$0.055^{+1.6}_{-1.1}$	-0.25	1.5	$0.108^{+1.6}_{-1.2}$
0.0	0.5	$0.009^{+1.6}_{-1.3}$	0.0	1.0	$0.036^{+1.5}_{-1.2}$	0.0	1.5	$0.081^{+1.5}_{-1.2}$
0.25	0.5	$0.004^{+2.1}_{-2.0}$	0.25	1.0	$0.022^{+1.6}_{-1.5}$	0.25	1.5	$0.059^{+1.5}_{-1.4}$
0.5	0.5	$0.004^{+4.6}_{-6.1}$	0.5	1.0	$0.014^{+2.1}_{-2.0}$	0.5	1.5	$0.043^{+1.8}_{-1.7}$
0.75	0.5	$0.010^{+4.7}_{-6.3}$	0.75	1.0	$0.012^{+3.2}_{-3.9}$	0.75	1.5	$0.033^{+2.1}_{-2.0}$
1.0	0.5	$0.021^{+4.0}_{-5.5}$	1.0	1.0	$0.016^{+4.6}_{-6.1}$	1.0	1.5	$0.028^{+2.8}_{-3.0}$
1.25	0.5	$0.038^{+3.7}_{-5.2}$	1.25	1.0	$0.025^{+4.8}_{-5.4}$	1.25	1.5	$0.029^{+3.6}_{-4.7}$
1.5	0.5	$0.061^{+3.5}_{-4.9}$	1.5	1.0	$0.039^{+4.6}_{-6.3}$	1.5	1.5	$0.035^{+4.6}_{-6.0}$
2.0	0.5	$0.125^{+3.0}_{-4.3}$	2.0	1.0	$0.086^{+4.0}_{-5.5}$	2.0	1.5	$0.065^{+4.8}_{-6.5}$
3.0	0.5	$0.317^{+2.8}_{-4.0}$	3.0	1.0	$0.247^{+3.3}_{-4.6}$	3.0	1.5	$0.193^{+4.0}_{-5.6}$

---

551 **B Appendix B: Distributions of variables used in the reconstruc-**

552 **tion**

DRAFT

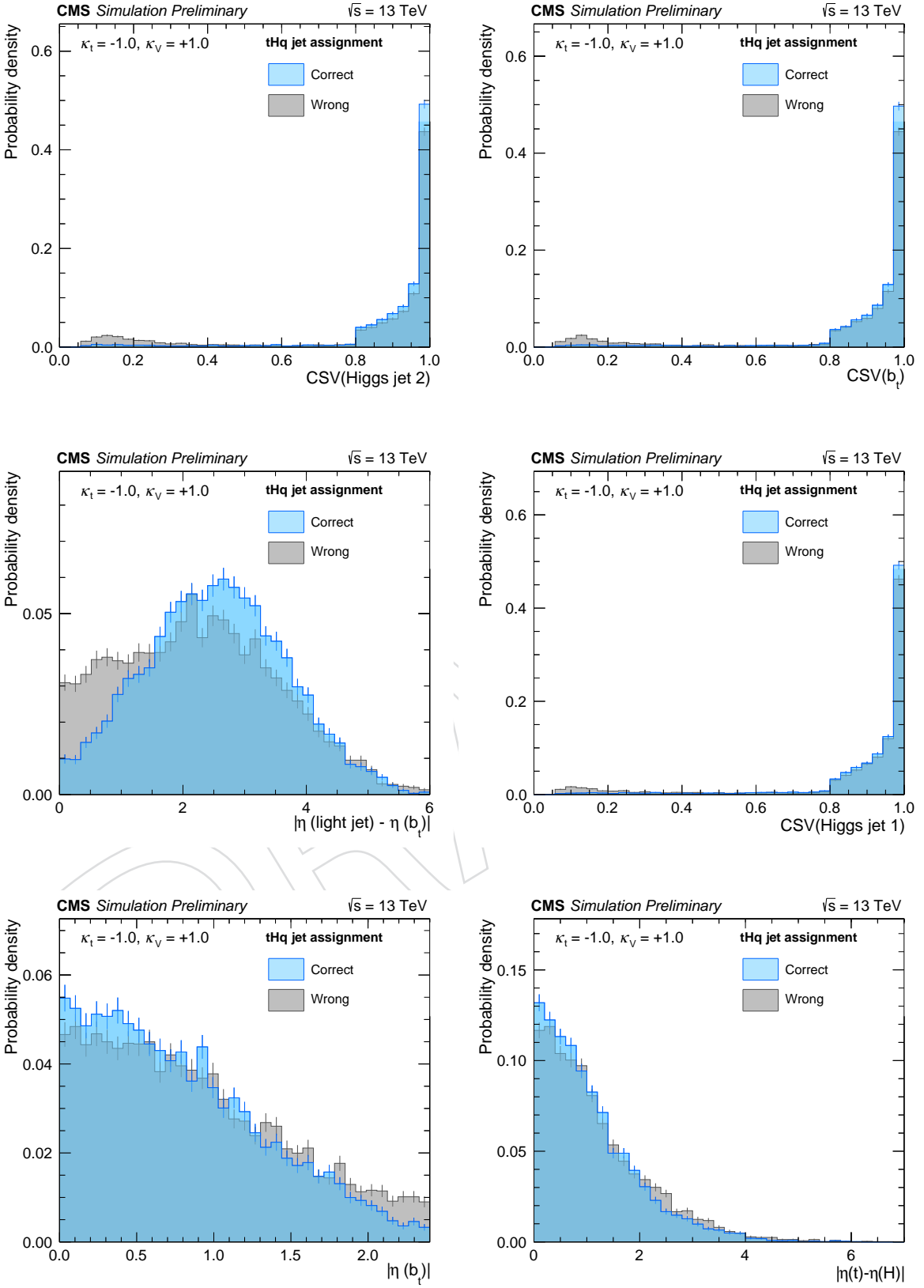


Figure 31: Distributions of variables ranked 7<sup>th</sup> to 12<sup>th</sup> place are shown for correct and wrong jet assignments in the tHq reconstruction. All distributions are normalized to unit area. The corresponding variable descriptions can be found in Table 7. The three remaining variables can be found in Appendix 32.

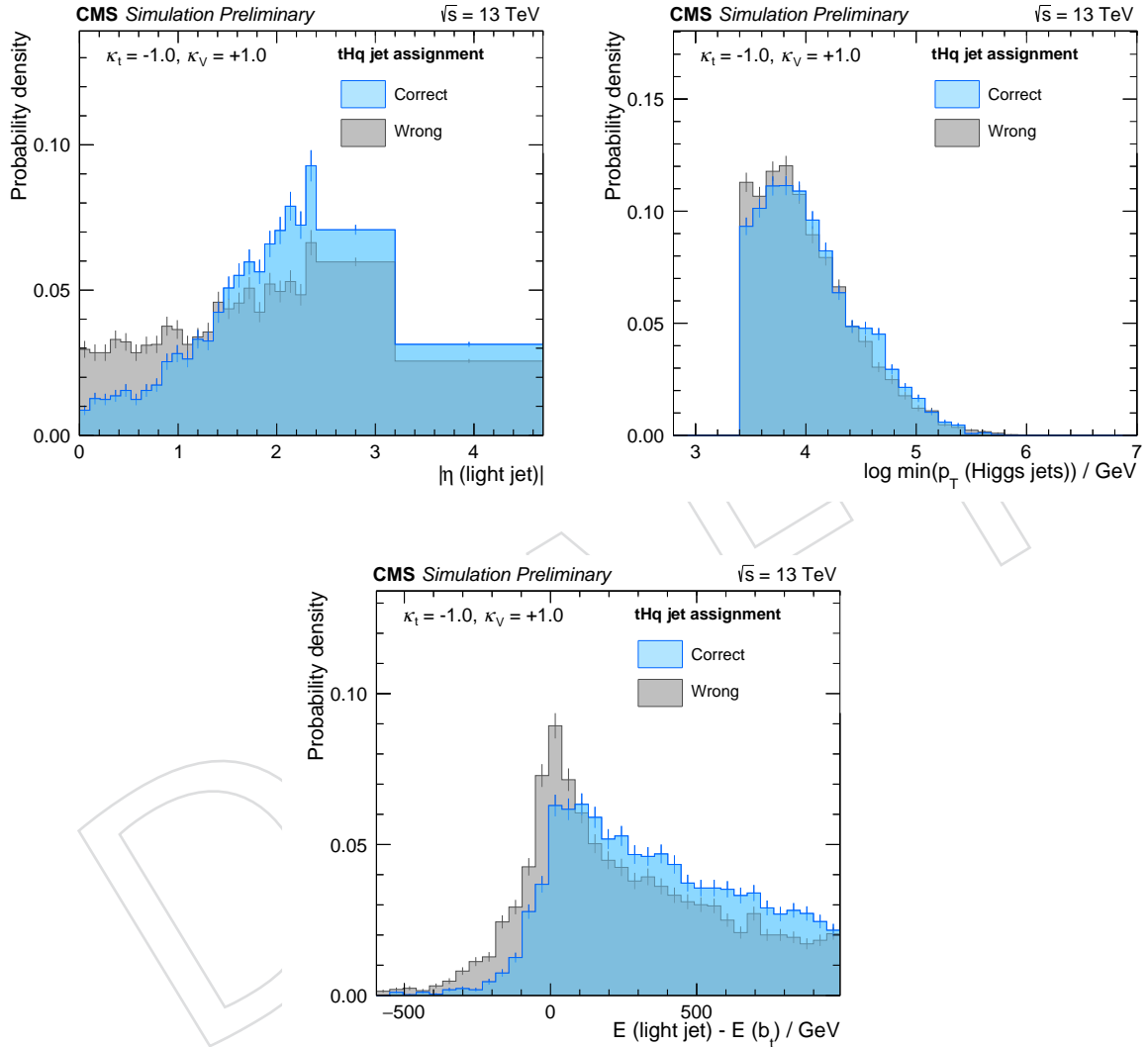


Figure 32: Distributions of variables ranked 13<sup>th</sup> to 15<sup>th</sup> place are shown for correct and wrong jet assignments in the tHq reconstruction. All distributions are normalized to unit area. The corresponding variable descriptions can be found in Table 7.

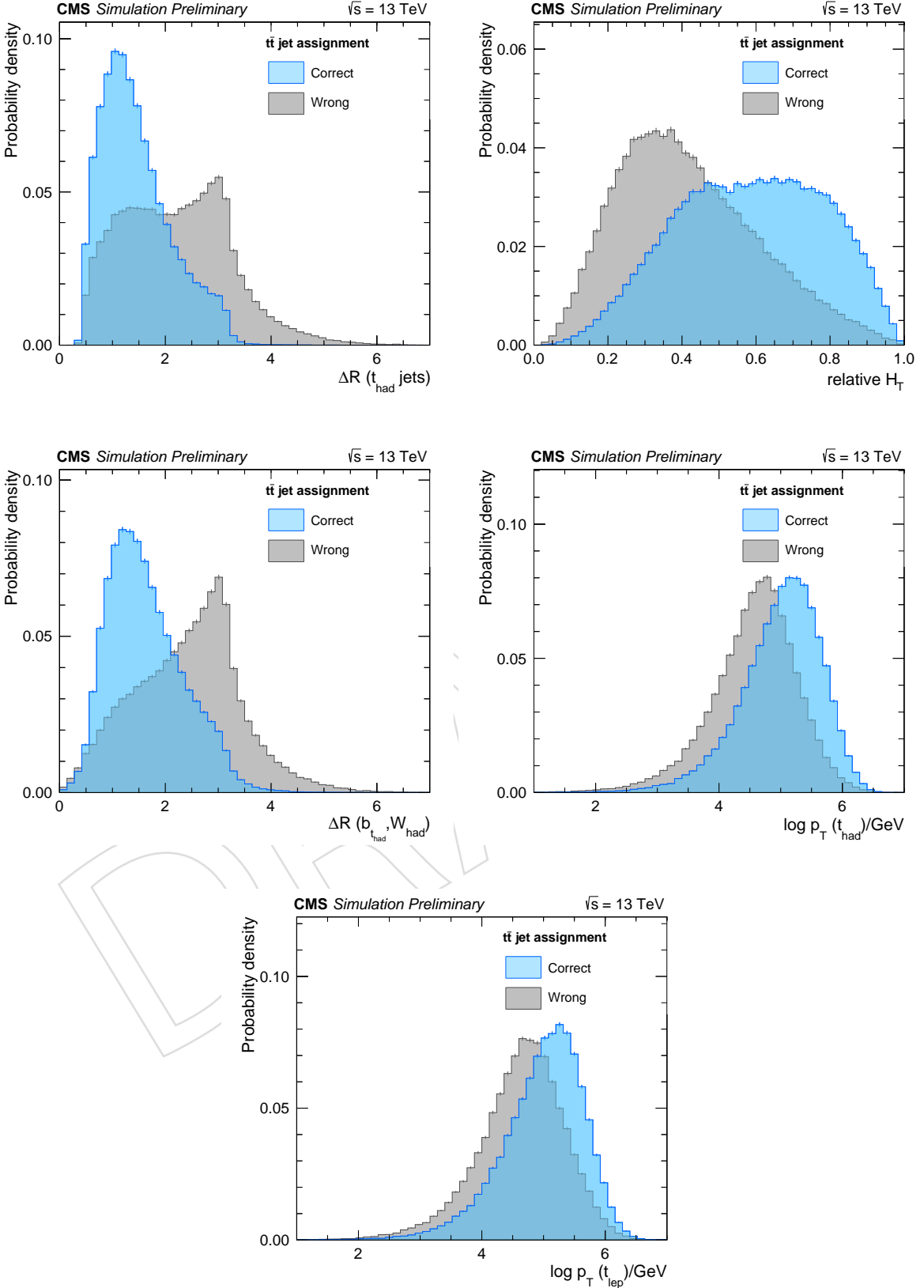


Figure 33: The remaining five variables between correct and wrong jet assignments in the  $t\bar{t}$  reconstruction are shown sorted by their importance in the training. All distributions are normalized to unit area. The corresponding variable descriptions can be found in Table 8.

## 553 C Appendix C: Changes from 8 to 13 TeV

554 In this appendix we discuss the changes to the analysis that took place with respect to the  
 555 search at 8 TeV.

- 556 • The major change on the phenomenological side has been the inclusion of an additional  
 557 signal process, tHW. This has already been discussed in Sec. 2. Here a brief  
 558 motivation is given as to why this process has not played a role in the 8 TeV analysis.  
 559 As can be seen from Fig. 34, applying the signal selection will decrease the tHQ/tHW  
 560 ratio relative to the inclusive cross sections of the two processes. This is mainly due  
 561 to the harder object kinematics in the tHW process, which causes the Higgs boson  
 562 and the top quark to be more central and their decay products (i.e. the b jets) to  
 563 pass the  $p_T$  threshold more often; in addition, there is no explicit requirement on the  
 564 existence of a forward jet, which would reject not only much of the tHW signal, but  
 565 also a good portion of the  $t$ -channel contribution. For these reasons, and for several  
 566 points in the 2-dim. plane, tHW contributes almost equally to the signal region as the  
 567 tHQ process. However, for the only point considered at 8 TeV,  $(\kappa_t, \kappa_V) = (-1, +1)$ ,  
 568 the ratio tHQ/tHW is  $> 2$ , which is why tHW has been neglected in the previous  
 569 searches. Now it is considered for all the points.

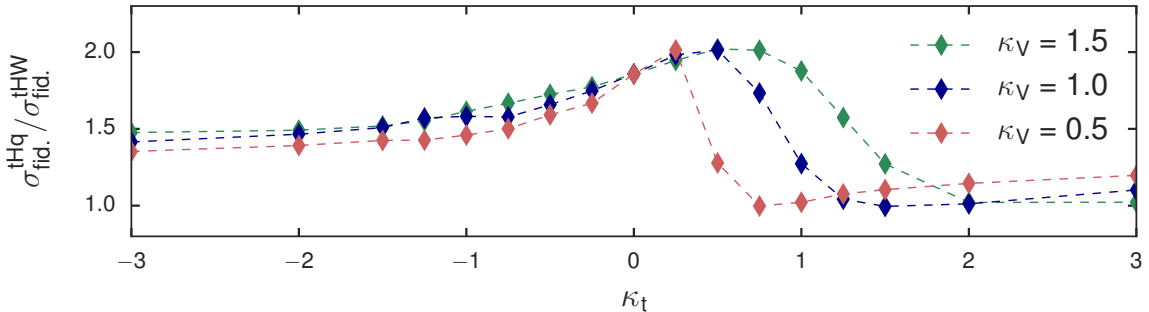


Figure 34: Relative contributions of the two signal processes tHQ and tHW in the signal regions for all 51 considered points in the 2-dim. plane. Since the kinematics changes differently with  $\kappa_t$  for tHQ and tHW, the ratio varies between  $\sim 1$  and  $\sim 2.5$ .

- 570 • Still on the phenomenological side, the signal modelling for the tHQ process has  
 571 undergone the changes listed in Table 1.
- 572 • The scope of the analysis has been extended: while at 8 TeV only the scenario with  
 573  $\kappa_t = -1$  has been searched for, now 51 points in the  $\kappa_t - \kappa_V$  plain are investigated.
- 574 • In terms of the event selection, a transition from the tight working point of the CSVv1  
 575 algorithm to the medium working point of the CSVv2 working point has taken place.  
 576 The CSV reweighting as applied in the ttH search is now used to correct for differ-  
 577 ences in b-/mistagging efficiencies between data and simulation. While in Run-I the  
 578 analysis has been bound to fixed working point and could only use boolean vari-  
 579 ables for the b-tagging status of a jet, the continuous CSV output of the jets can now  
 580 be employed as variable in the BDTs.

<sup>581</sup> **D Appendix D: Limit Values**

Table 15: List of all expected and observed asymptotic limits at 95% C.L. for all studied points in the  $\kappa_t - \kappa_V$  plane. The super- and subscripted values for the expected limit correspond to the  $\pm 1\sigma$  uncertainty band values for the studied points.

$\kappa_t$	$\kappa_V = 0.5$		$\kappa_V = 1.0$		$\kappa_V = 1.5$	
	obs.	exp.	obs.	exp.	obs.	exp.
-3.00	1.3	$1.8^{+1.0}_{-0.6}$	1.3	$1.6^{+0.9}_{-0.5}$	1.2	$1.7^{+1.0}_{-0.6}$
-2.00	2.6	$3.5^{+2.0}_{-1.2}$	2.0	$2.8^{+1.6}_{-0.9}$	2.1	$2.8^{+1.6}_{-0.9}$
-1.50	4.7	$5.2^{+3.0}_{-1.8}$	3.9	$4.1^{+2.4}_{-1.4}$	4.0	$3.6^{+2.1}_{-1.2}$
-1.25	5.9	$7.0^{+4.0}_{-2.4}$	4.4	$4.9^{+2.9}_{-1.7}$	3.5	$4.6^{+2.7}_{-1.6}$
-1.00	6.1	$9.0^{+5.2}_{-3.1}$	6.0	$6.4^{+3.7}_{-2.2}$	4.2	$5.1^{+3.0}_{-1.7}$
-0.75	11.5	$14.0^{+8.2}_{-4.9}$	6.5	$8.2^{+4.7}_{-2.7}$	4.9	$5.8^{+3.4}_{-2.0}$
-0.50	16.4	$21.3^{+12.3}_{-7.1}$	8.5	$10.5^{+6.1}_{-3.5}$	6.9	$7.7^{+4.5}_{-2.6}$
-0.25	30.9	$35.4^{+20.7}_{-12.2}$	13.5	$15.0^{+8.7}_{-5.0}$	9.3	$9.4^{+5.6}_{-3.2}$
0.00	62.7	$68.0^{+40.6}_{-23.2}$	17.5	$21.5^{+12.6}_{-7.3}$	11.4	$12.3^{+7.2}_{-4.2}$
0.25	221.4	$180.6^{+105.8}_{-61.6}$	23.8	$34.4^{+19.9}_{-11.6}$	13.6	$16.7^{+9.7}_{-5.7}$
0.50	417.9	$326.2^{+195.1}_{-112.1}$	57.4	$55.9^{+33.4}_{-19.1}$	19.8	$21.8^{+12.8}_{-7.4}$
0.75	140.2	$154.2^{+87.3}_{-51.2}$	73.5	$85.6^{+51.2}_{-29.4}$	31.3	$32.1^{+18.8}_{-11.0}$
1.00	53.9	$65.2^{+37.2}_{-21.8}$	113.7	$98.6^{+60.5}_{-34.6}$	42.4	$44.9^{+27.5}_{-15.5}$
1.25	26.0	$34.1^{+19.2}_{-11.6}$	81.1	$77.2^{+44.0}_{-26.3}$	56.5	$53.2^{+32.7}_{-18.6}$
1.50	14.5	$19.4^{+10.9}_{-6.5}$	39.2	$48.4^{+27.6}_{-16.3}$	57.8	$56.9^{+33.3}_{-19.3}$
2.00	6.6	$9.7^{+5.5}_{-3.2}$	13.3	$19.6^{+11.0}_{-6.5}$	38.6	$41.1^{+24.1}_{-13.8}$
3.00	3.7	$3.5^{+2.0}_{-1.2}$	4.5	$6.2^{+3.5}_{-2.0}$	8.1	$11.3^{+6.3}_{-3.8}$

582 **E Appendix E: BDT output distributions**

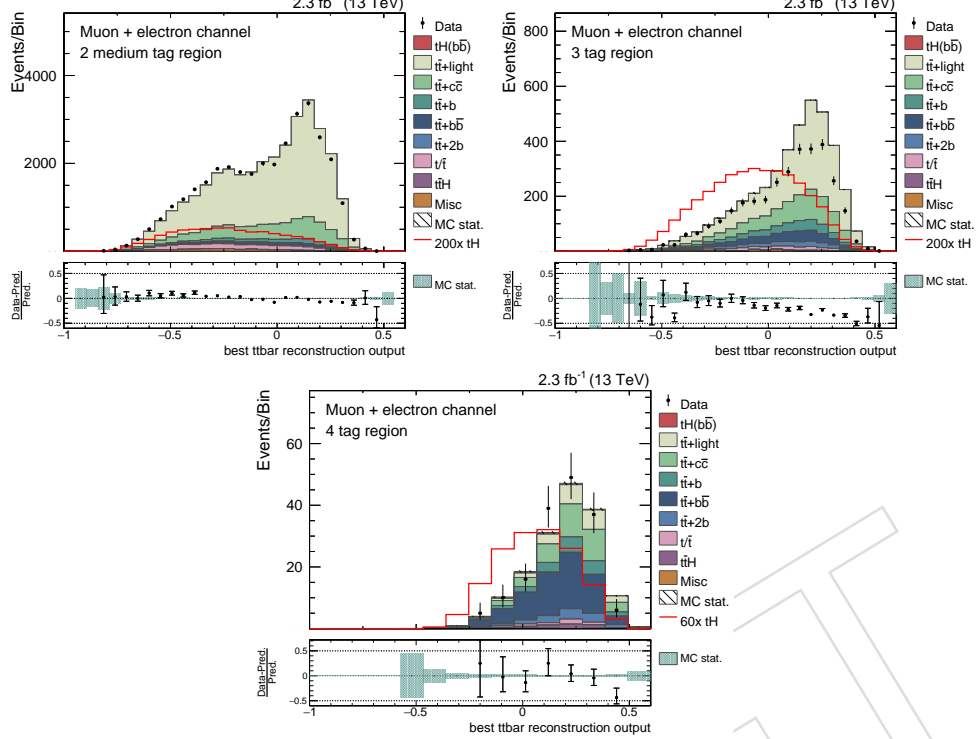


Figure 35: The output of  $t\bar{t}$  reconstruction BDT at 13 TeV in the three regions is shown in this figure.

## E Appendix E: BDT output distributions

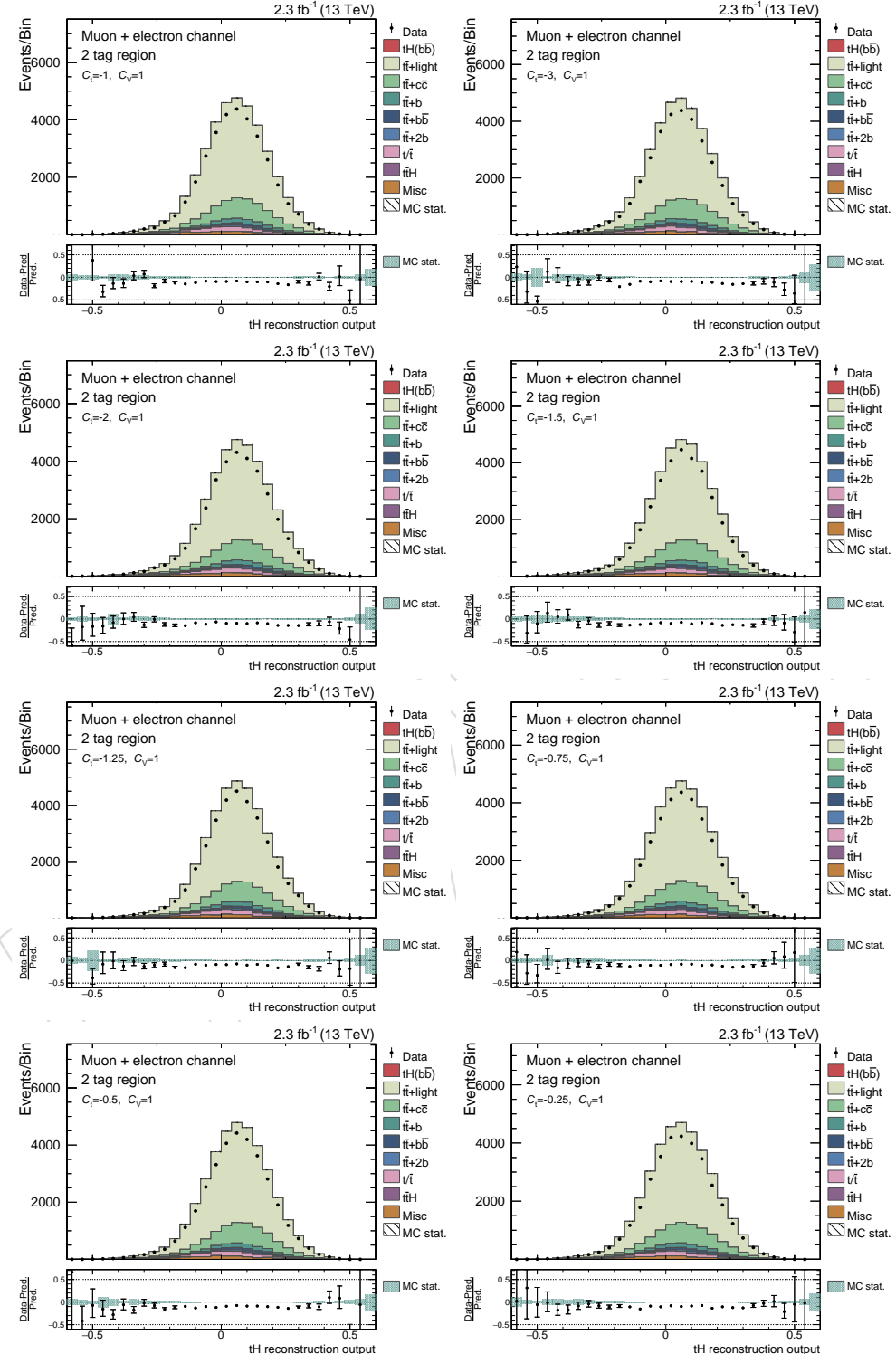


Figure 36: The output of tHq reconstruction BDT at 13 TeV in the 2 tag region for the different signal hypotheses is shown in this figure.

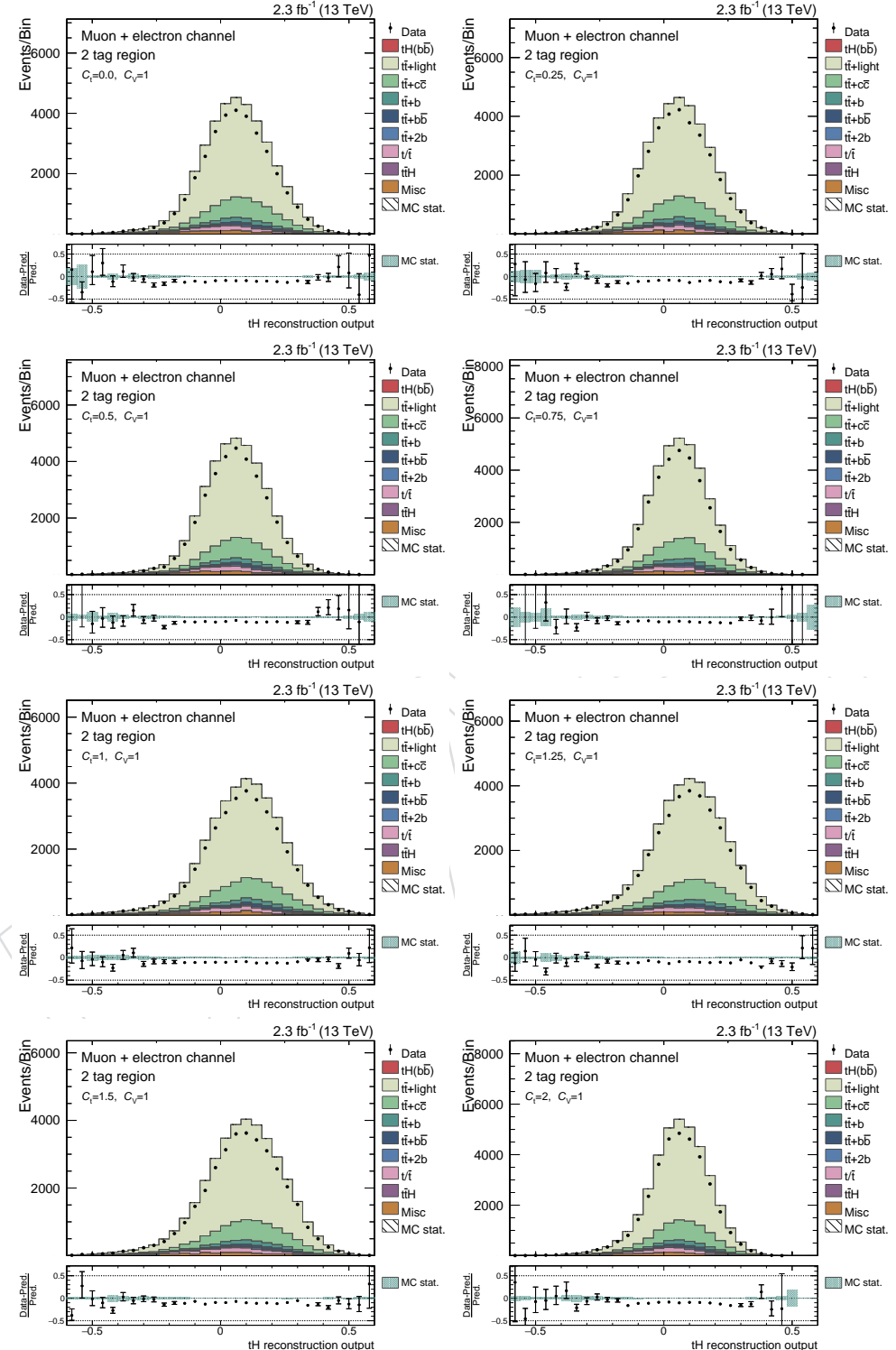


Figure 37: The output of  $tHq$  reconstruction BDT at 13 TeV in the 2 tag region for the different signal hypotheses is shown in this figure.

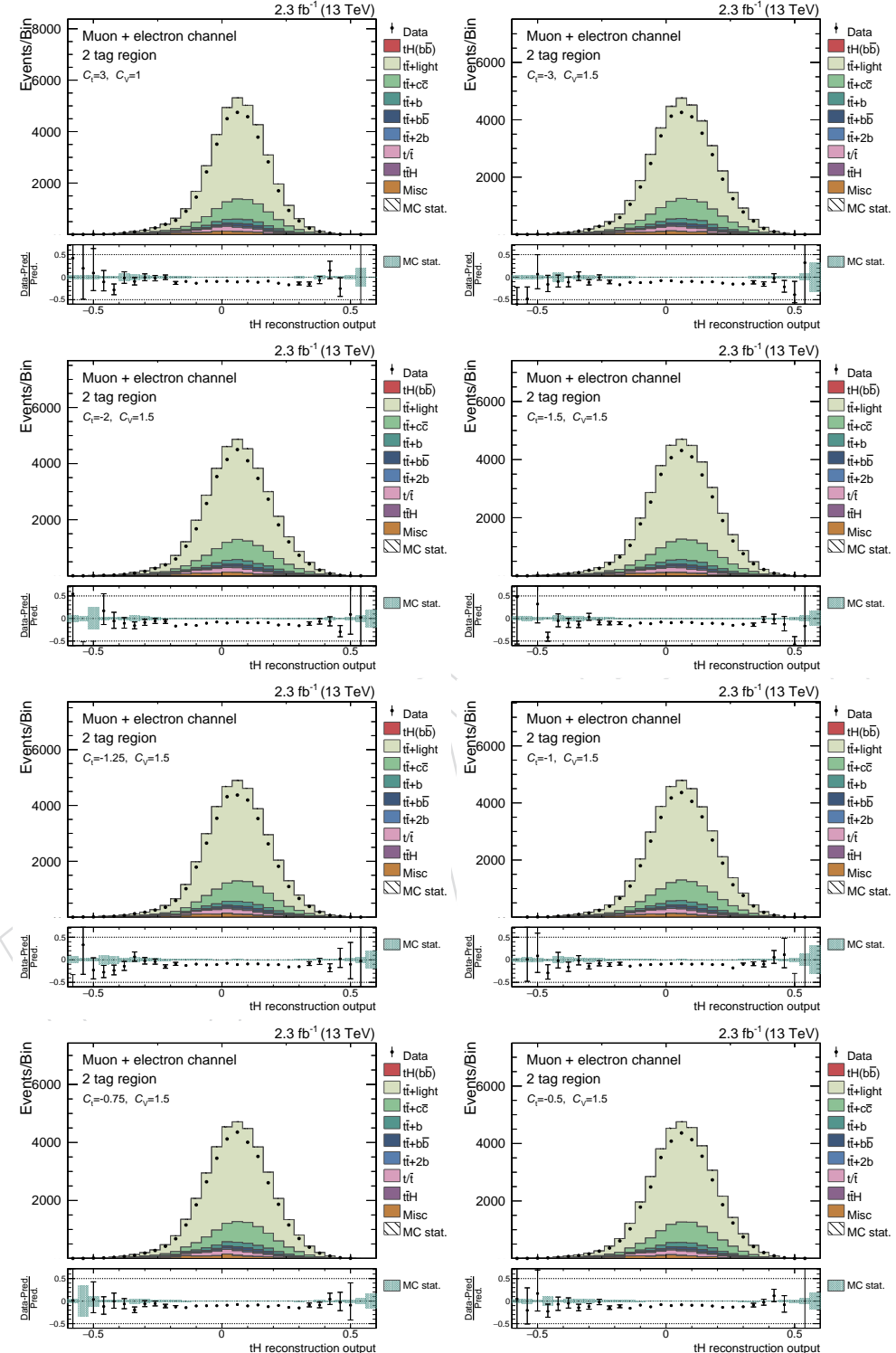


Figure 38: The output of  $tHq$  reconstruction BDT at 13 TeV in the 2 tag region for the different signal hypotheses is shown in this figure.

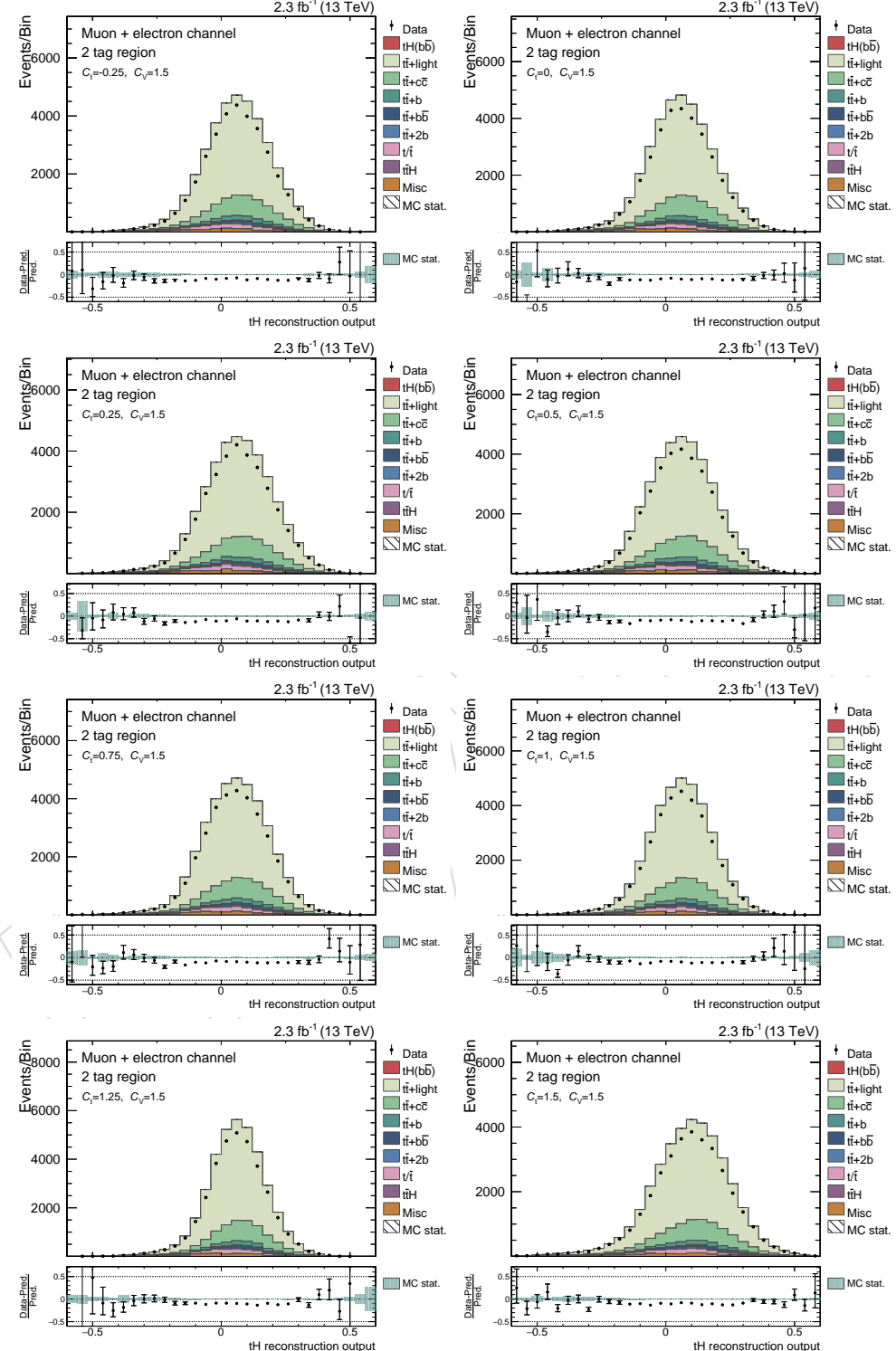


Figure 39: The output of  $tHq$  reconstruction BDT at 13 TeV in the 2 tag region for the different signal hypotheses is shown in this figure.

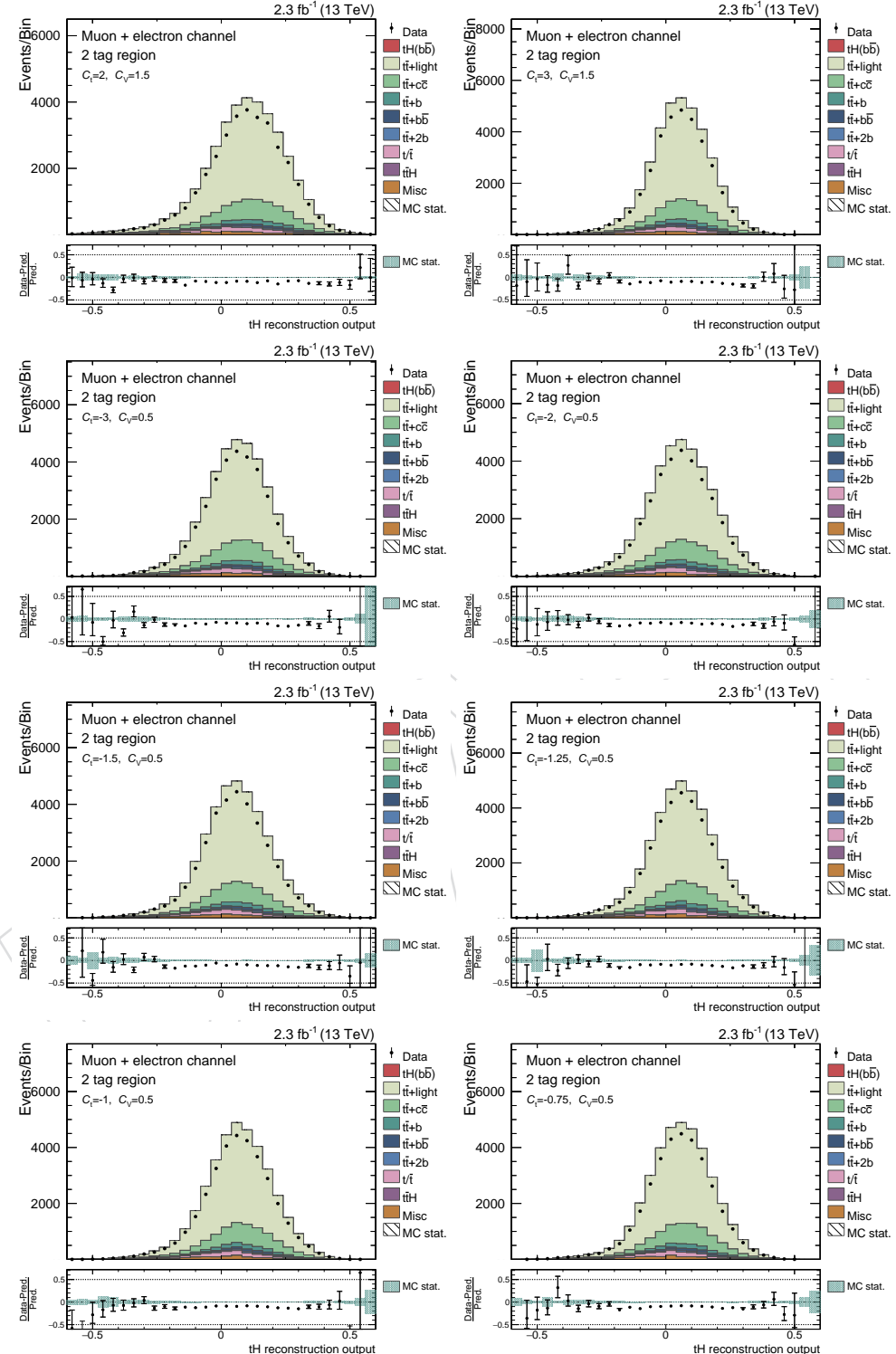


Figure 40: The output of  $tHq$  reconstruction BDT at 13 TeV in the 2 tag region for the different signal hypotheses is shown in this figure.

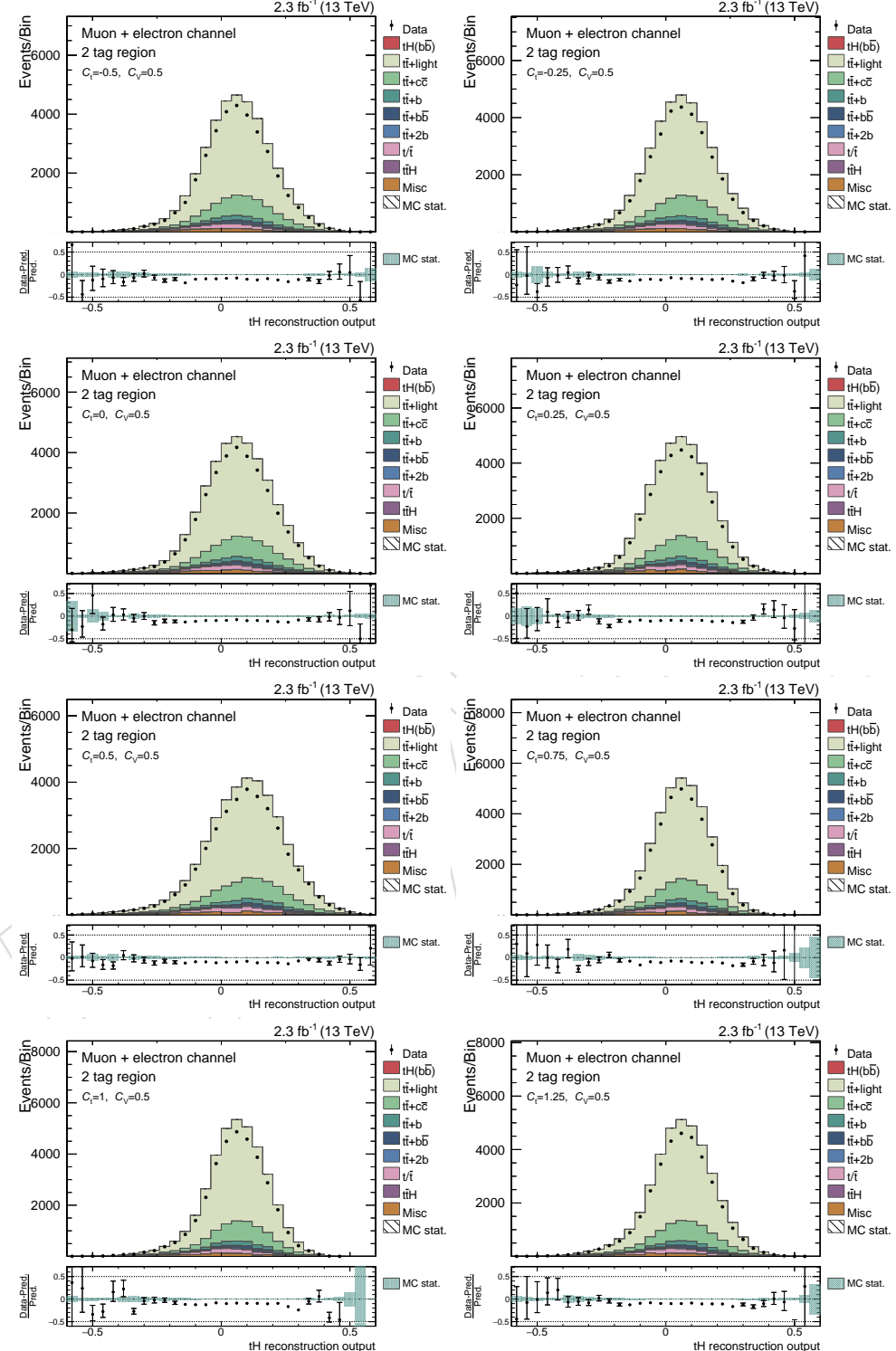


Figure 41: The output of  $tHq$  reconstruction BDT at 13 TeV in the 2 tag region for the different signal hypotheses is shown in this figure.

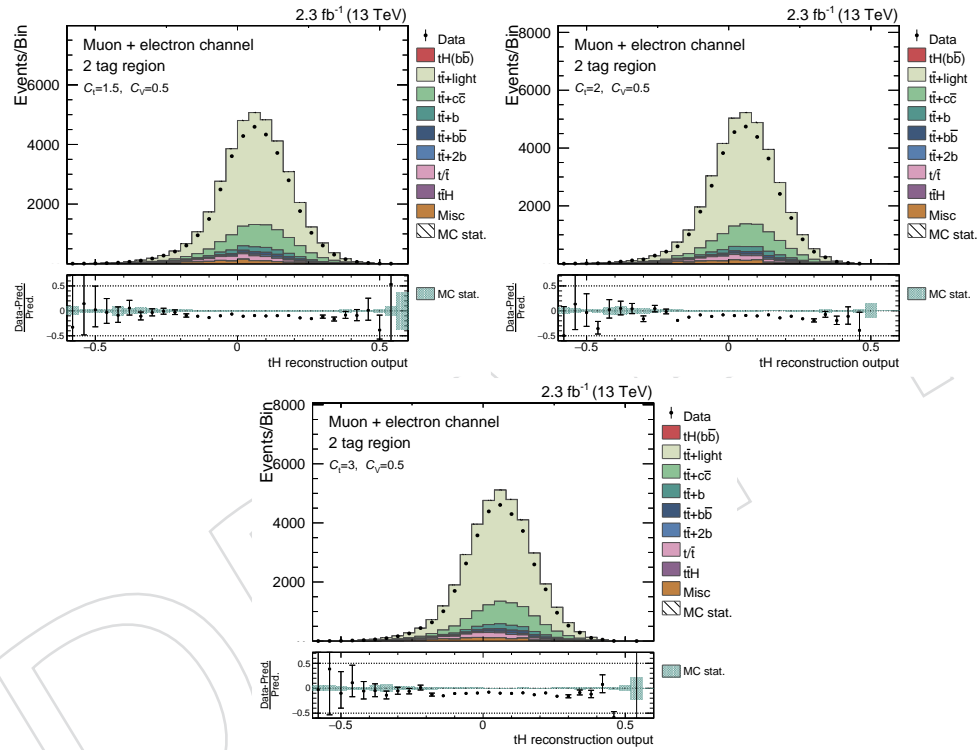


Figure 42: The output of  $tHq$  reconstruction BDT at  $13 \text{ TeV}$  in the 2 tag region for the different signal hypotheses is shown in this figure.

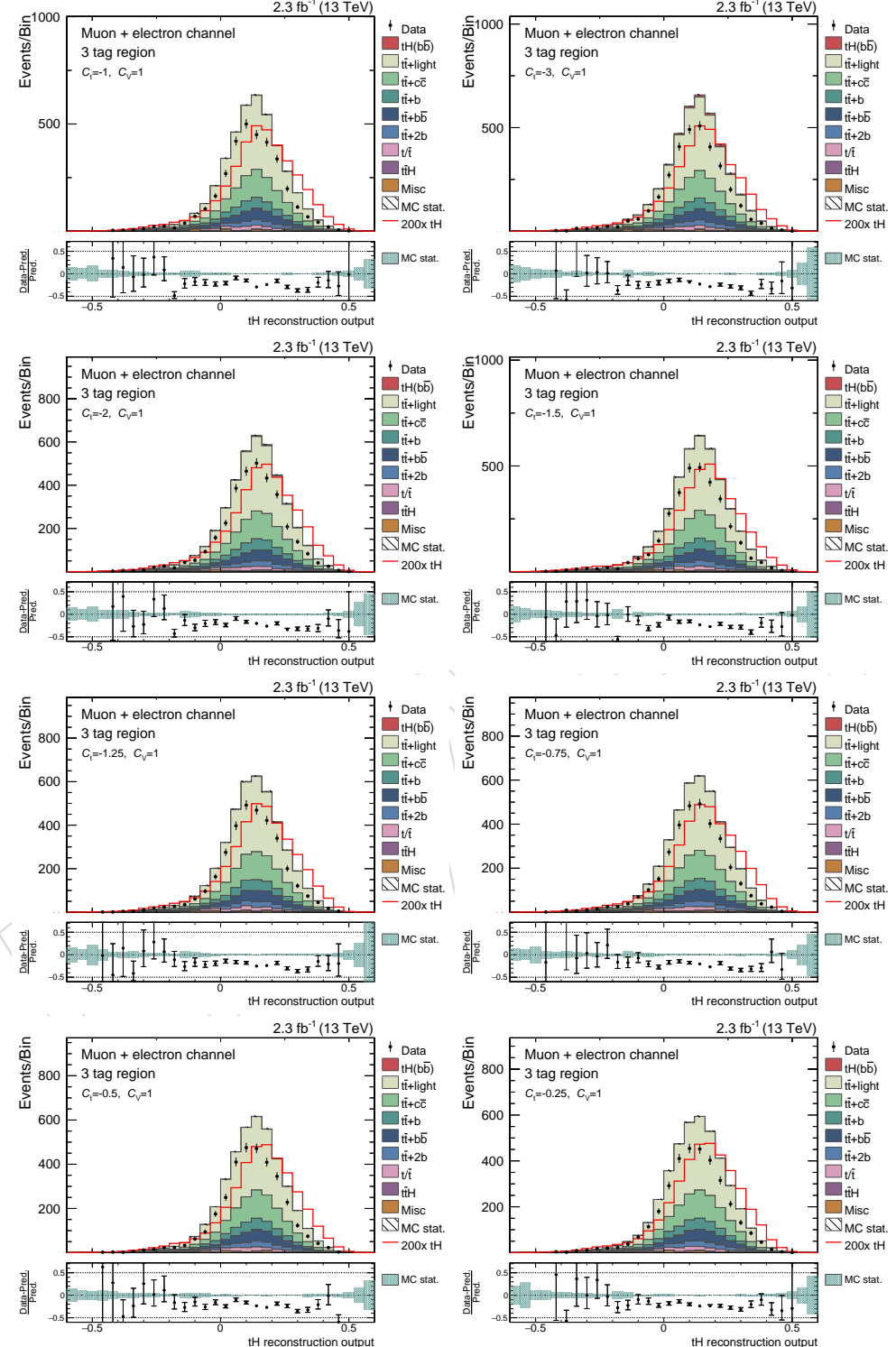


Figure 43: The output of tHq reconstruction BDT at 13 TeV in the 3 tag region for the different signal hypotheses is shown in this figure.

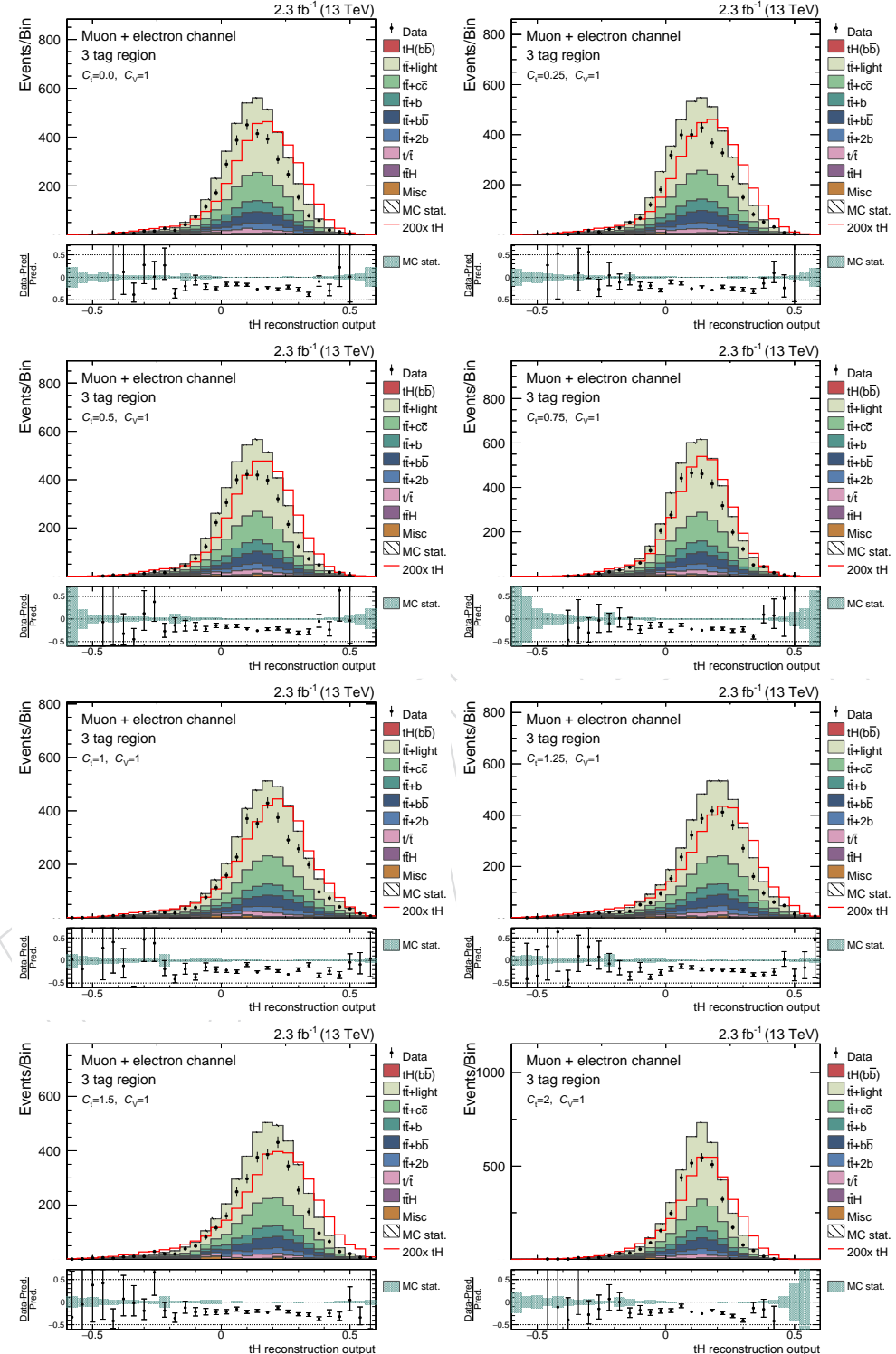


Figure 44: The output of  $tHq$  reconstruction BDT at 13 TeV in the 3 tag region for the different signal hypotheses is shown in this figure.

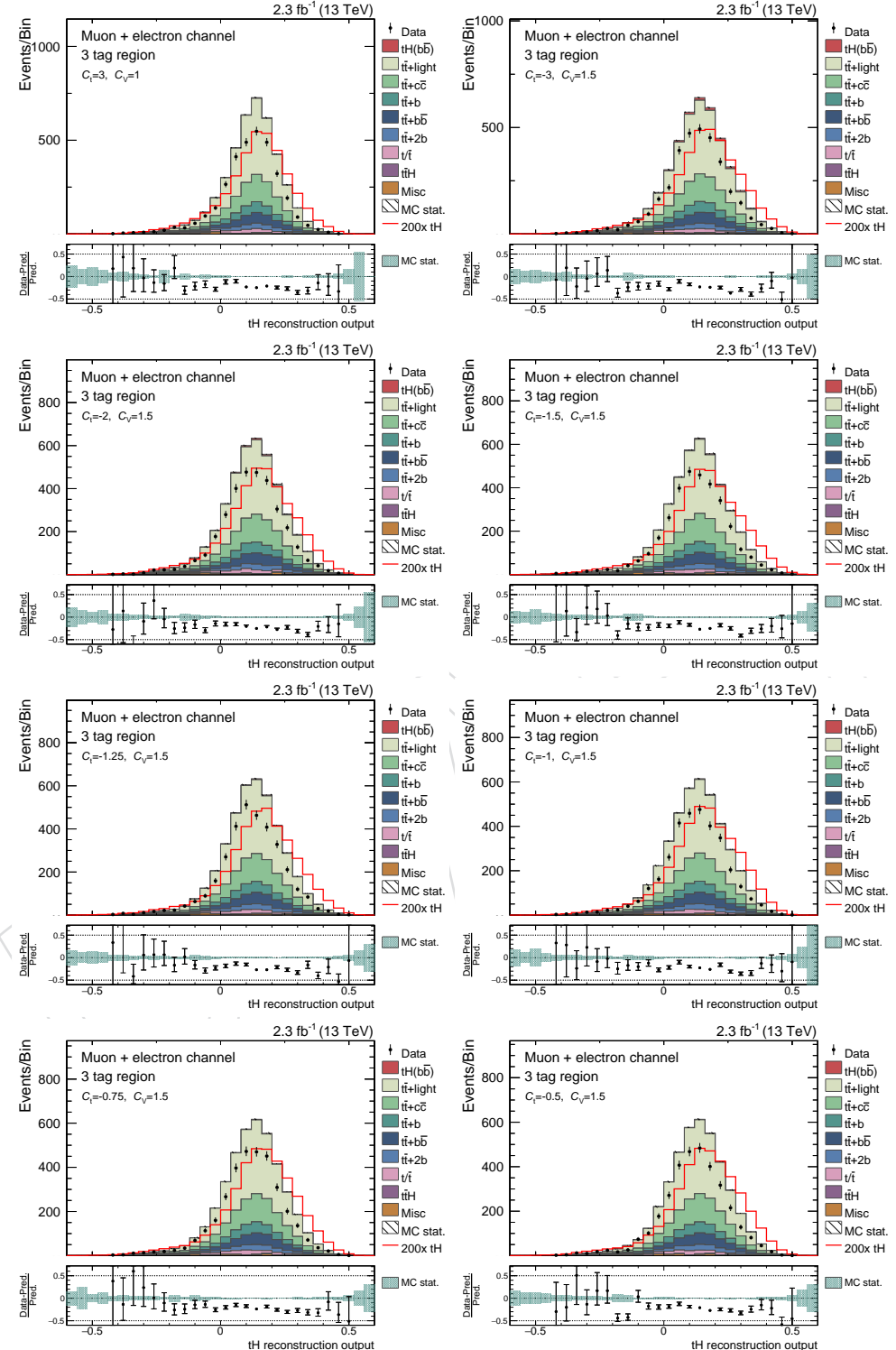


Figure 45: The output of  $tHq$  reconstruction BDT at 13 TeV in the 3 tag region for the different signal hypotheses is shown in this figure.

## E Appendix E: BDT output distributions

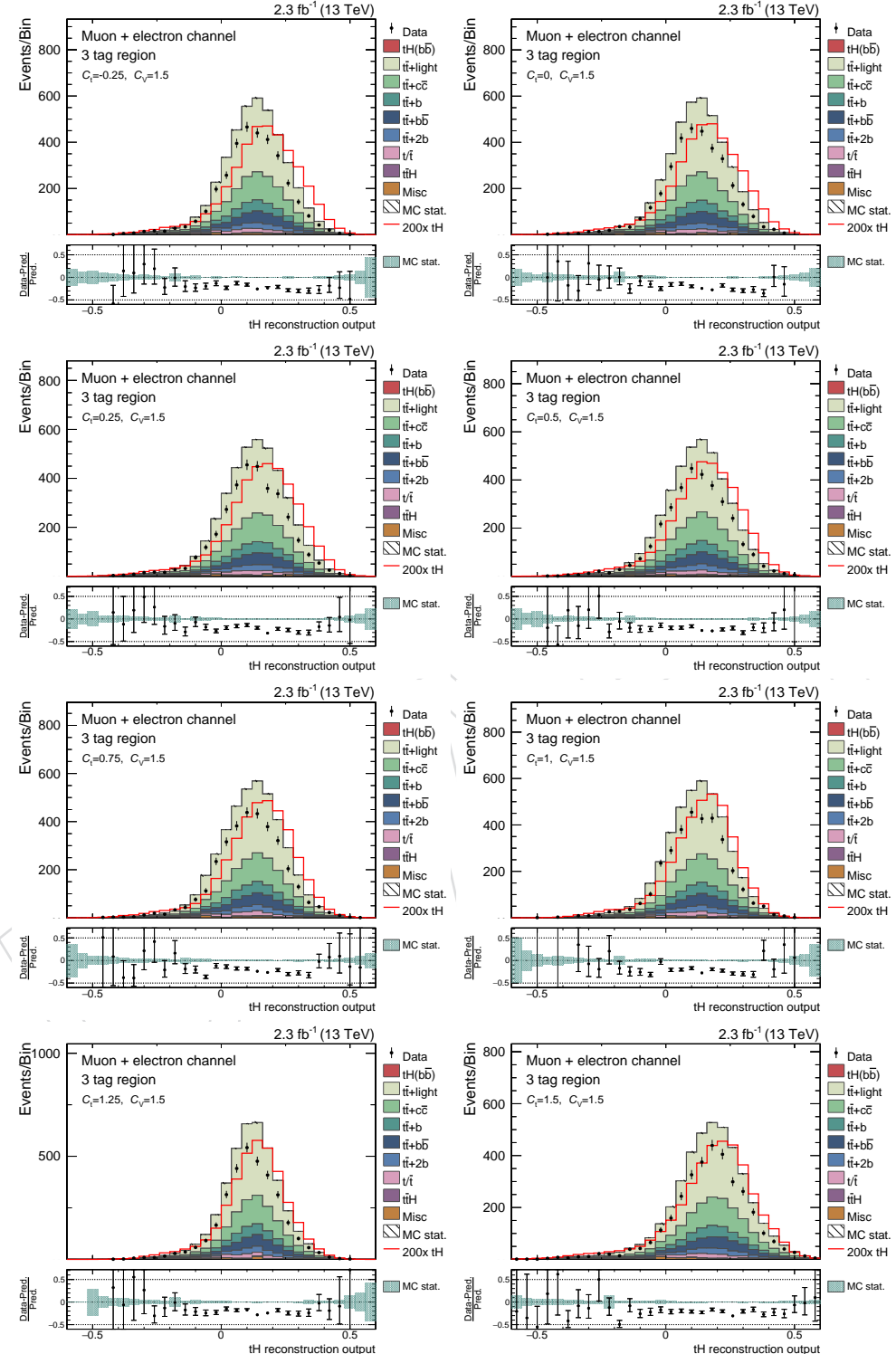


Figure 46: The output of  $tHq$  reconstruction BDT at 13 TeV in the 3 tag region for the different signal hypotheses is shown in this figure.

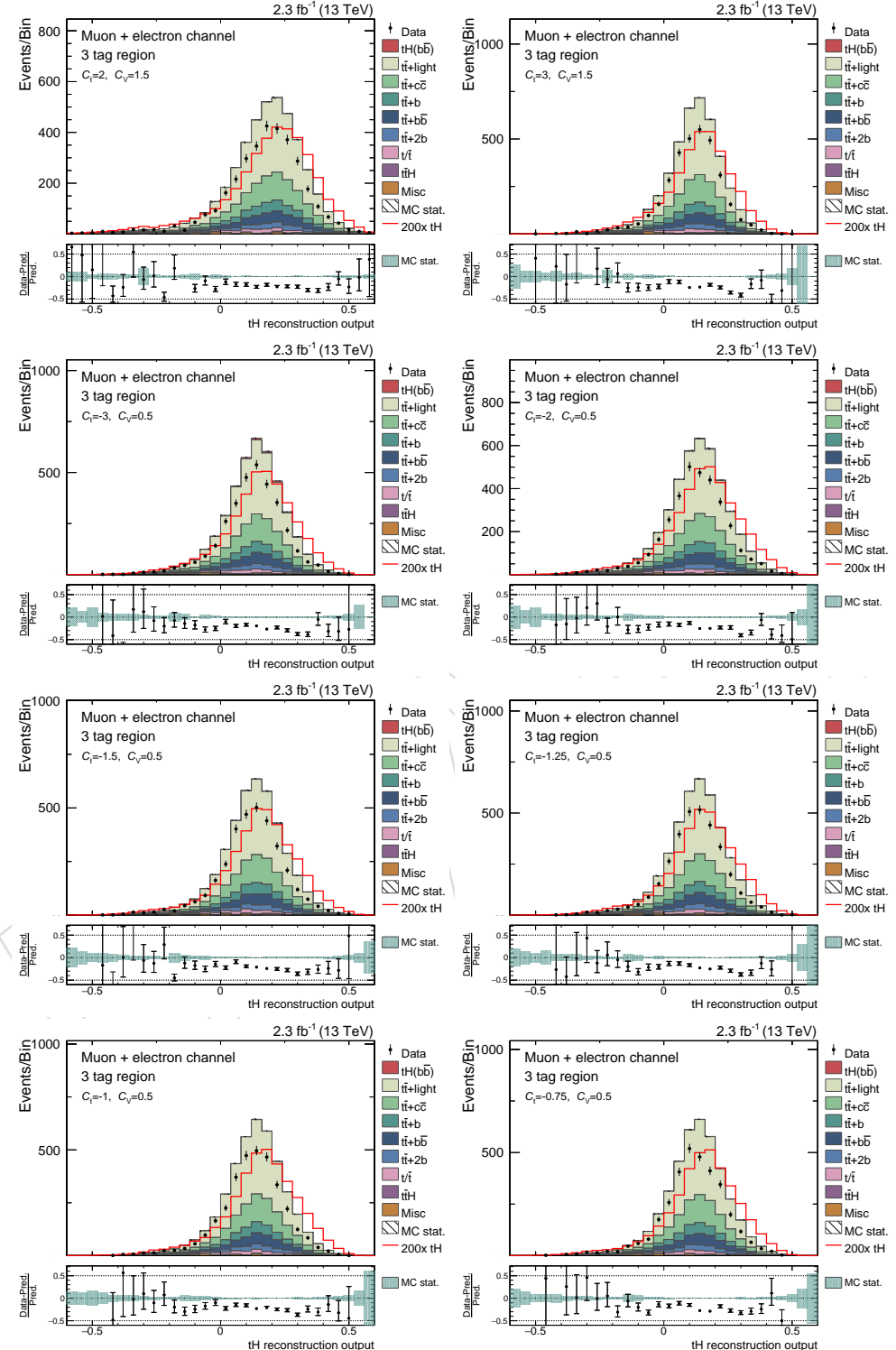


Figure 47: The output of  $tHq$  reconstruction BDT at 13 TeV in the 3 tag region for the different signal hypotheses is shown in this figure.

## E Appendix E: BDT output distributions

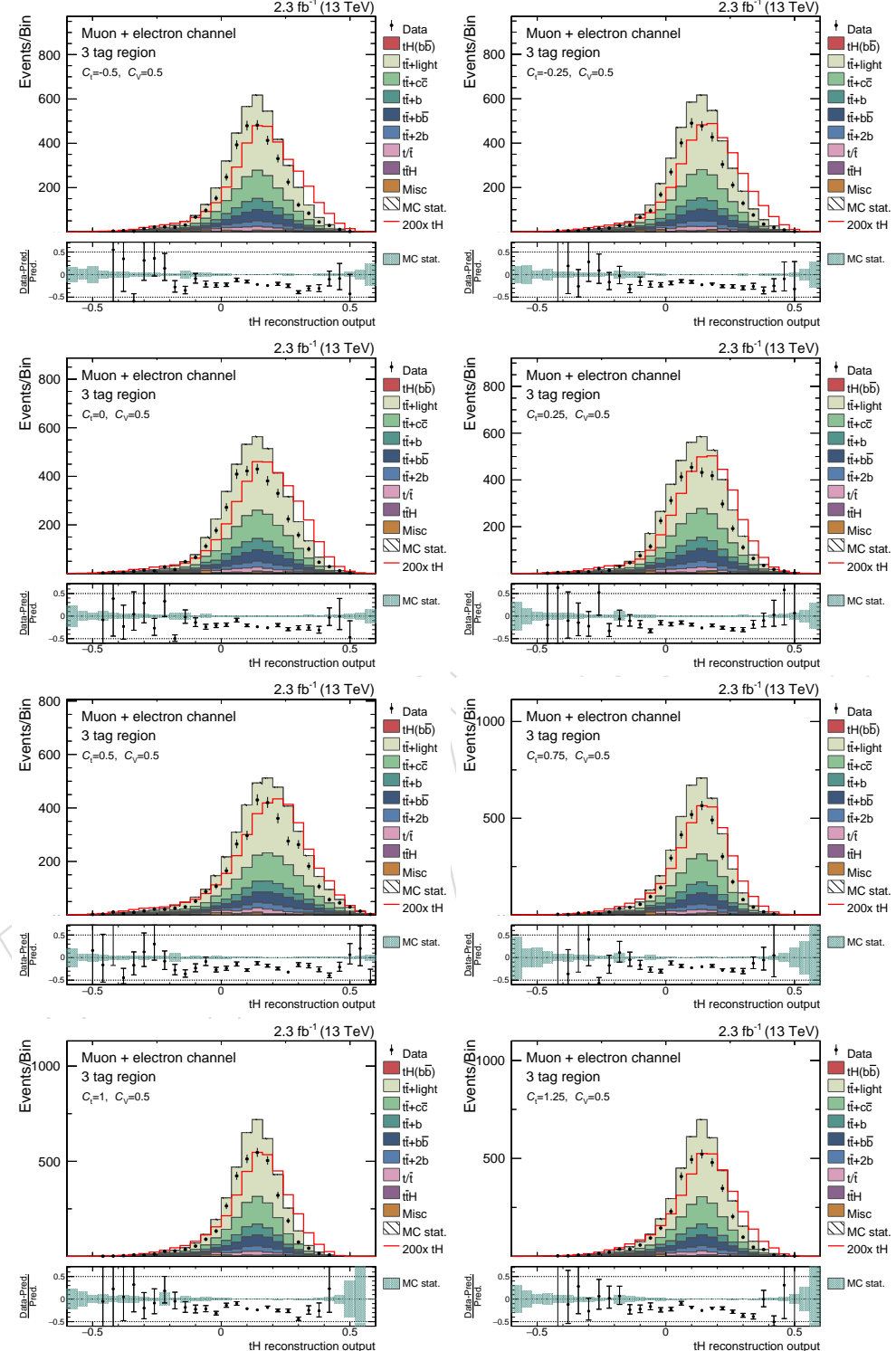


Figure 48: The output of tHq reconstruction BDT at 13 TeV in the 3 tag region for the different signal hypotheses is shown in this figure.

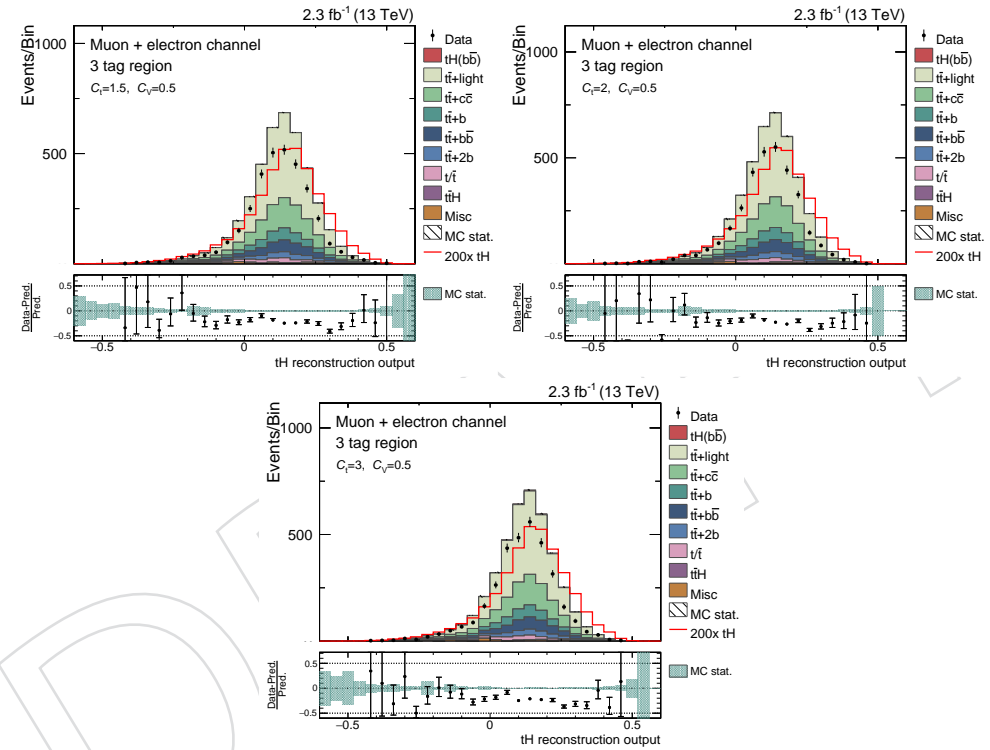


Figure 49: The output of  $t\bar{H}q$  reconstruction BDT at 13 TeV in the 3 tag region for the different signal hypotheses is shown in this figure.

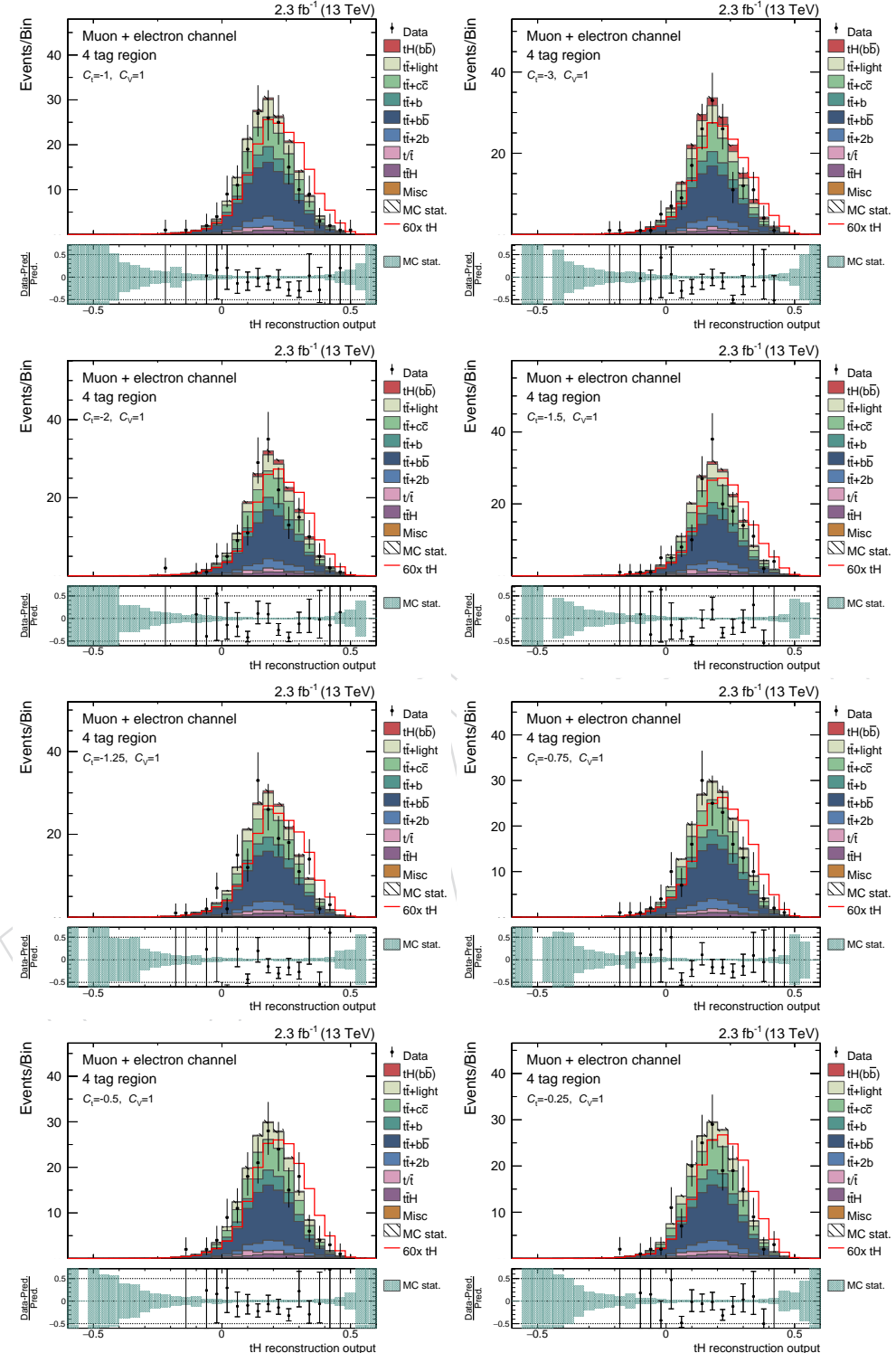


Figure 50: The output of tHq reconstruction BDT at 13 TeV in the 4 tag region for the different signal hypotheses is shown in this figure.

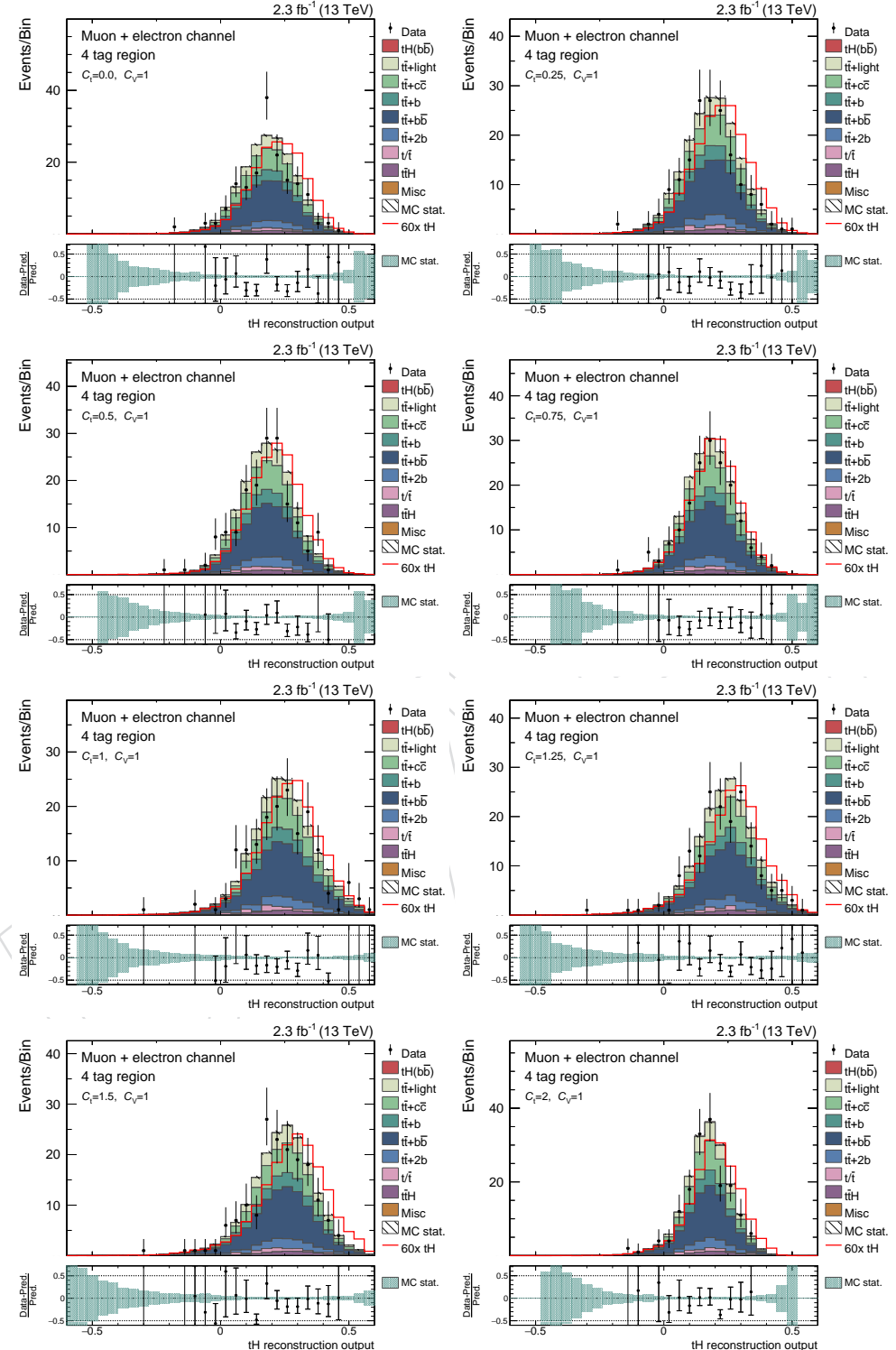


Figure 51: The output of  $tHq$  reconstruction BDT at 13 TeV in the 4 tag region for the different signal hypotheses is shown in this figure.

## E Appendix E: BDT output distributions

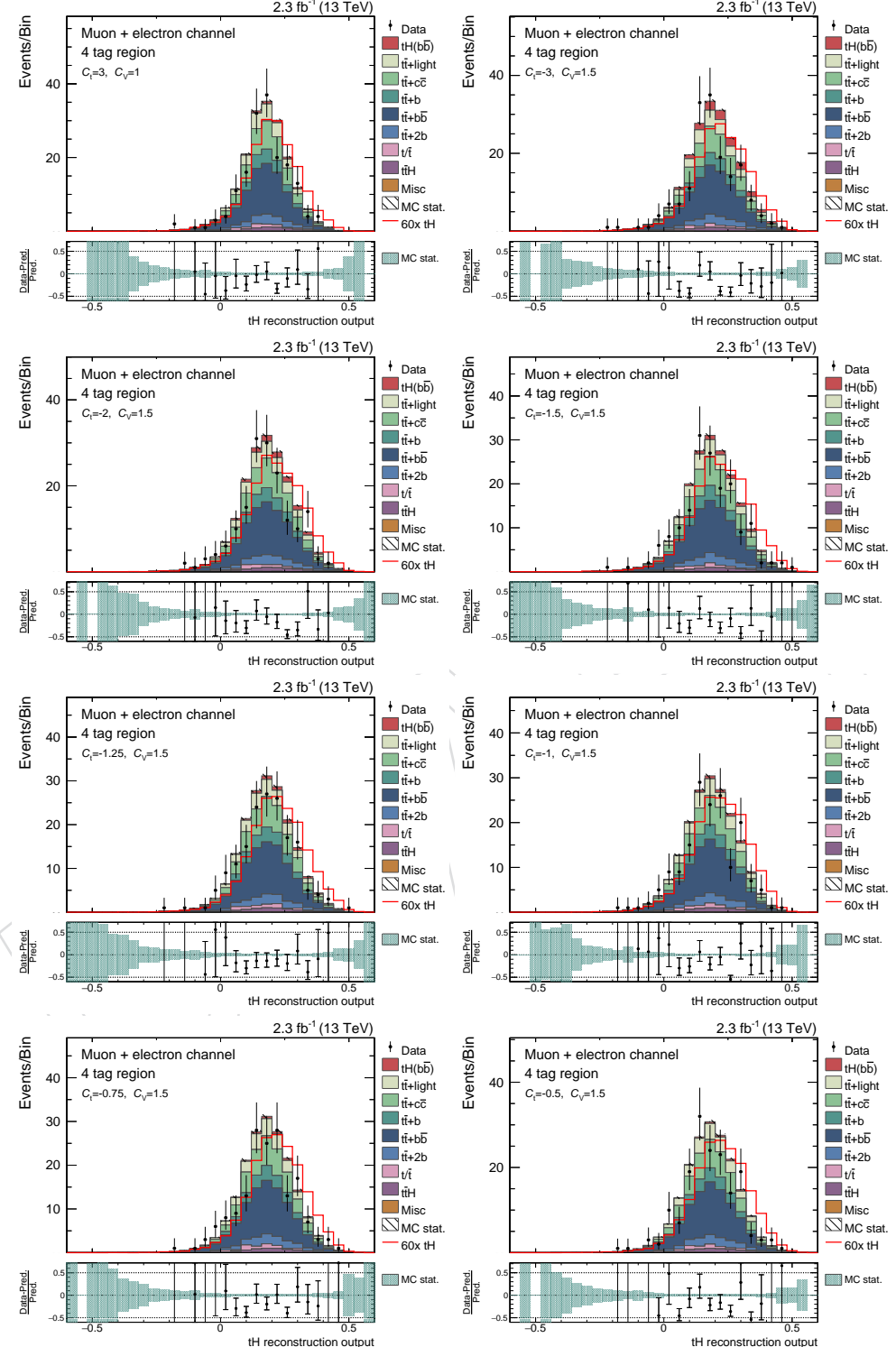


Figure 52: The output of  $t\bar{t}Hq$  reconstruction BDT at 13 TeV in the 4 tag region for the different signal hypotheses is shown in this figure.

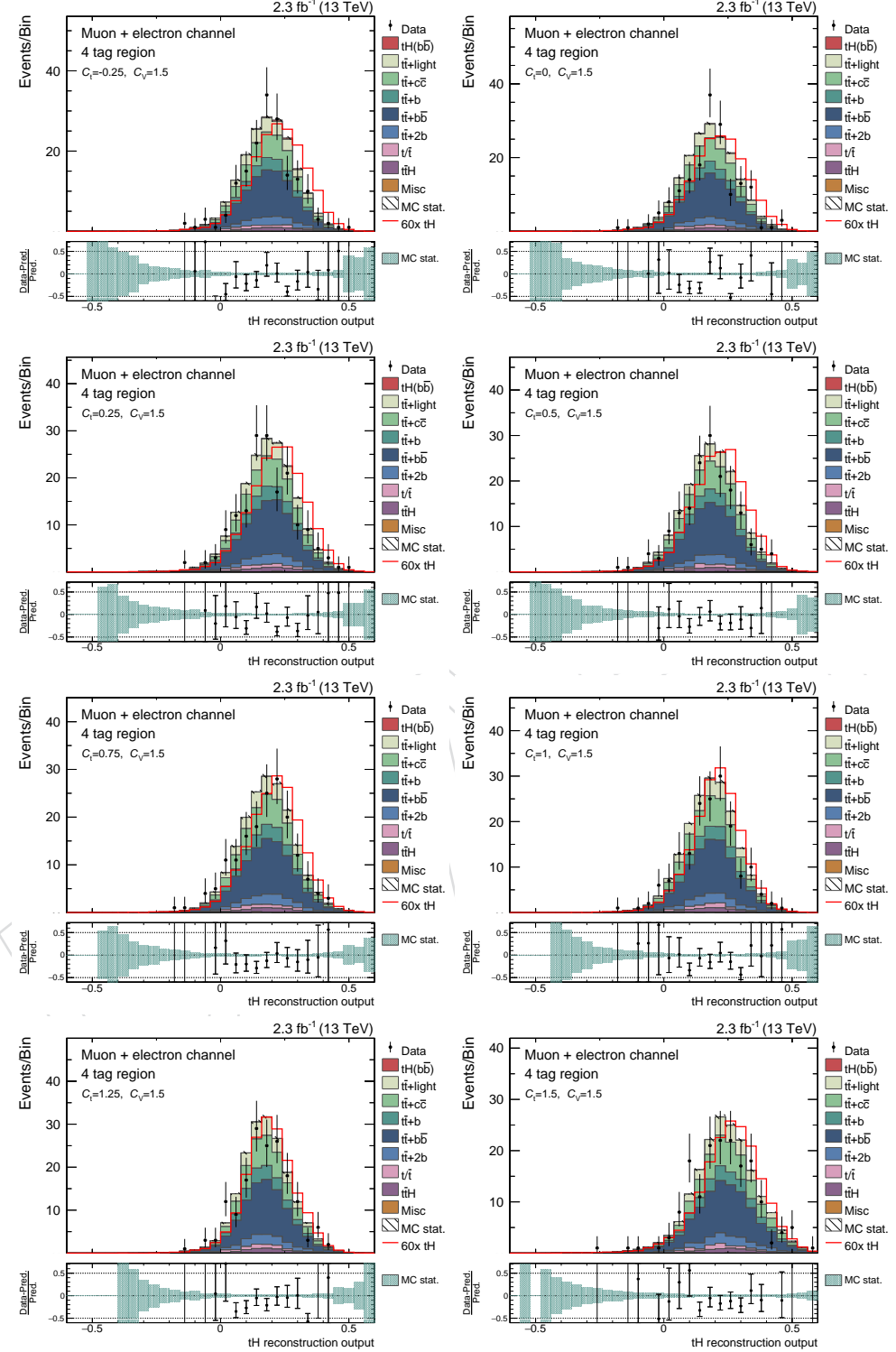


Figure 53: The output of  $tHq$  reconstruction BDT at 13 TeV in the 4 tag region for the different signal hypotheses is shown in this figure.

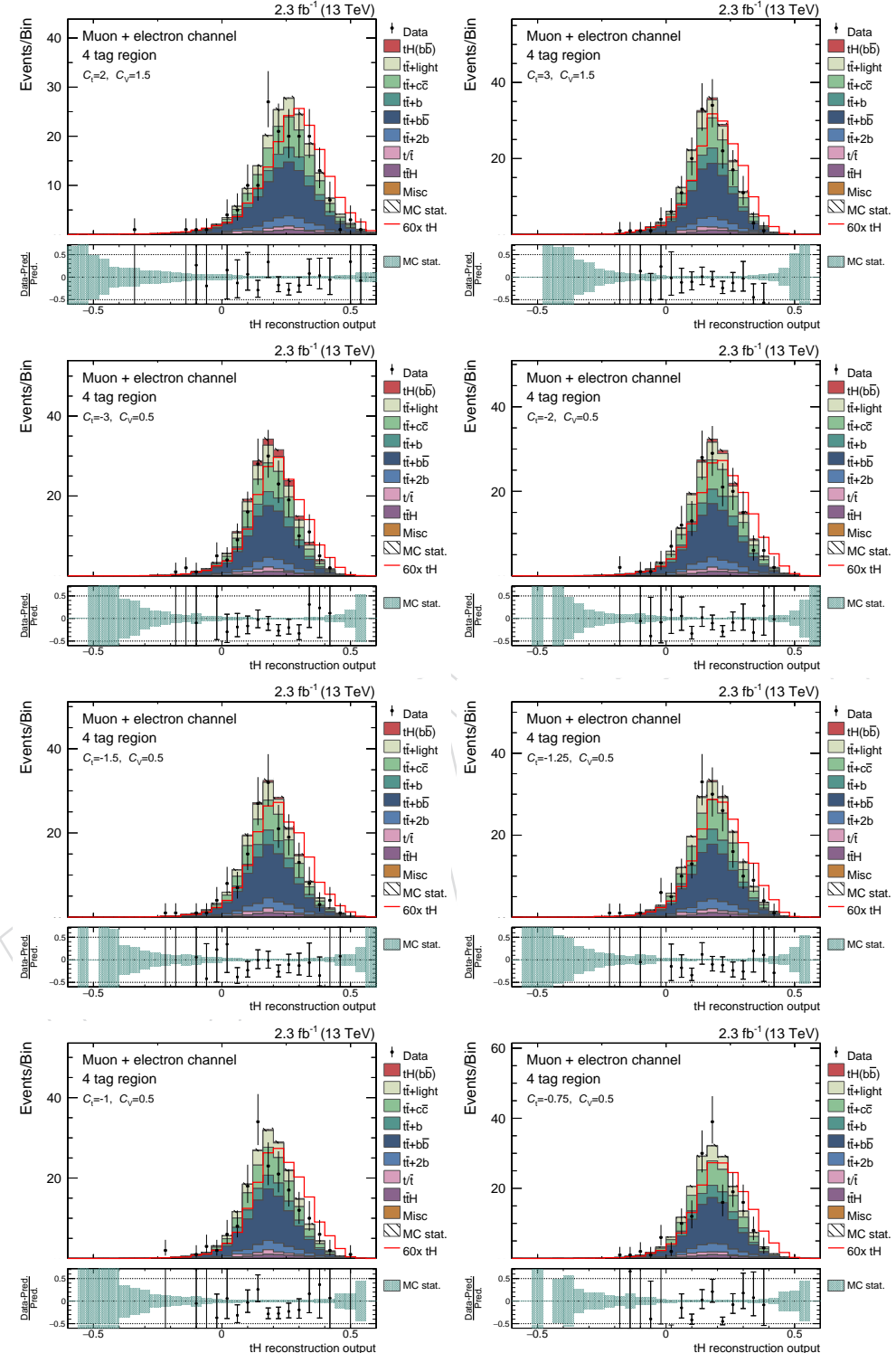


Figure 54: The output of tHq reconstruction BDT at 13 TeV in the 4 tag region for the different signal hypotheses is shown in this figure.

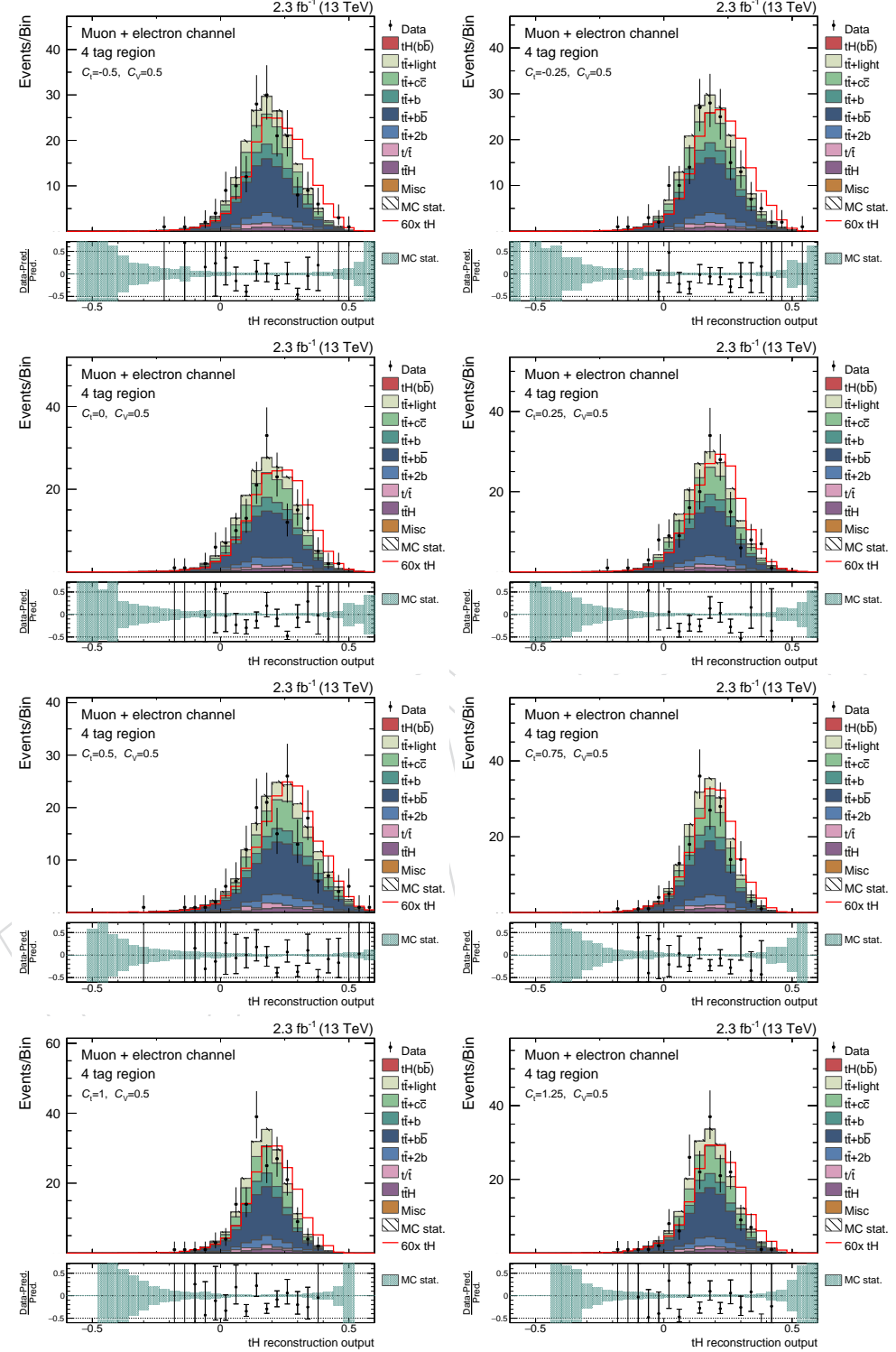


Figure 55: The output of  $tHq$  reconstruction BDT at 13 TeV in the 4 tag region for the different signal hypotheses is shown in this figure.

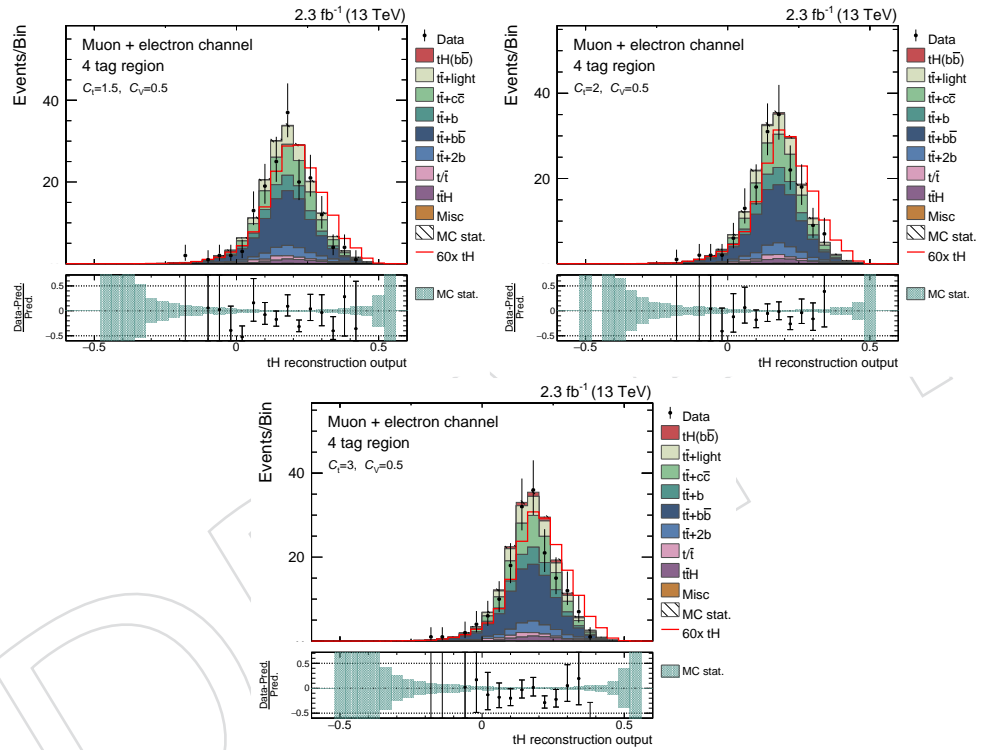


Figure 56: The output of  $tHq$  reconstruction BDT at 13 TeV in the 4 tag region for the different signal hypotheses is shown in this figure.

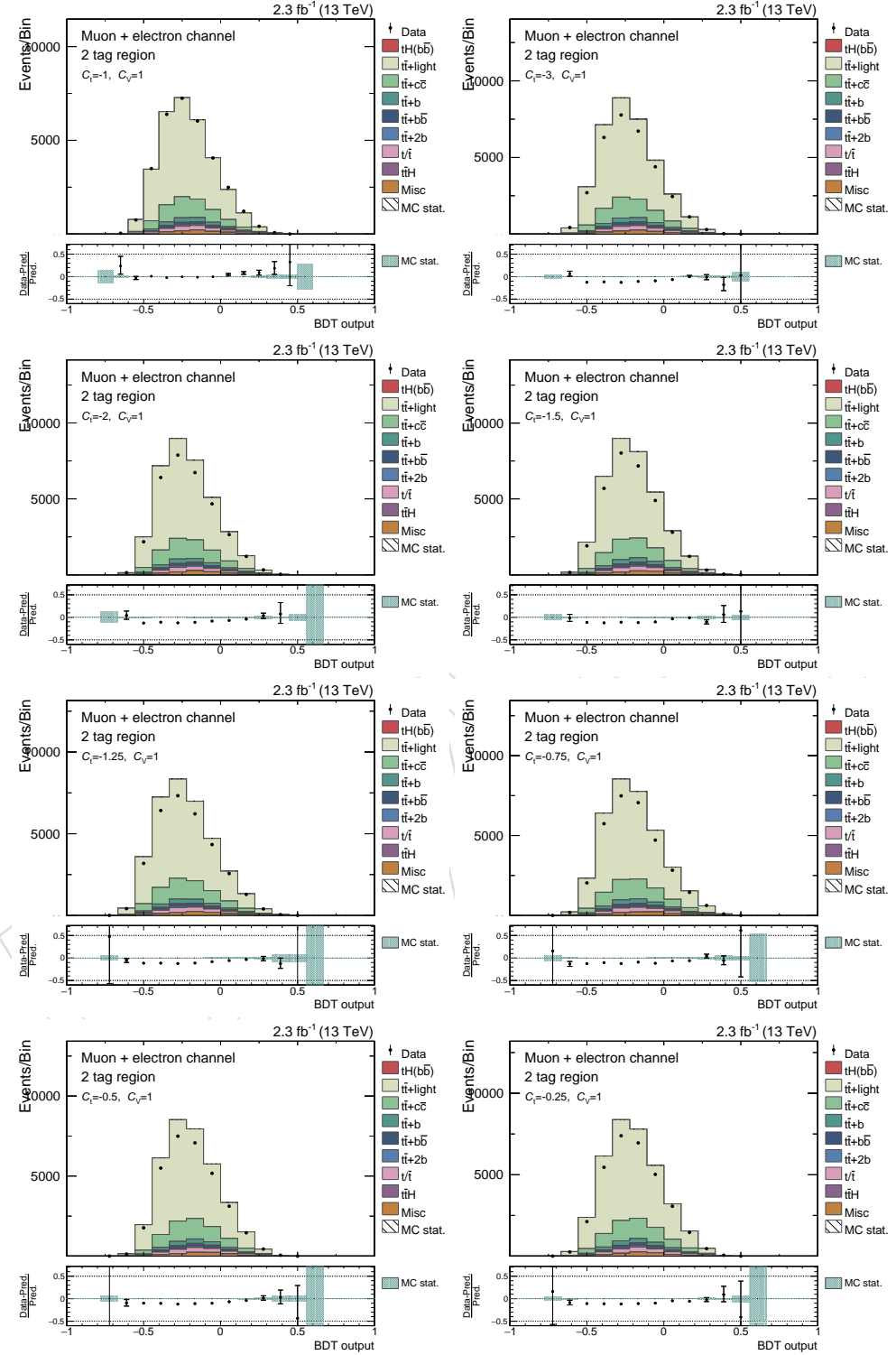


Figure 57: The output of classification BDT at 13 TeV in the 2 tag region for the different signal hypotheses is shown in this figure.

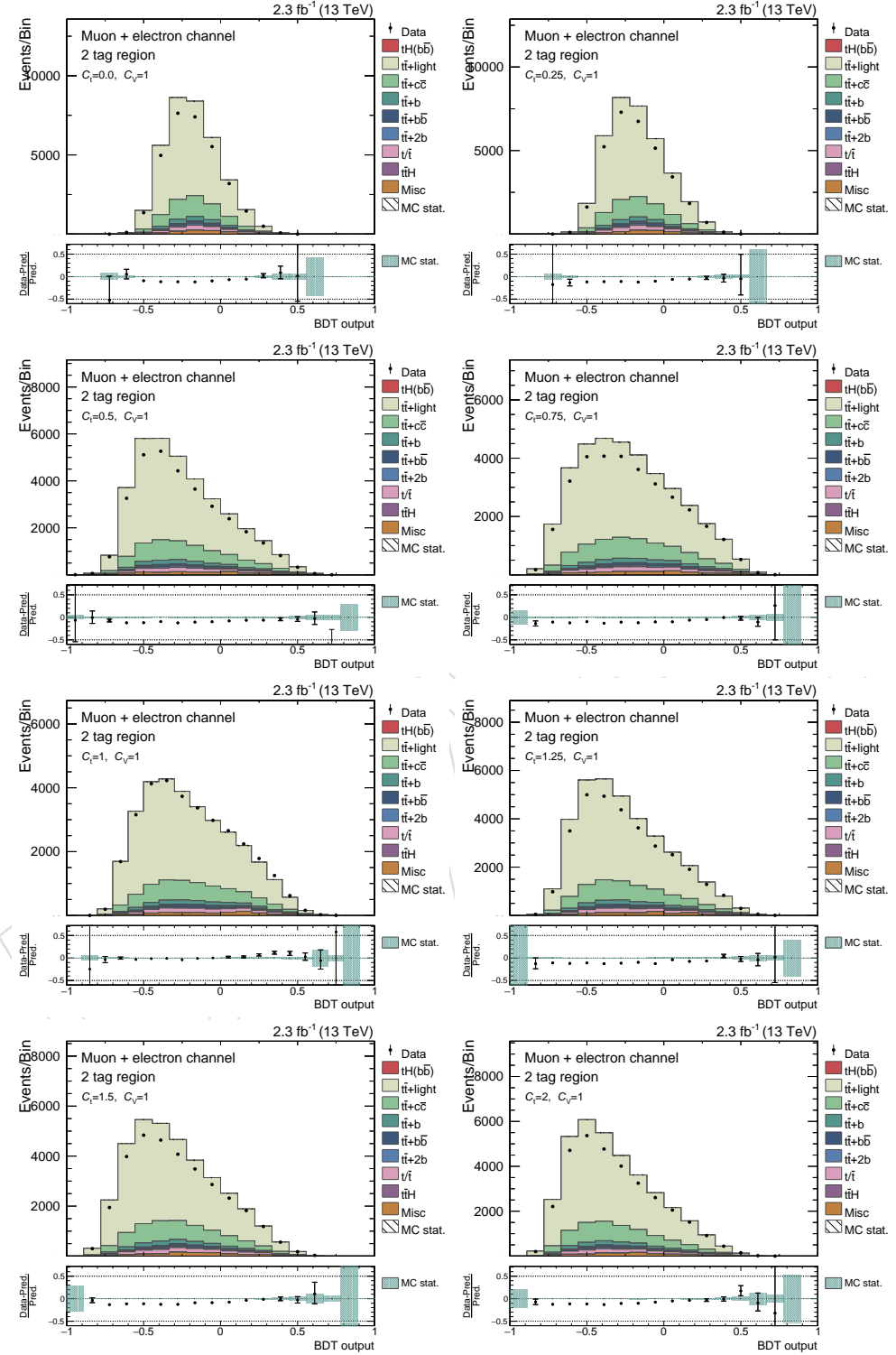


Figure 58: The output of classification BDT at 13 TeV in the 2 tag region for the different signal hypotheses is shown in this figure.

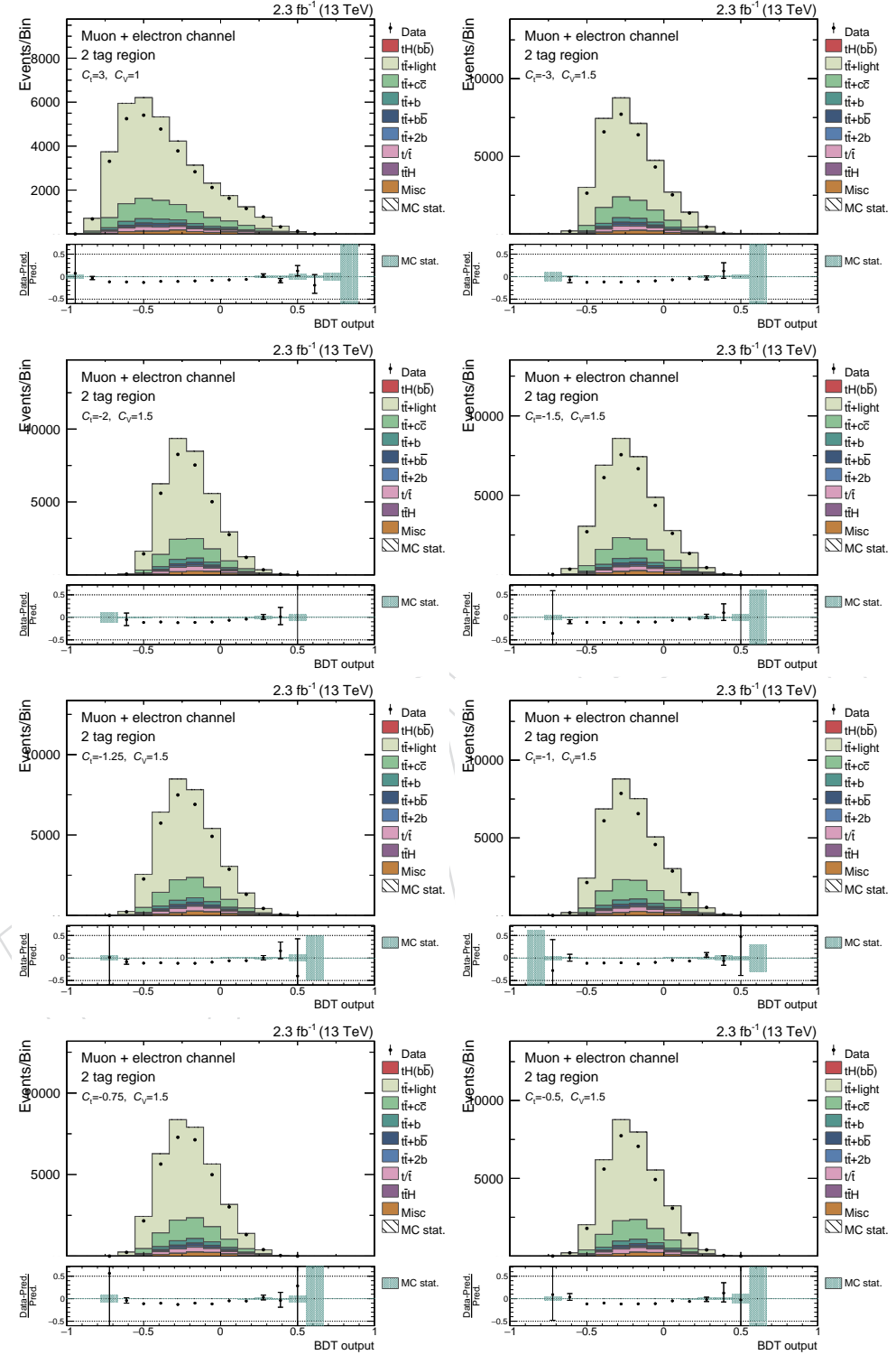


Figure 59: The output of classification BDT at 13 TeV in the 2 tag region for the different signal hypotheses is shown in this figure.

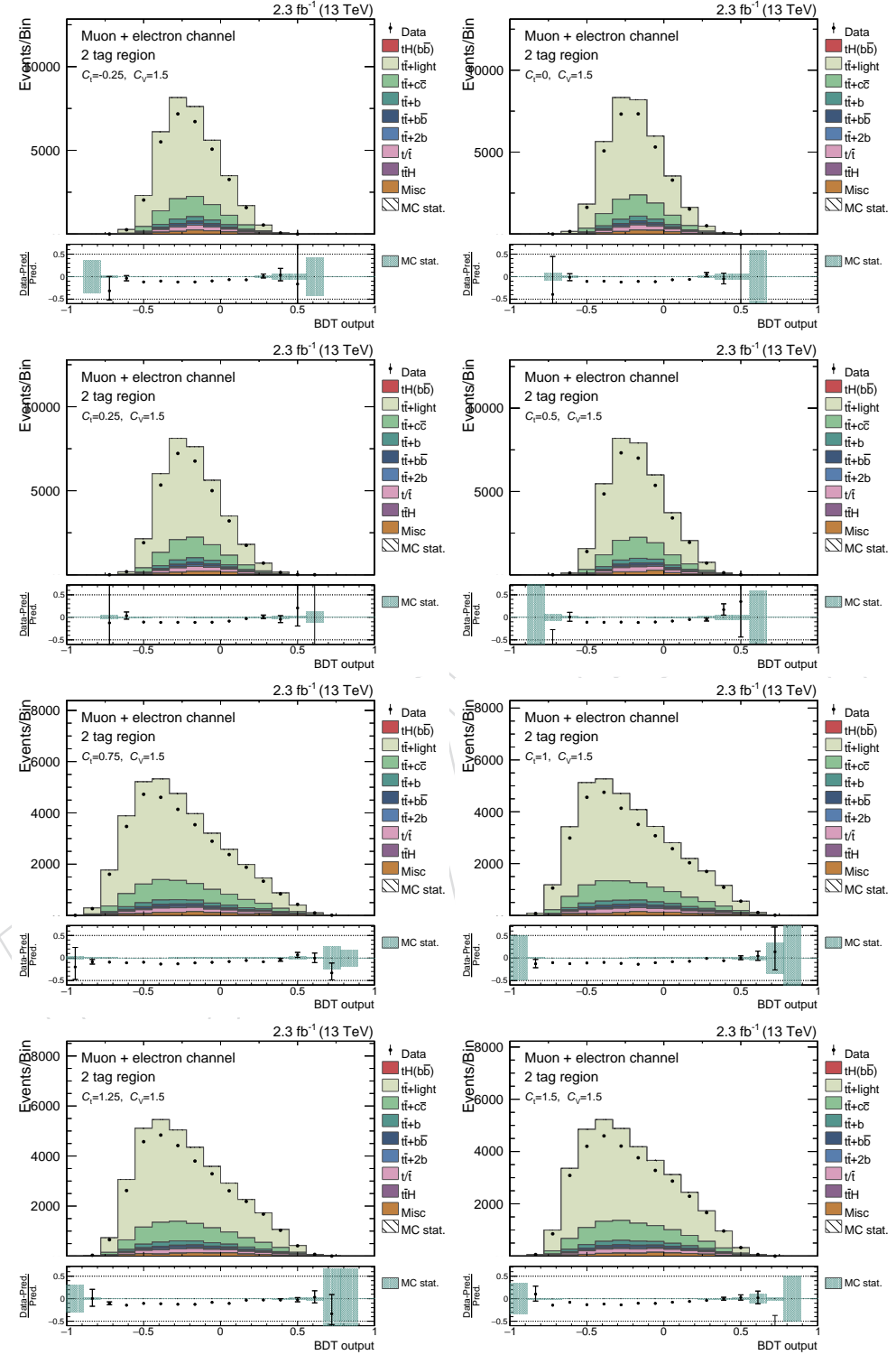


Figure 60: The output of classification BDT at 13 TeV in the 2 tag region for the different signal hypotheses is shown in this figure.

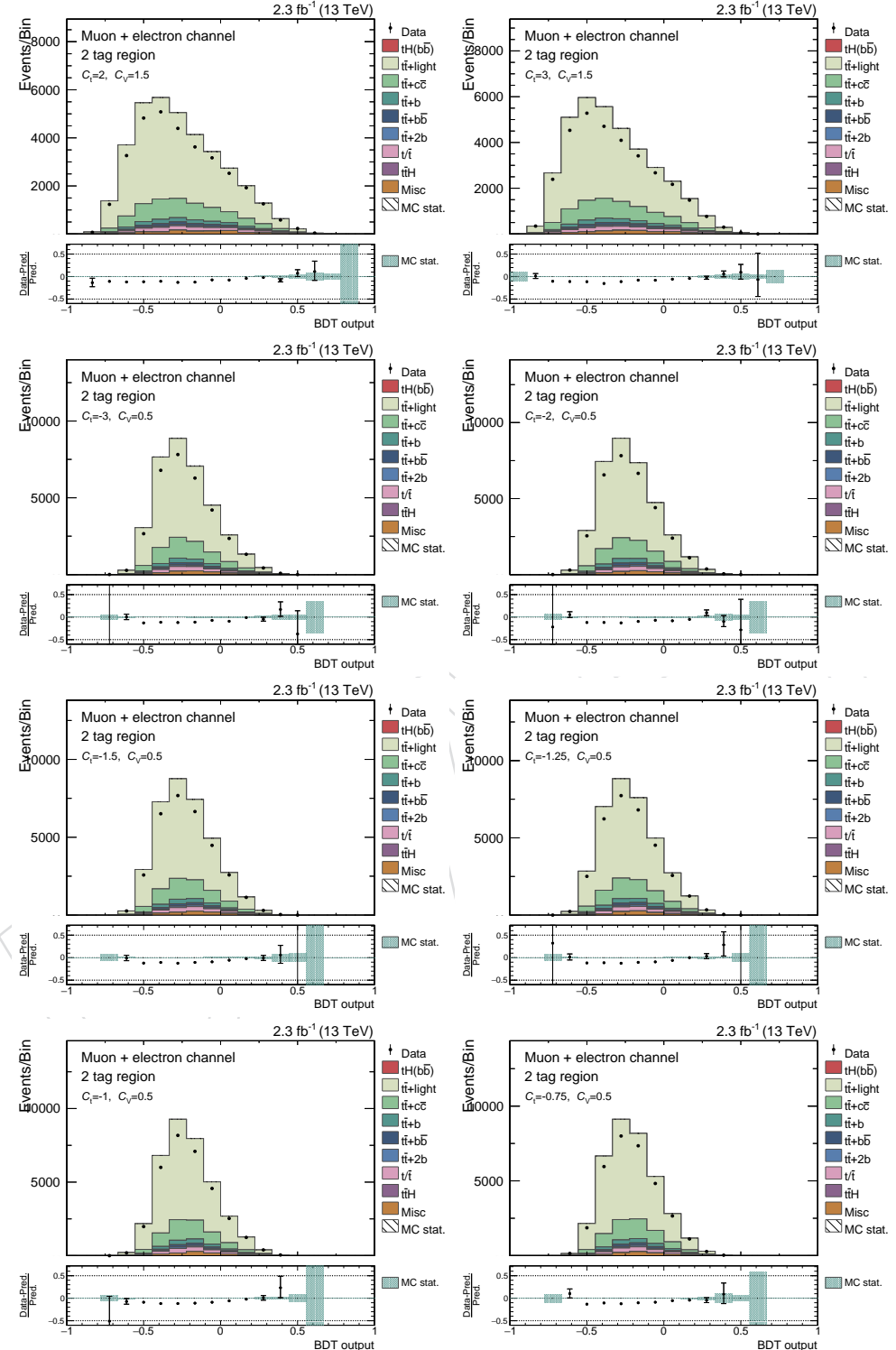


Figure 61: The output of classification BDT at 13 TeV in the 2 tag region for the different signal hypotheses is shown in this figure.

## E Appendix E: BDT output distributions

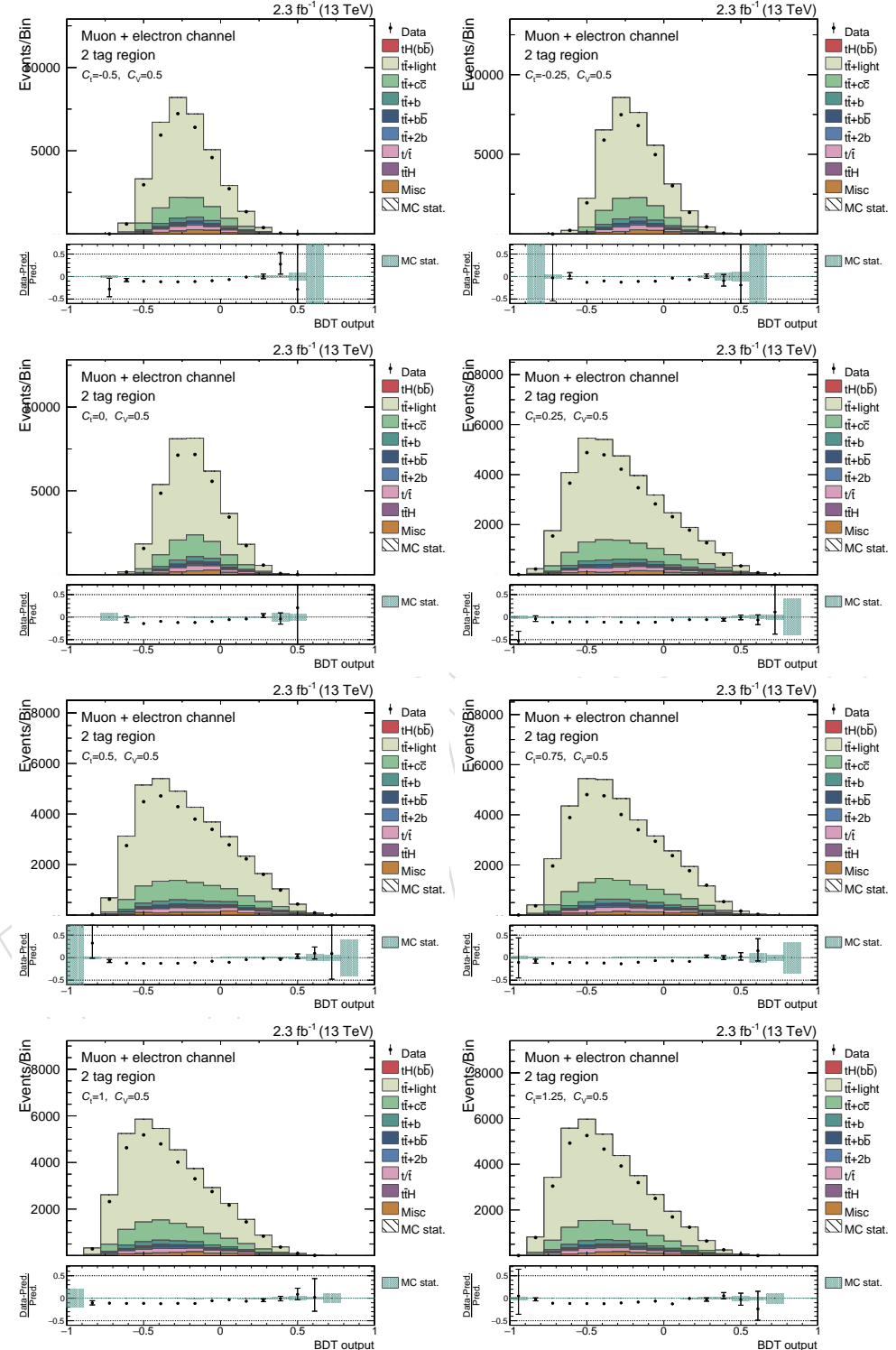


Figure 62: The output of classification BDT at 13 TeV in the 2 tag region for the different signal hypotheses is shown in this figure.

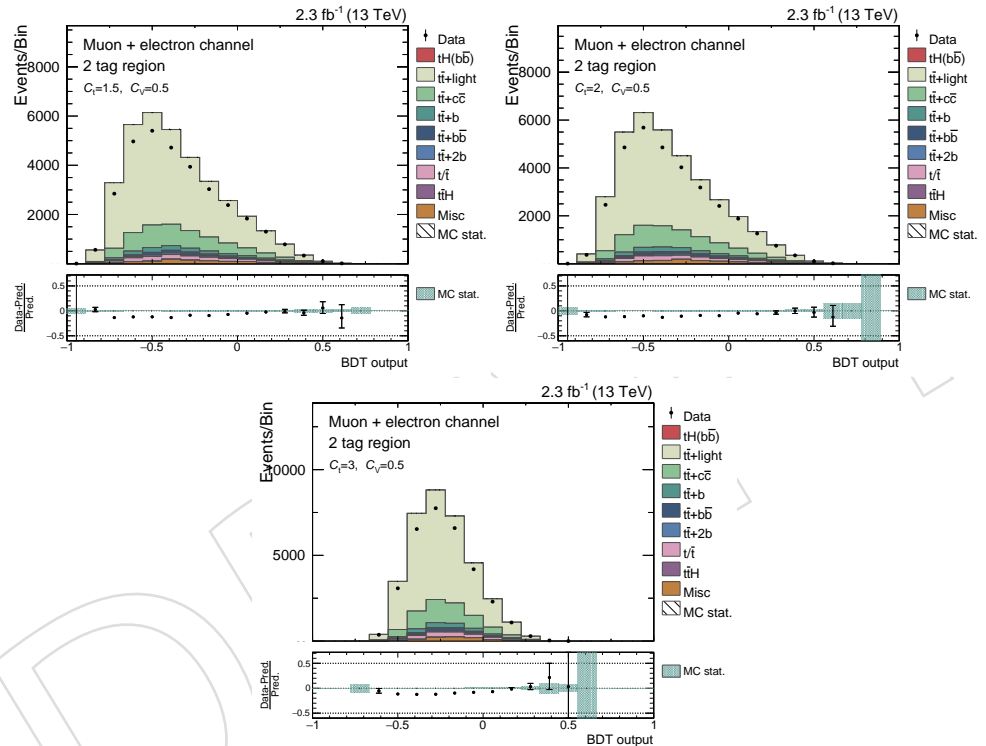


Figure 63: The output of classification BDT at 13 TeV in the 2 tag region for the different signal hypotheses is shown in this figure.

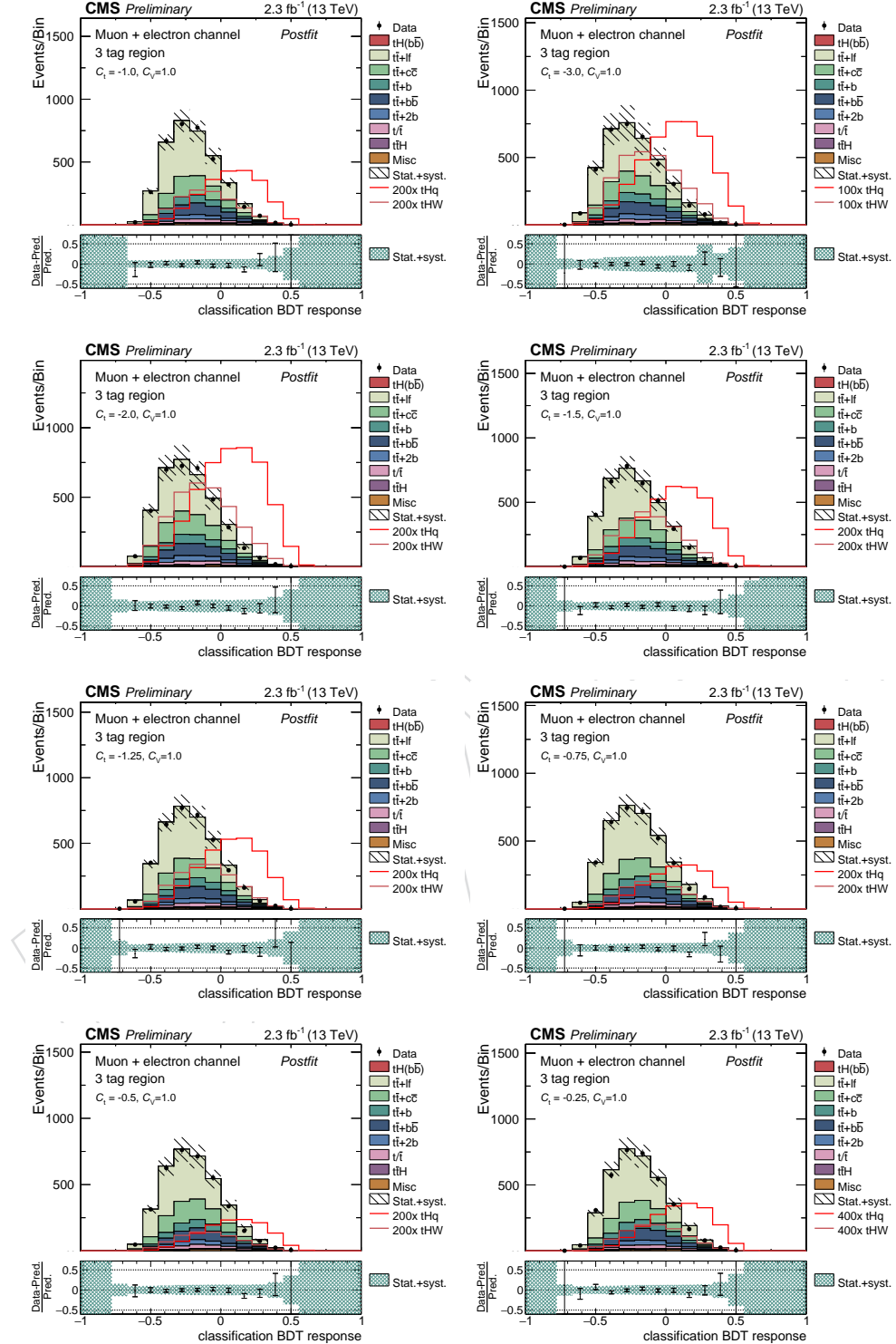


Figure 64: The output of classification BDT at 13 TeV in the 3 tag region for the different signal hypotheses is shown in this figure.

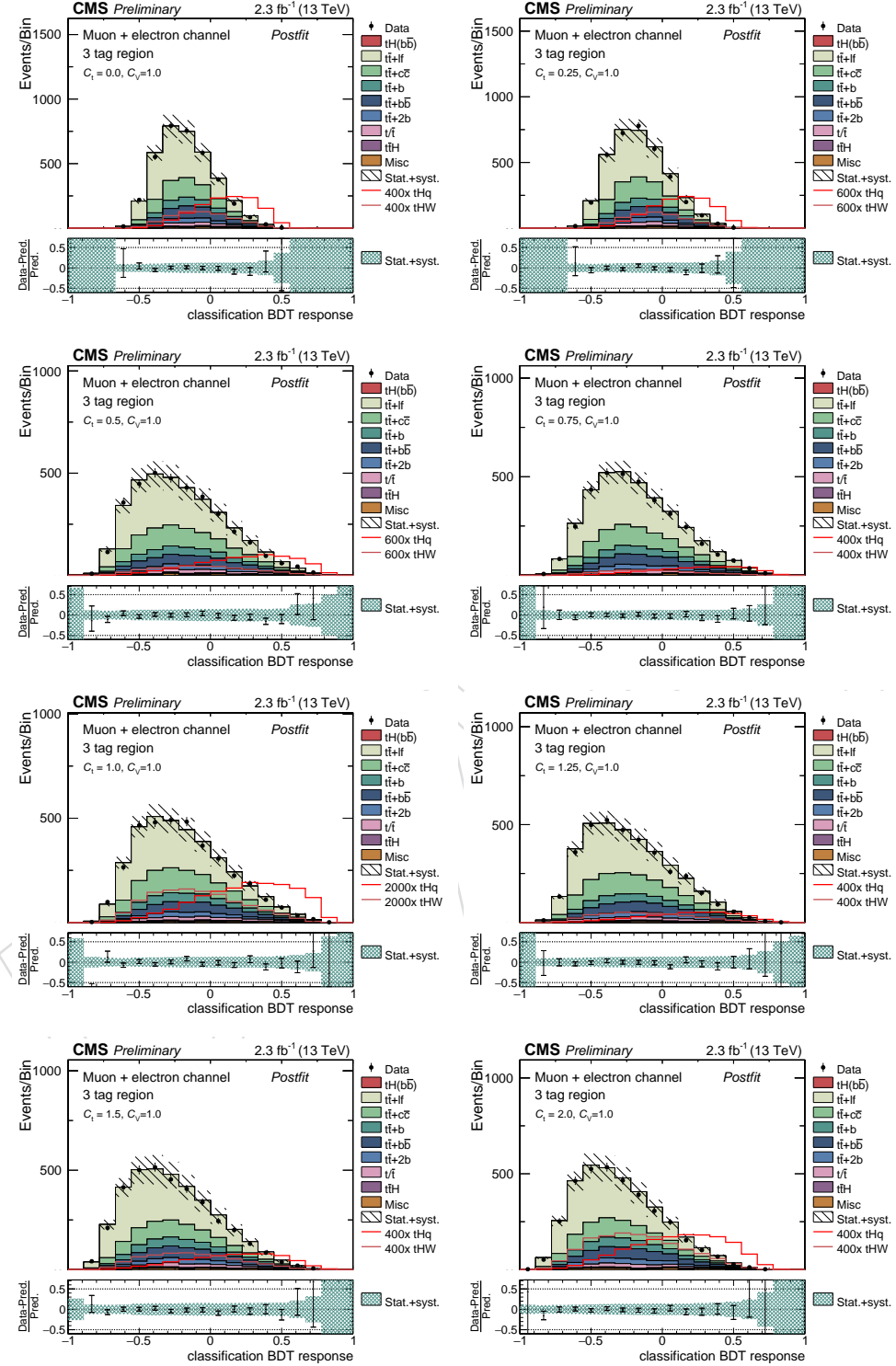


Figure 65: The output of classification BDT at 13 TeV in the 3 tag region for the different signal hypotheses is shown in this figure.

## E Appendix E: BDT output distributions

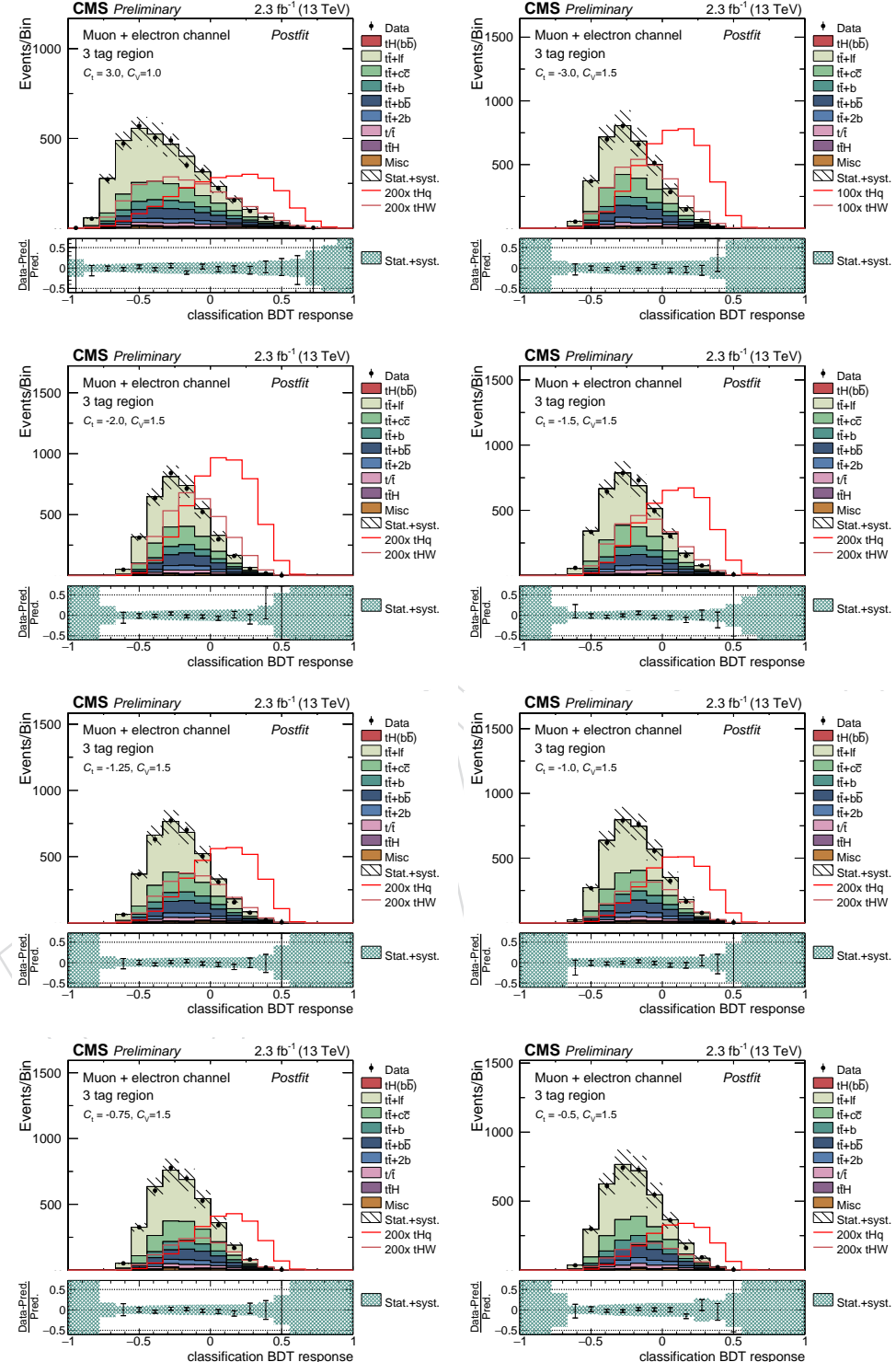


Figure 66: The output of classification BDT at 13 TeV in the 3 tag region for the different signal hypotheses is shown in this figure.

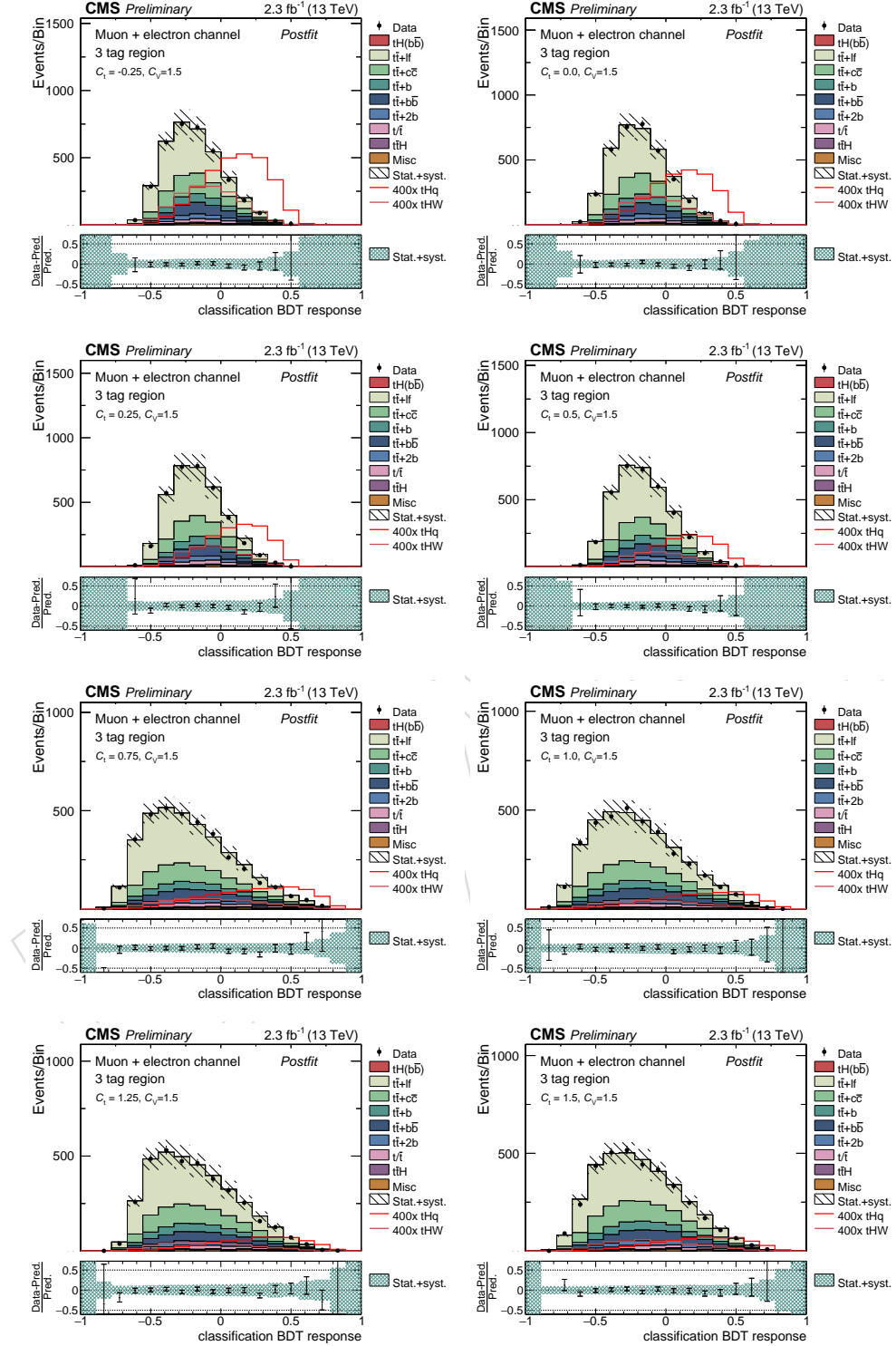


Figure 67: The output of classification BDT at 13 TeV in the 3 tag region for the different signal hypotheses is shown in this figure.

## E Appendix E: BDT output distributions

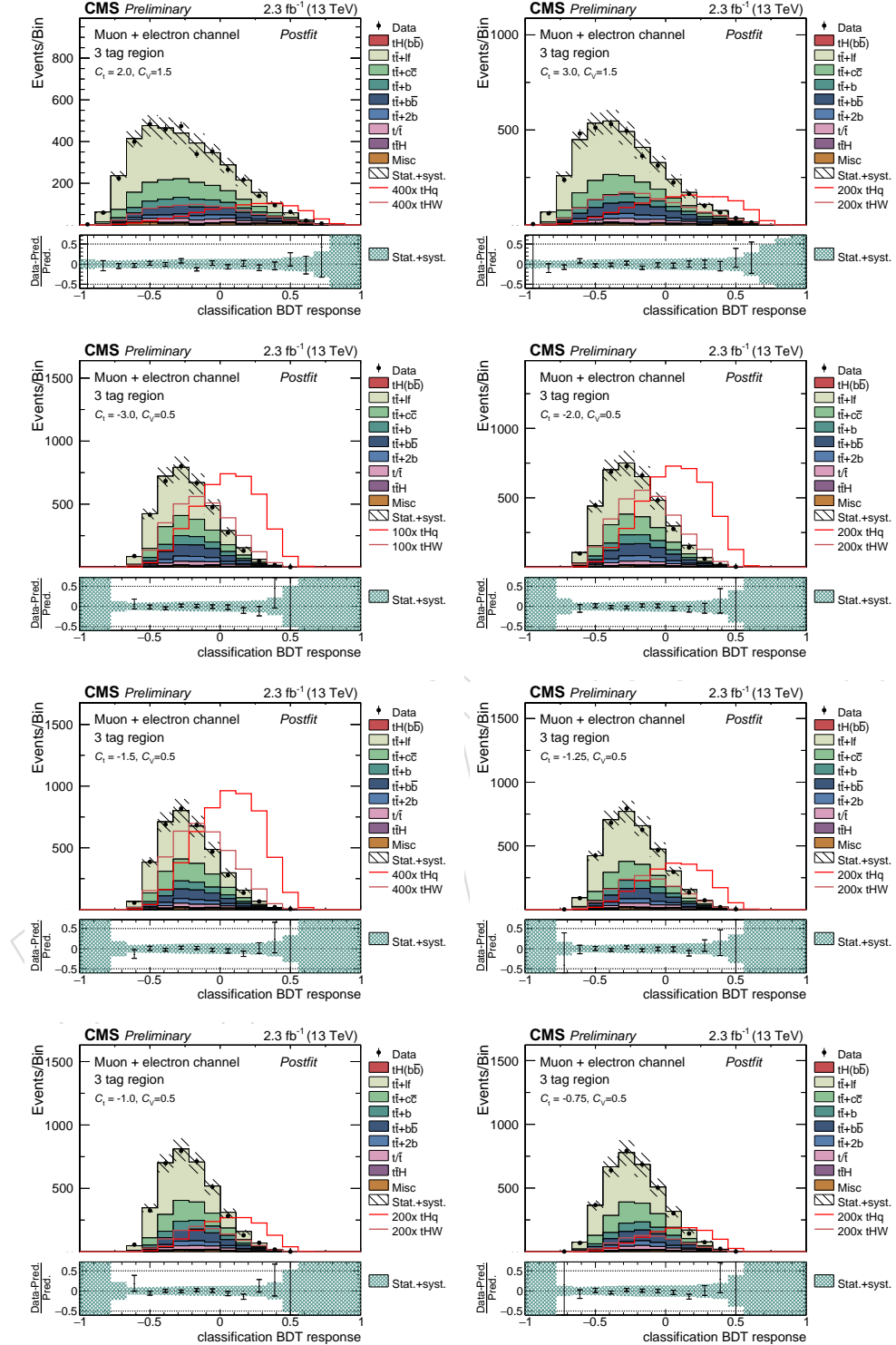


Figure 68: The output of classification BDT at 13 TeV in the 3 tag region for the different signal hypotheses is shown in this figure.

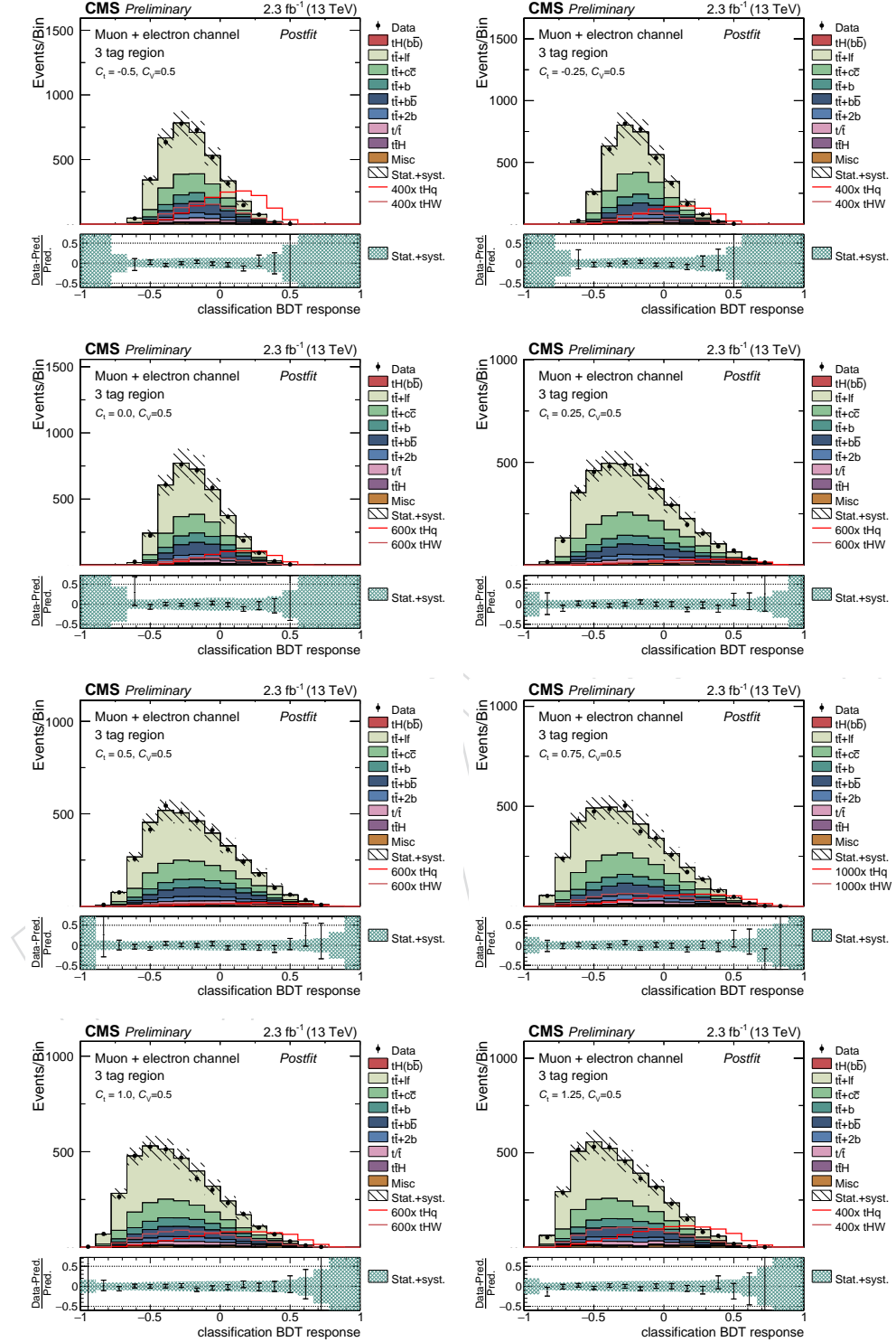


Figure 69: The output of classification BDT at 13 TeV in the 3 tag region for the different signal hypotheses is shown in this figure.

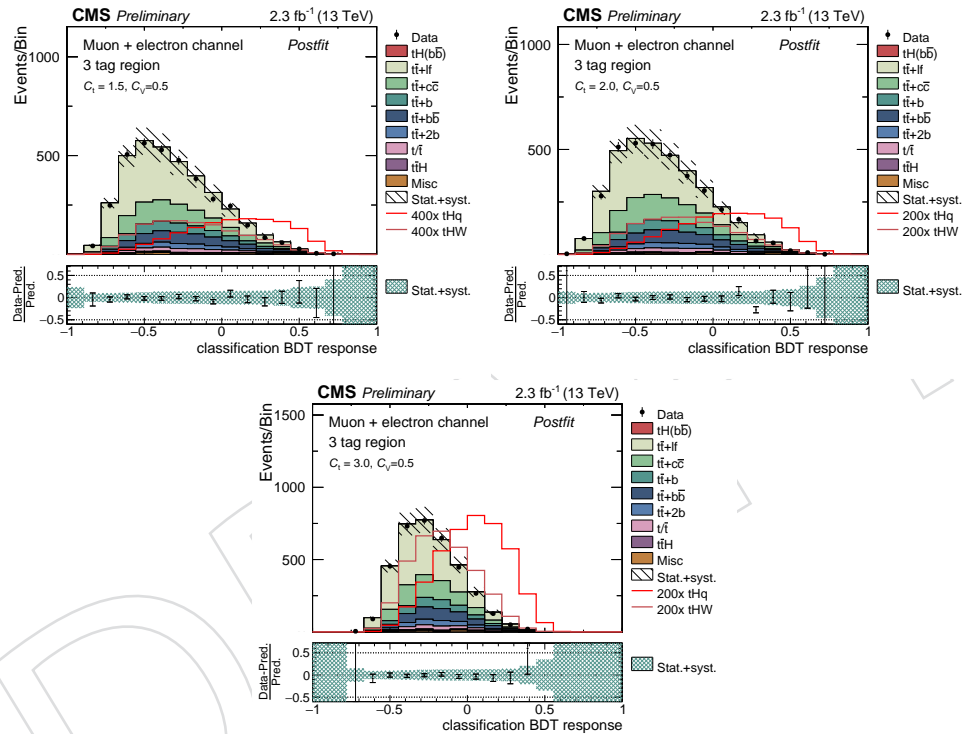


Figure 70: The output of classification BDT at 13 TeV in the 3 tag region for the different signal hypotheses is shown in this figure.

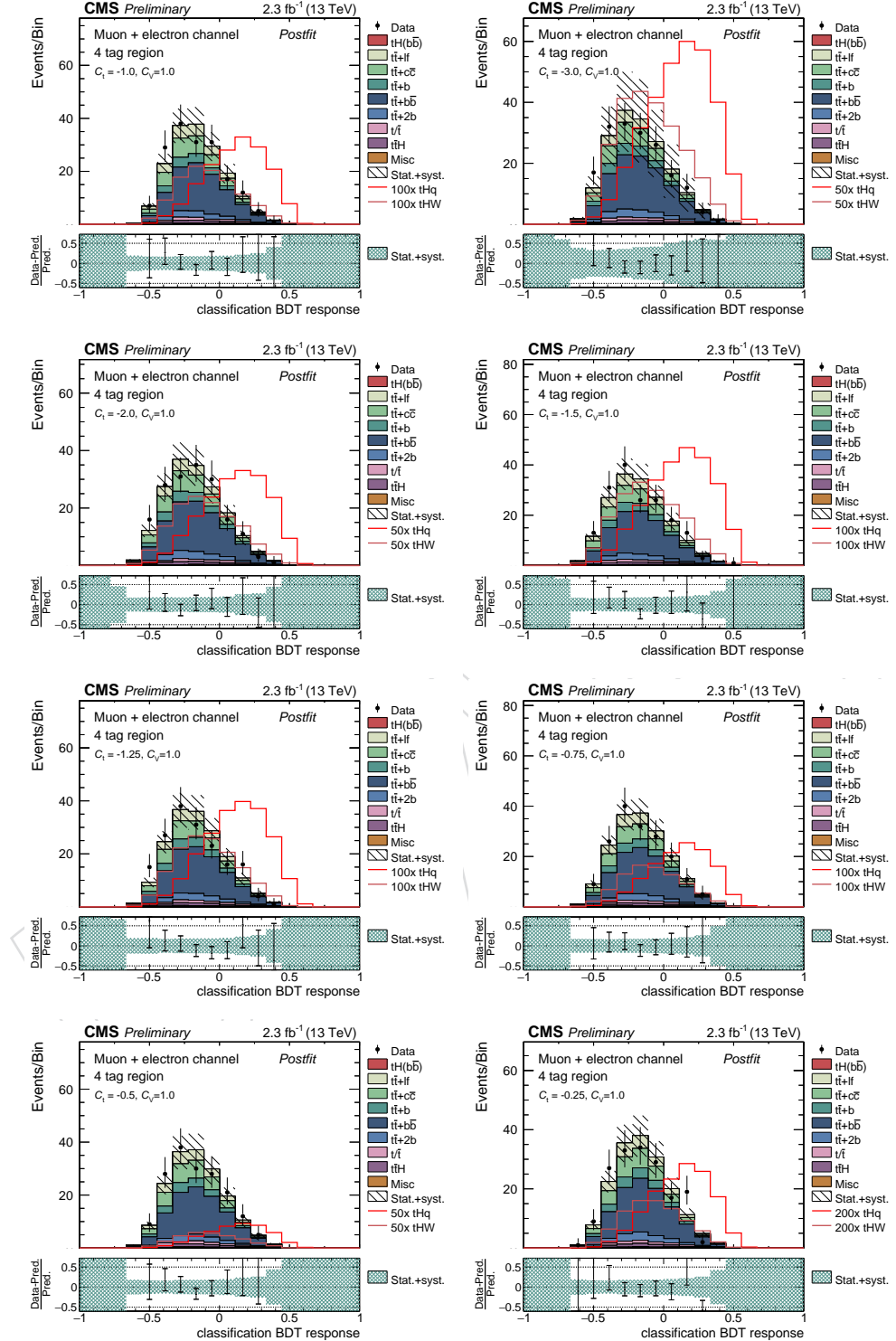


Figure 71: The output of classification BDT at 13 TeV in the 4 tag region for the different signal hypotheses is shown in this figure.

## E Appendix E: BDT output distributions

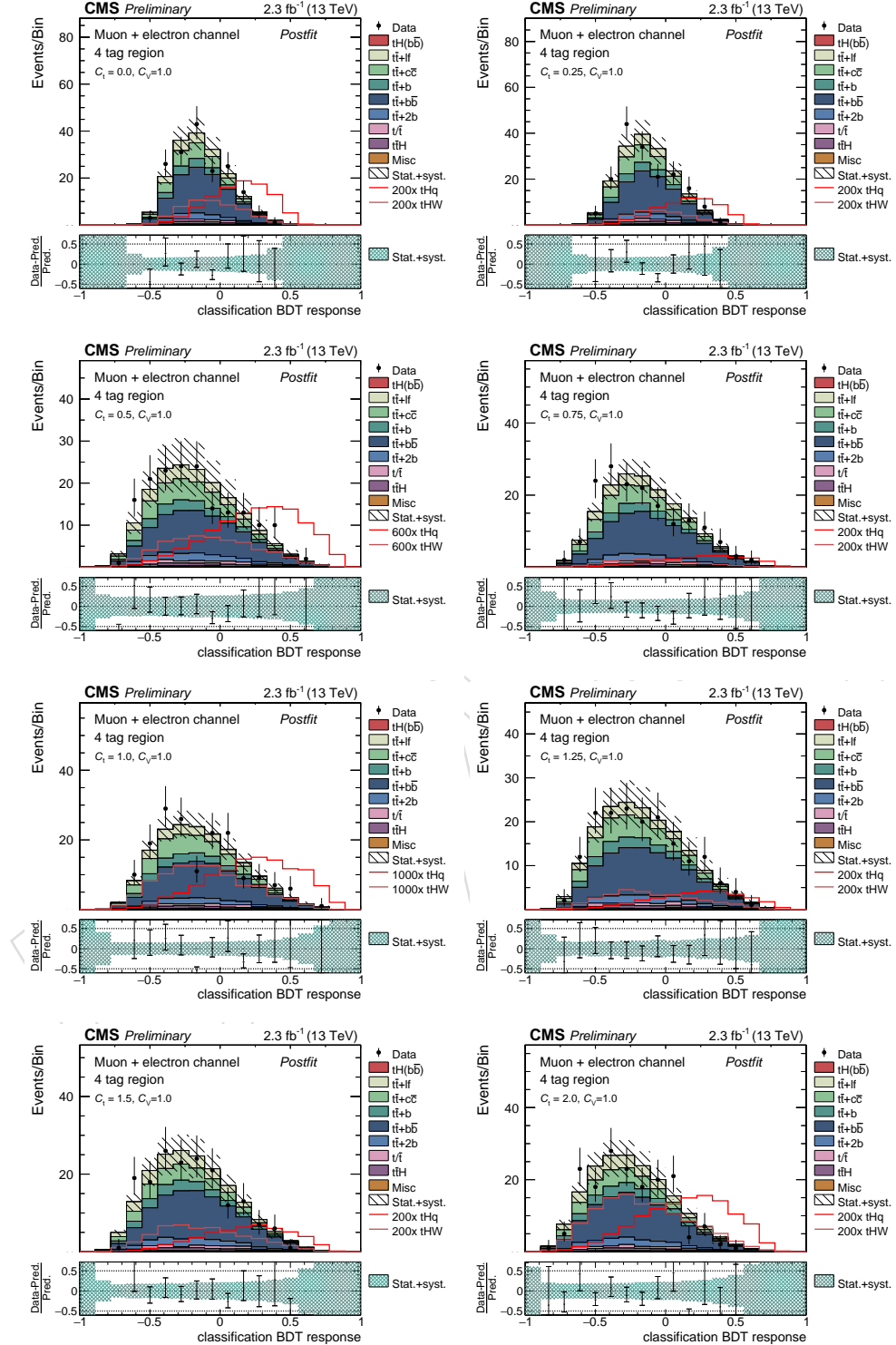


Figure 72: The output of classification BDT at 13 TeV in the 4 tag region for the different signal hypotheses is shown in this figure.

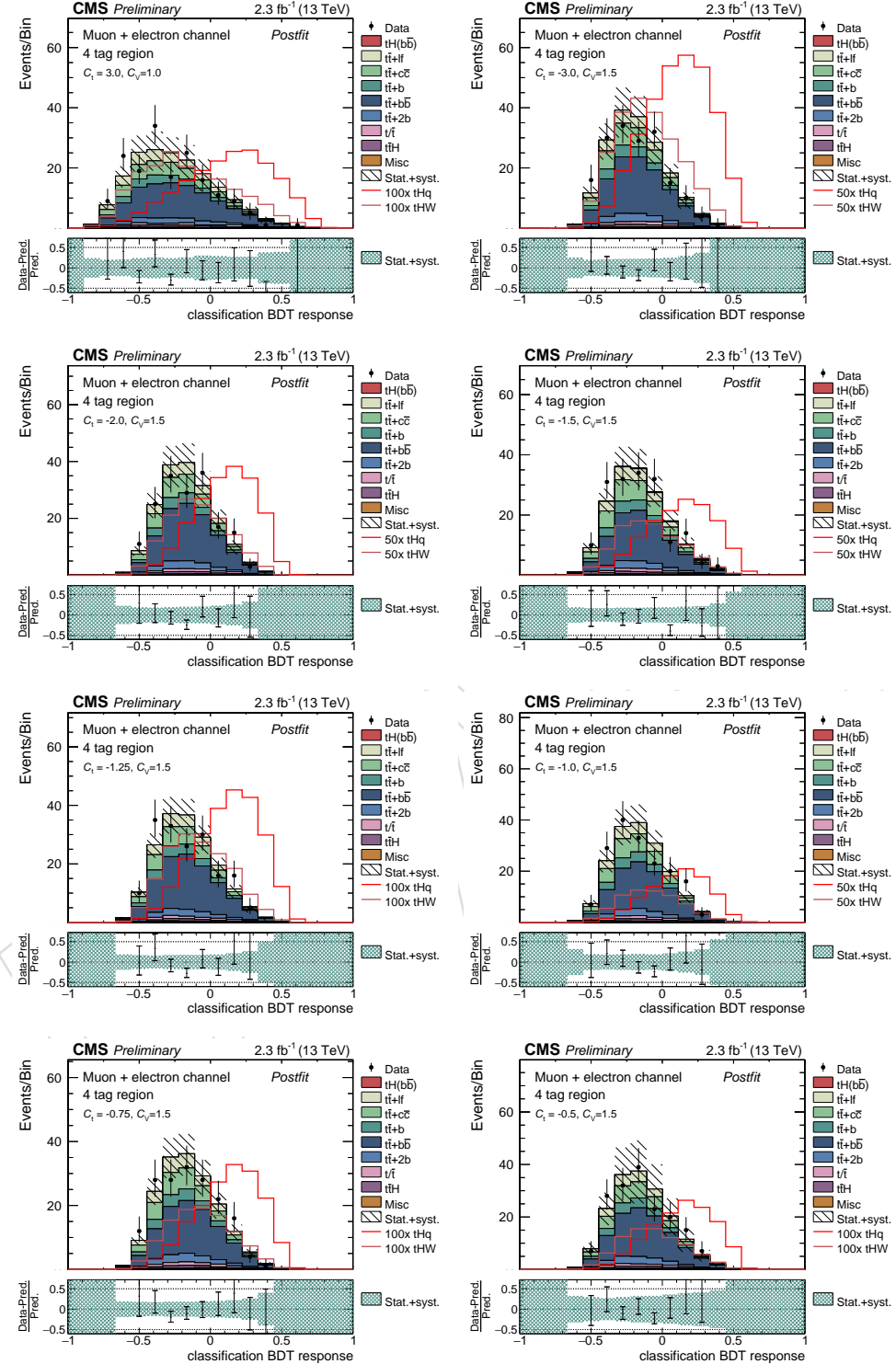


Figure 73: The output of classification BDT at 13 TeV in the 4 tag region for the different signal hypotheses is shown in this figure.

## E Appendix E: BDT output distributions

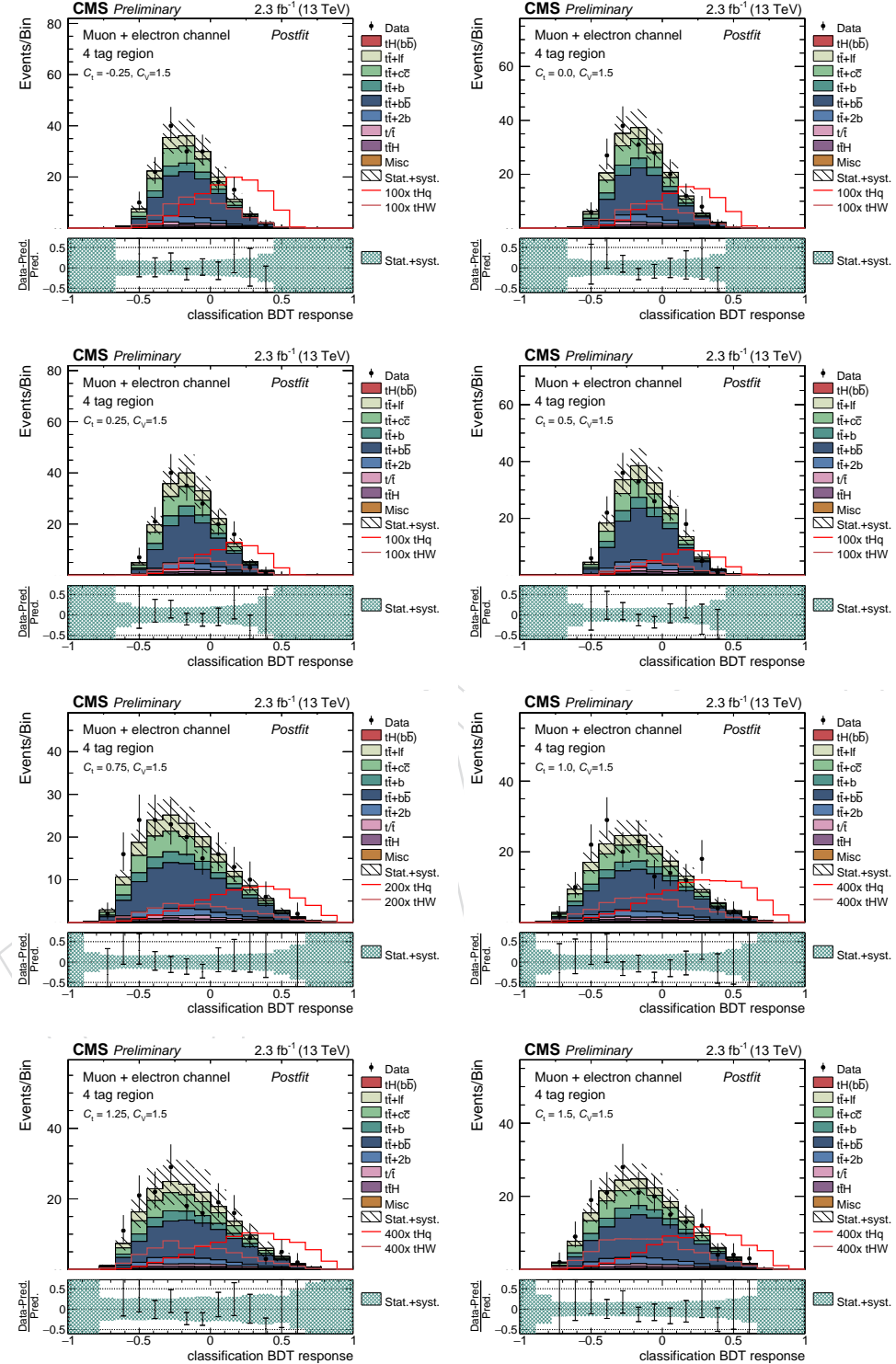


Figure 74: The output of classification BDT at 13 TeV in the 4 tag region for the different signal hypotheses is shown in this figure.

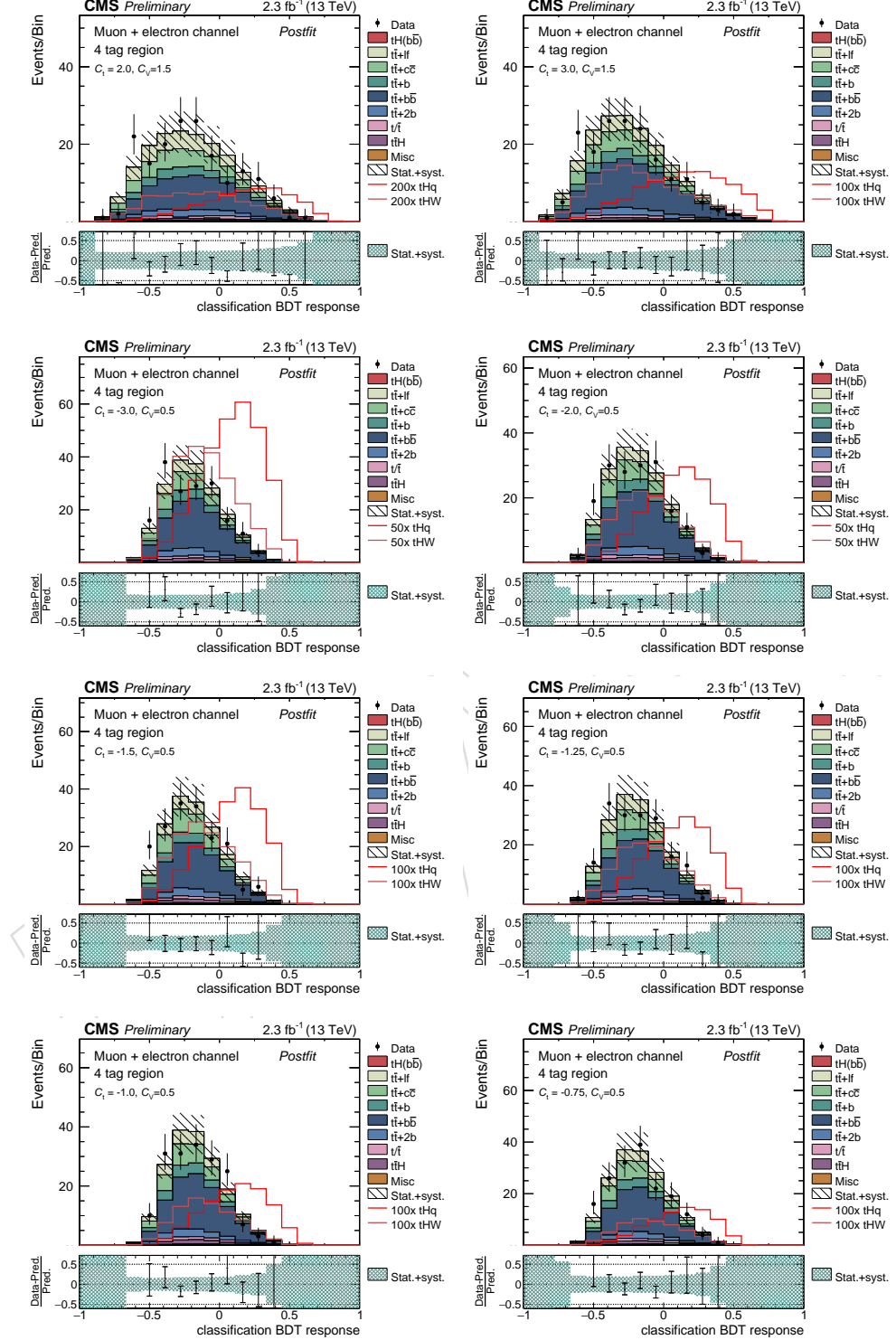


Figure 75: The output of classification BDT at 13 TeV in the 4 tag region for the different signal hypotheses is shown in this figure.

## E Appendix E: BDT output distributions

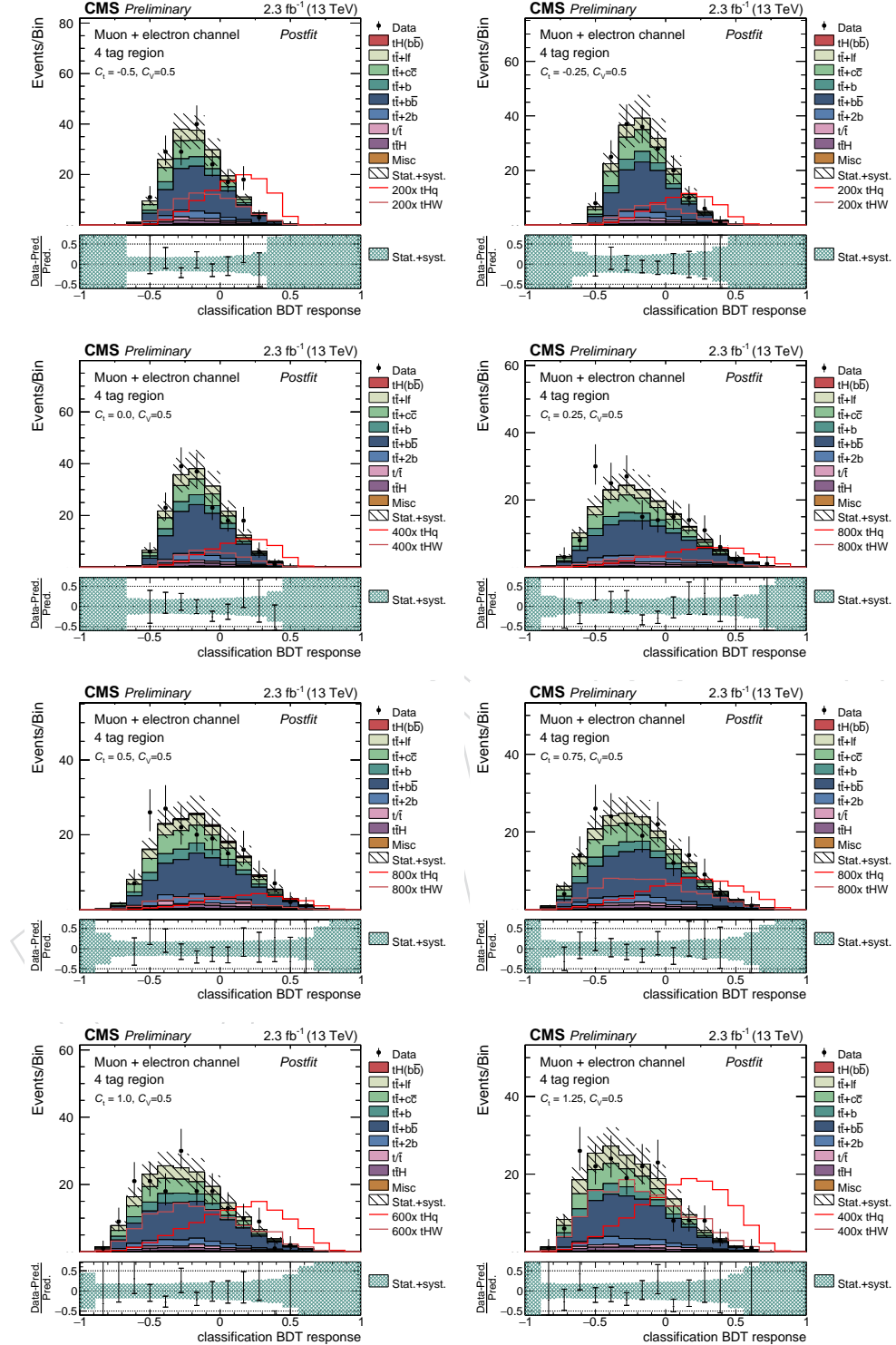


Figure 76: The output of classification BDT at 13 TeV in the 4 tag region for the different signal hypotheses is shown in this figure.

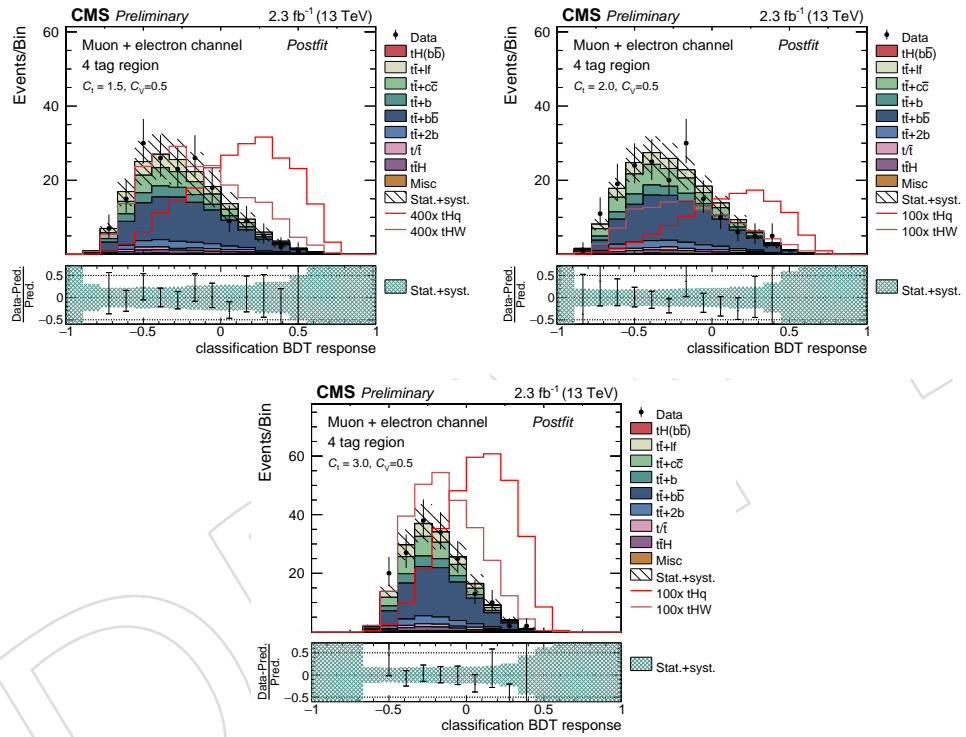


Figure 77: The output of classification BDT at 13 TeV in the 4 tag region for the different signal hypotheses is shown in this figure.

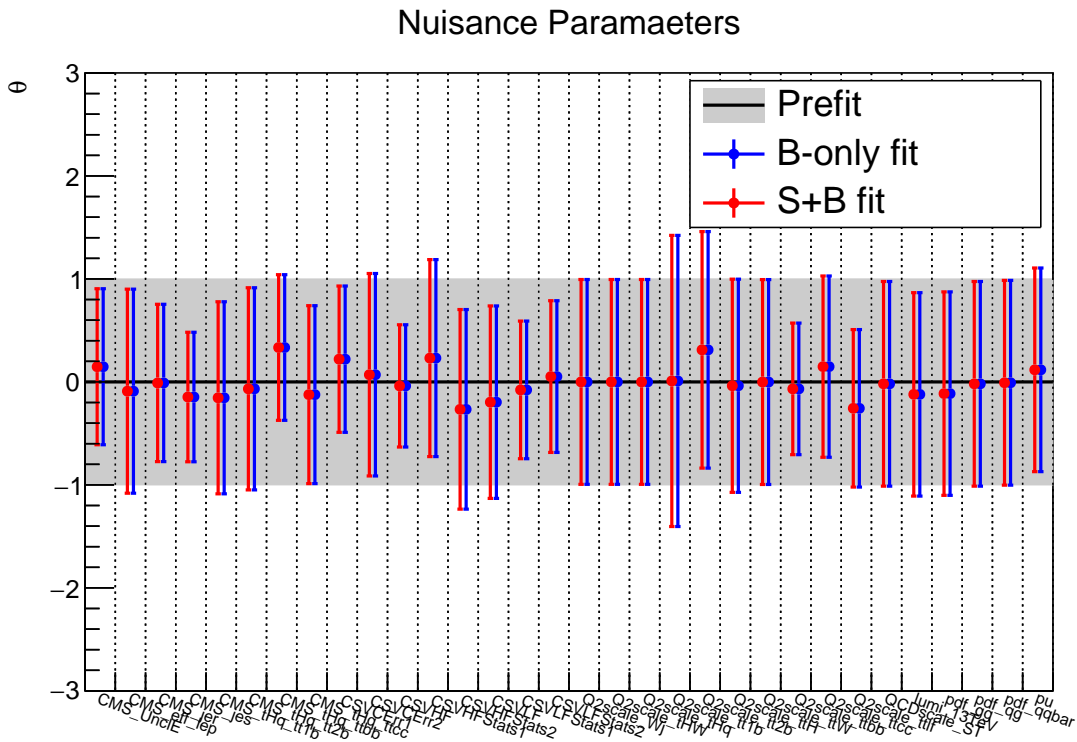


Figure 78: The pulls for data with no signal expected in the fit are shown in this figure.

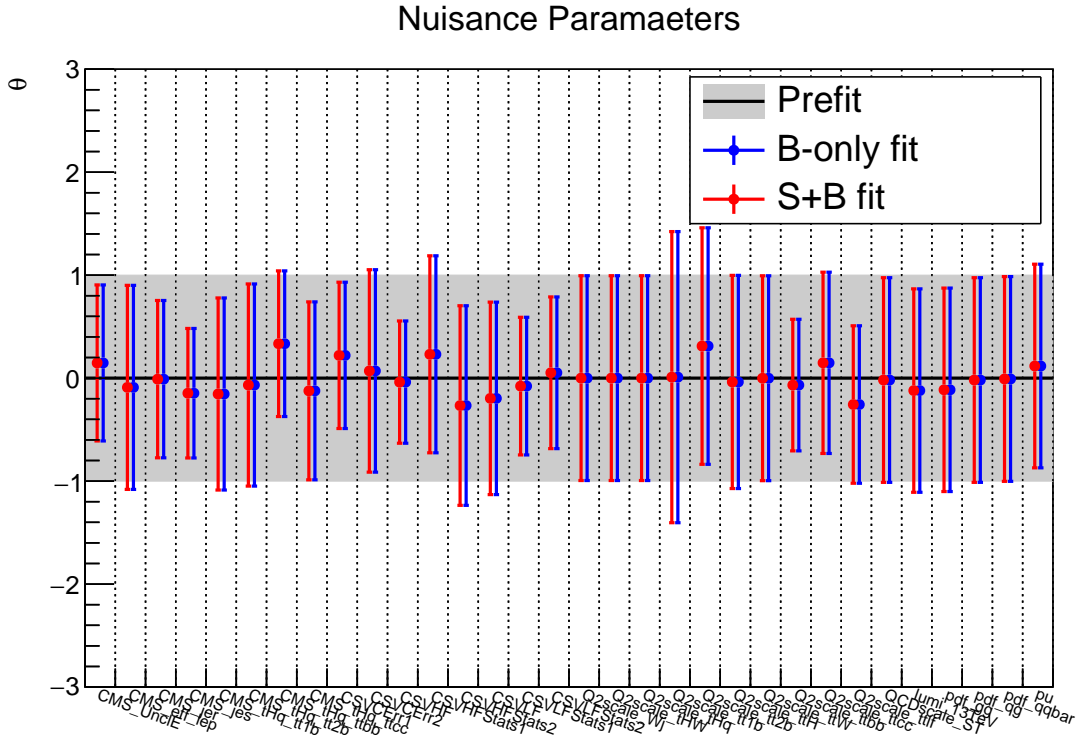


Figure 79: The pulls for data with signal expected in the fit are shown in this figure.

## 583 References

- [1] S. Dawson, "The effective W approximation", *Nucl. Phys.* **B249** (1985), no. 1, 42–60,  
doi:[http://dx.doi.org/10.1016/0550-3213\(85\)90038-0](http://dx.doi.org/10.1016/0550-3213(85)90038-0).
- [2] M. Farina et al., "Lifting degeneracies in Higgs couplings using single top production in association with a Higgs boson", *JHEP* **1305** (2013) 022,  
doi:[10.1007/JHEP05\(2013\)022](https://doi.org/10.1007/JHEP05(2013)022), arXiv:[1211.3736](https://arxiv.org/abs/1211.3736).
- [3] J. Chang, K. Cheung, J. S. Lee, and C.-T. Lu, "Probing the Top-Yukawa Coupling in Associated Higgs production with a Single Top Quark", arXiv:[1403.2053](https://arxiv.org/abs/1403.2053).
- [4] T. Tait and C.-P. Yuan, "Associated production of Higgs and single top at hadron colliders", *Phys. Rev. D* **63**, **014018** (2000).
- [5] F. Maltoni, K. Paul, and S. Willenbrock, "Associated production of Higgs and single top at hadron colliders", *Phys. Rev. D* **64**, **094023** (2001).
- [6] S. Biswas, E. Gabrielli, F. Margaroli, and B. Mele, "Direct constraints on the top-Higgs coupling from the 8 TeV LHC data", *JHEP* **07** (2013) 73,  
doi:[10.1007/JHEP07\(2013\)073](https://doi.org/10.1007/JHEP07(2013)073).
- [7] CMS Collaboration, "Search for H to  $b\bar{b}$  in association with single top quarks as a test of Higgs couplings", CMS-PAS-HIG-14-015 (2014).
- [8] F. Demartin et al., "tWH associated production at the LHC", arXiv:[1607.05862](https://arxiv.org/abs/1607.05862).
- [9] F. Demartin, F. Maltoni, K. Mawatari, and M. Zaro, "Higgs production in association with a single top quark at the LHC", *Eur. Phys. J.* **C75** (2015), no. 6, 267,  
doi:[10.1140/epjc/s10052-015-3475-9](https://doi.org/10.1140/epjc/s10052-015-3475-9).
- [10] NNPDF Collaboration, "Parton distributions for the LHC Run II", *JHEP* **04** (2015) 040,  
doi:[10.1007/JHEP04\(2015\)040](https://doi.org/10.1007/JHEP04(2015)040), arXiv:[1410.8849](https://arxiv.org/abs/1410.8849).
- [11] CMS Collaboration, "Search for  $t\bar{t}H$  production in the  $H \rightarrow b\bar{b}$  decay channel with  $\sqrt{s} = 13$  TeV pp collisions at the CMS experiment", CMS-PAS-HIG-16-004.
- [12] CMS Collaboration, "TTbar Hbb Run2 76X Samples and References".  
[https://twiki.cern.ch/twiki/bin/viewauth/CMS/TTbarHbbRun2ReferenceAnalysis\\_76XTransition](https://twiki.cern.ch/twiki/bin/viewauth/CMS/TTbarHbbRun2ReferenceAnalysis_76XTransition), last accessed on 14.07.2016.
- [13] CMS Collaboration, "Summary table of samples produced for the 1 Billion campaign, with 25ns bunch-crossing".  
<https://twiki.cern.ch/twiki/bin/viewauth/CMS/SummaryTable1G25ns>, last accessed on 27.05.2016.
- [14] CMS Collaboration, "NLO single-top channel cross sections".  
<https://twiki.cern.ch/twiki/bin/view/LHCPhysics/SingleTopRefXsec>.
- [15] F. Maltoni, D. Pagani, and I. Tsinikos, "Associated production of a top-quark pair with vector bosons at NLO in QCD: impact on  $t\bar{t}H$  searches at the LHC", *Journal of High Energy Physics* **02** (2016) 113, doi:[10.1007/JHEP02\(2016\)113](https://doi.org/10.1007/JHEP02(2016)113), arXiv:[1507.05640](https://arxiv.org/abs/1507.05640).
- [16] CMS Collaboration, "NNLO+NNLL top-quark-pair cross sections".  
<https://twiki.cern.ch/twiki/bin/view/LHCPhysics/TtbarNNLO>.

- [622] [17] LHC Higgs Cross Section Working Group, "Higgs cross sections and decay branching  
[623] ratios". <https://twiki.cern.ch/twiki/bin/view/LHCPhysics/LHCHXSWG>, last  
[624] accessed on 26.05.2016.
- [625] [18] CMS Collaboration, "CMS Luminosity Measurement for the 2015 Data Taking Period",  
[626] (2016). CMS-PAS-LUM-15-001.
- [627] [19] CMS Collaboration, "Offline Primary Vertex Reconstruction with Deterministic  
[628] Annealing Clustering", CMS Internal Note 2011-014, 2010.
- [629] [20] CMS Collaboration, "Baseline muon selections for Run-II - Tight Muon". [https://twiki.cern.ch/twiki/bin/view/CMS/SWGuideMuonIdRun2#Tight\\_Muon](https://twiki.cern.ch/twiki/bin/view/CMS/SWGuideMuonIdRun2#Tight_Muon),  
[630] last accessed on 27.04.2016.
- [632] [21] <https://twiki.cern.ch/twiki/bin/view/CMS/MultivariateElectronIdentification>.
- [633] [22] M. Cacciari, G. P. Salam, and G. Soyez, "The anti- $k_t$  jet clustering algorithm", *JHEP* **04**  
[634] (2008) 063, doi:10.1088/1126-6708/2008/04/063, arXiv:0802.1189.
- [635] [23] <https://twiki.cern.ch/twiki/bin/viewauth/CMS/JetID>.
- [636] [24] CMS Collaboration, "Recommended Jet Energy Corrections and Uncertainties For Data  
[637] and MC". <https://twiki.cern.ch/twiki/bin/view/CMS/JECDataMC>, last  
[638] accessed on 27.04.2016.
- [639] [25] CMS Collaboration, "Jet Energy Resolution". [https://twiki.cern.ch/twiki/bin/viewauth/CMS/JetResolution#JER\\_Scaling\\_factors\\_and\\_Uncertai](https://twiki.cern.ch/twiki/bin/viewauth/CMS/JetResolution#JER_Scaling_factors_and_Uncertai), last  
[640] accessed on 27.04.2016.
- [642] [26] CMS Collaboration, "Usage of b Tag Objects for 13 TeV Data with 25ns bunch spacing  
[643] and 76X ReReco".  
<https://twiki.cern.ch/twiki/bin/view/CMS/BtagRecommendation76X>.
- [645] [27] T. Chwalek, "Measurement of the W-Boson Helicity-Fractions in Top-Quark Decays with  
[646] the CDF II Experiment and Prospects for an Early  $t\bar{t}$  Cross-Section Measurement with the  
[647] CMS Experiment", Karlsruhe Institute of Technology, CERN-THESIS-2010-255, 2010.
- [648] [28] <https://twiki.cern.ch/twiki/bin/viewauth/CMS/PileupMCReweightingUtilities>.
- [649] [29] MuonPOG, "Reference muon id, isolation and trigger efficiencies for Run-II", 2016.  
<https://twiki.cern.ch/twiki/bin/view/CMS/MuonReferenceEffsRun2>, last  
[651] accessed on 27.04.2016.
- [652] [30] MuonPOG, "Muon T&P Instructions for Run-II", 2016.  
<https://twiki.cern.ch/twiki/bin/view/CMS/MuonTagAndProbeTreesRun2>,  
[653] last accessed on 27.04.2016.
- [655] [31] EgammaPOG, "Instructions for applying electron and photon ID", 2016.  
<https://twiki.cern.ch/twiki/bin/view/CMS/EgammaIDRecipesRun2>, last  
[657] accessed on 27.04.2016.
- [658] [32] EgammaPOG, "Instructions for applying electron and photon ID", 2016.  
<https://twiki.cern.ch/twiki/bin/view/CMS/ElectronScaleFactorsRun2>,  
[659] last accessed on 27.04.2016.

- 661 [33] BtagPOG, "Event reweighting using scale factors calculated with a tag and probe  
662 method", 2016. [https://twiki.cern.ch/twiki/bin/view/CMS/  
663 BTagShapeCalibration#Using\\_histogram\\_files](https://twiki.cern.ch/twiki/bin/view/CMS/BTagShapeCalibration#Using_histogram_files), last accessed on 17.05.2016.
- 664 [34] CMS Collaboration, "Calibration of the Combined Secondary Vertex b-Tagging  
665 discriminant using dileptonic  $t\bar{t}$  and Drell-Yan events", CMS Analysis Note AN-13-130,  
666 2013.
- 667 [35] <https://twiki.cern.ch/twiki/bin/viewauth/CMS/PileupSystematicErrors>.
- 668 [36] CMS Collaboration, "SM Higgs production cross sections at  $\sqrt{s} = 13$  TeV (update in  
669 CERN Report4 2016)". [https://twiki.cern.ch/twiki/bin/view/LHCPhysics/  
670 CERNYellowReportPageAt13TeV](https://twiki.cern.ch/twiki/bin/view/LHCPhysics/CERNYellowReportPageAt13TeV), last accessed on 05.05.2016.
- 671 [37] CMS Collaboration, "Standard Model Cross Sections for CMS at 13 TeV".  
672 [https://twiki.cern.ch/twiki/bin/view/CMS/  
673 StandardModelCrossSectionsat13TeVInclusive](https://twiki.cern.ch/twiki/bin/view/CMS/StandardModelCrossSectionsat13TeVInclusive).
- 674 [38] R. J. Barlow and C. Beeston, "Fitting using finite Monte Carlo samples", *Computer Physics  
675 Communication* **77** (1993) 219–228.
- 676 [39] J. S. Conway, "Incorporating Nuisance Parameters in Likelihoods for Multisource  
677 Spectra", in *Proceedings, PHYSTAT 2011 Workshop on Statistical Issues Related to Discovery  
678 Claims in Search Experiments and Unfolding, CERN, Geneva, Switzerland 17-20 January 2011*.  
679 2011. arXiv:1103.0354.
- 680 [40] CMS Collaboration, "Modelling of the single top-quark production in association with  
681 the Higgs boson at 13 TeV". [https://twiki.cern.ch/twiki/bin/viewauth/  
682 CMS/SingleTopHiggsGeneration13TeV](https://twiki.cern.ch/twiki/bin/viewauth/CMS/SingleTopHiggsGeneration13TeV).